Stress and strain
of a plate boundary

- the Reykjanes Peninsula, SW Iceland

Marie Keiding

Stress and strain of a plate boundary
- the Reykjanes Peninsula, SW Iceland

Marie Keiding

A dissertation submitted to the Faculty of Earth Sciences for the degree of
Doctor of Philosophy in Geophysics

Thesis advisors

Dr. Þóra Árnadóttir
Nordic Volcanological Centre, University of Iceland

Dr. Björn Lund
Department of Earth Sciences, Uppsala University

Doctoral Committee

Dr. Þóra Árnadóttir
Nordic Volcanological Centre, University of Iceland

Dr. Björn Lund
Department of Earth Sciences, Uppsala University

Prof. Páll Einarsson
Institute of Earth Science, University of Iceland

Opponents

Prof. Kristine M. Larson
Dept. Aerospace Engineering Sciences, University of Colorado

Prof. Ólafur Guðmundsson
School of Science and Engineering, Reykjavík University

Faculty of Earth Sciences
School of Engineering and Natural Sciences
University of Iceland

Stress and strain of a plate boundary - the Reykjanes Peninsula, SW Iceland
A dissertation submitted to the Faculty of Earth Sciences for the degree of
Doctor of Philosophy in Geophysics

Contents

Abstract

The Reykjanes Peninsula in southwest Iceland offers excellent opportunities to study the dynamics of an obliquely divergent plate boundary zone. Both left-lateral shear and extension are accommodated on the peninsula, resulting in a plate boundary zone characterised by high earthquake activity as well as recent volcanism. This thesis investigates crustal deformation and earthquakes along the plate boundary on the Reykjanes Peninsula, using a variety of geophysical methods.

In the first paper, we use GPS velocities from 2000–2006 to derive a kinematic elastic half-space model of the plate boundary deformation on the Reykjanes Peninsula. The model predicts left-lateral motion of 18^{+4}_{-3} mm/yr and opening of 7^{+3}_{-2} mm/yr below a locking depth of 7^{+1}_{-2} km (95% confidence levels). The resulting deep motion, of 20^{+4}_{-3} mm/yr in the direction of N(100^{+8}_{-6})°E, agrees well with the predicted relative North America - Eurasia rate, showing that the observed surface deformation is consistent with the plate motion models. The GPS strain rate fields, however, reveal temporal and spatial variations within the plate boundary zone due to shallow sources related to earthquakes or geothermal activity.

The second paper presents the first comprehensive analysis of the seismicity on the Reykjanes Peninsula, since early instrumental earthquake recordings in 1926. The seismicity on the peninsula shows a systematic change from primarily earthquake swarms in the west to mainshock-aftershock sequences in the east, reflecting the transition from seafloor spreading along the Reykjanes Ridge to transform motion in the South Iceland Seismic Zone. The state of stress during 1997–2006, as estimated from inversion of micro-earthquake focal mechanisms, is mainly strike-slip with a tendency toward a normal stress state. We find

an excellent agreement between the directions of least compressive stress from inversion of earthquake data and the directions of greatest extensional strain rate derived from GPS data, indicating that the earthquakes are primarily driven by plate motion.

Finally, the third paper presents a geodetic study of the crustal deformation on the Reykjanes Peninsula, using Interferometric Synthetic Aperture Radar (In-SAR) data from 1992–1999 and 2003–2008, as well as GPS data from 2000–2009. The geodetic data reveal deformation due to the plate spreading, anthropogenic subsidence due to geothermal fluid extraction in the Reykjanes, Svartsengi and Hellisheidi fields and, possibly, increasing pressure in the Krísuvík geothermal system. The installation of the Reykjanes geothermal power plant in 2006 results in subsidence of around 10 cm during the first two years of production. Short-lived swarms of micro-earthquakes as well as aseismic fault movement appear to be triggered by the stresses due to geothermal fluid extraction.

Ágrip

Ritgerðin fjallar um jarðskorpuhreyfingar og jarðskjálfta á Reykjanesskaga. Fleka-
skil Norður-Ameríku og Evrasíu flekanna liggja eftir skaganum endilöngum, frá
Reykjaneshrygg í vestri að Suðurlandsbrotabeltinu í austri. Rekstefnan er ekki
hornrétt á flekaskilin á Reykjanesskaga, og það veldur bæði vinstri-handar skúf-
hreyfingu og gliðnun yfir skagann. Mikil jarðskjálftavirkni og eldvirkni á nútíma
eru á flekaskilunum, og svæðið því tilvalið til rannsókna á ferlum sem einkenna
virk skásett (*e. oblique*) rekbelti.

Ritgerðin er samsett úr þremur vísindagreinum ásamt inngangi. Í fyrstu grein-
inni er greint frá niðurstöðum Global Positioning System (GPS) landmælinga á
Reykjanesskaga á tímabilinu 2000 til 2006. Með endurteknum GPS mælingum
má reikna færslu og færsluhraða stöðva í landmælinganetinu og þannig fæst þrívíð
mynd af jarðskorpuhreyfingum á skaganum. Þrívíða hraðakortið er síðan notað
til að gera líkan af flekaskilunum. Til einföldunar gerir líkanið ráð fyrir að jörðin
sé fjaðrandi hálfrúm og að hreyfingunni á flekaskilunum megi lýsa sem skriði á
lóðréttum flötum. Andhverfureikningar (*e. inversion*) eru notaðir til að meta
hraða vinstri-handar skúfhreyfingar og gliðnunar ásamt þykkt brotgjörnu jarð-
skorpunnar á þessu svæði. Í því líkani sem fellur best að mæligögnunum er árleg
vinstri-handar skúfhreyfing sem nemur 18^{+4}_{-3} millimetrum (mm), gliðnun sem er
um 7^{+3}_{-2} mm, og þykkt brotgjörnu skorpunnar er 7^{+1}_{-2} km (óvissa er metin sem 95%
vikmörk). Líkanið bendir til þess að færsla í neðri skorpu/efri möttli undir fleka-
skilunum á Reykjanesskaga sé um 20^{+4}_{-3} mm á ári í stefnu N(100^{+8}_{-6})°Austur, sem
er í samræmi við viðtekin líkön af hreyfingu Evrasíu flekans miðað við Norður-
Ameríku á stærri lengdarkvarða. Breytingar á hraða aflögunar (*e. strain rate*)
sem greina má milli ára tengjast grunnstæðum ferlum í brotgjörnu skorpunni,
s.s. jarðskjálftum og jarðhitavirkni.

Önnur greinin í ritgerðinni fjallar um jarðskjálfta á Reykjanesskaga. Í fyrri hluta greinarinnar er yfirlit yfir jarðskjálftavirkni á Reykjanesskaga frá árinu 1926 til 2006. Jarðskjálftavirknin er fyrst og fremst smáskjálftavirkni í skjálftahrinum á vesturhluta skagans en stærri skjálftar og eftirskjálftavirkni einkenna eystri hluta hans. Þetta endurspeglar breytingar á eðli flekaskilanna frá vestri til austurs, þ.e. frá fráreksbelti á Reykjaneshrygg til skjálftabeltisins á Suðurlandi, þar sem hjárek er ríkjandi. Í seinni hluta greinarinnar er spennuástand bergs reiknað út frá staðsetningum og brotlausnum smáskjálfta á tímabilinu 1997–2006, sem einkum sýna sniðgengishreyfingar en einnig nokkra hreyfingu á siggengjum. Mesta nýmælið í þessari rannsókn felst í mati á spennuástandi bergs og samanburði á stefnuásum spennu sem losnar í jarðskjálftum og stefnuásum aflögunar. Rannsóknirnar sýna að gott samræmi er milli stefnu ása minnstu þrýstispennu, sem metin er út frá brotlausnum jarðskjálfta, og stefnu mestu gliðnunar (*e. extensional strain*), sem fæst með túlkun á GPS mælingum. Þessar niðurstöður benda til að sú spenna sem losnar í jarðskjálftum á Reykjanesskaga sé fyrst og fremst til komin vegna flekareks.

Í þriðju greininni í ritgerðinni er greint frá niðurstöðum radarmælinga með gervitunglum, sem sýna jarðskorpuhreyfingar á Reykjanesskaga á tímabilunum 1992 til 1999 og 2003 til 2008. Einnig er fjallað um niðurstöður GPS mælinga á tímabilinu frá 2000 til 2009. Landmælingarnar sýna jarðskorpuhreyfingar vegna flekareks og sig vegna vinnslu á jarðhitasvæðunum á Reykjanesi í Svartsengi og Hellisheiði. Landmælingarnar sýna einnig landris á jarðhitasvæðinu við Krísuvík, sem bendir til aukins þrýstings í jarðhitageyminum þar. Fyrstu tvö árin eftir að virkjunin á Reykjanesi var tekin í notkun í maí 2006 mældist sig, sem nemur mest um 10 cm, vegna uppdælingar jarðhitavökva á svæðinu. Einnig er líklegt að hrinur smáskjálfta og hæg færsla á misgengjum án mældrar skjálftavirkni tengist spennubreytingum í bergi vegna jarðhitavinnslu á Reykjanesi.

Acknowledgements

x

Chapter 1

Introduction

The main objective of this PhD project is to improve our understanding of the dynamics of an oblique, divergent plate boundary: the Reykjanes Peninsula in southwest Iceland. Some of the questions that are addressed in this work are whether the deformation within the plate boundary zone is consistent with the plate motion predicted by the plate models, and how the regional distributed strain at the surface relates to the discrete, brittle deformation at depth. Several different geophysical techniques have been applied, namely GPS, InSAR, surface deformation modelling, earthquake analysis, and stress tensor inversion of earthquake focal mechanisms.

This thesis consists of two parts. The first part is an introduction to the study area and the methods used in the project. The second and main part is a compilation of three papers that address different aspects of the plate boundary deformation on the Reykjanes Peninsula. The included papers are:

I **Keiding, M.**, T. Árnadóttir, E. Sturkell, H. Geirsson, and B. Lund, 2008. Strain accumulation along an oblique plate boundary: the Reykjanes Peninsula, southwest Iceland. *Geophys. J. Int.*, **172**, 861–872, doi:10.1111/j.1365-246X.2007.03655.x.

II **Keiding, M.**, B. Lund, and T. Árnadóttir, 2009. Earthquakes, stress and strain along an obliquely divergent plate boundary: the Reykjanes Peninsula, southwest Iceland, *J. Geophys. Res.*, **114**, doi:10.1029/2008JB006253.

III **Keiding, M.**, T. Árnadóttir, S. Jónsson, J. Decriem, and A. Hooper, 2009. Plate boundary deformation and man-made subsidence around geothermal fields on the Reykjanes Peninsula, Iceland, *to be submitted to J. Volcanol. Geoth. Res.*

1.1 The Reykjanes Peninsula

The Icelandic plate boundary is a complicated and changing system of volcanic rifts and fault zones, due to the interplay between the Mid-Atlantic spreading ridge and the Icelandic mantle plume (Figure 1.1). Throughout the geological history of Iceland the westward motion of the spreading ridge, with respect to the mantle plume, has resulted in a number of eastward rift jumps and an increasing offset of the plate boundary in Iceland from the Mid-Atlantic spreading ridge (Einarsson, 1991). As a result, most of the plate boundary in Iceland is oriented at an oblique angle to the spreading direction. On the Reykjanes Peninsula, the plate boundary trends approximately N80°E, highly oblique to the NUVEL-1A spreading direction of N103°E at 63.9°N, 22.0°W (DeMets et al., 1994).
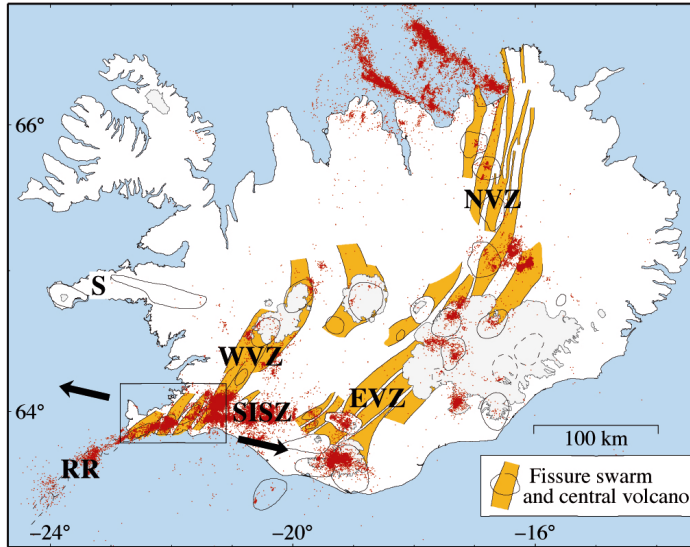
Figure 1.1: Neovolcanic and seismic zones of Iceland. Orange colours indicate the volcanic systems (Einarsson and Sæmundsson, 1987), and red dots are 1997–2008 earthquake locations from the SIL seismic catalogue. RR: Reykjanes Ridge, SISZ: South Iceland Seismic Zone, S: Snæfellsnes Peninsula, WVZ: Western Volcanic Zone, EVZ: Eastern Volcanic Zone, NVZ: Northern Volcanic Zone. The box shows the location of the Reykjanes Peninsula (Figure 1.2), and the arrows show the direction of the 2 cm/yr spreading across the Reykjanes Peninsula between North America and Eurasia (DeMets et al., 1994).

Rifting on the Reykjanes Peninsula began after a rift jump 6–7 Ma ago (Sæ-mundsson, 1978). Today, the plate boundary is expressed as a zone of high seismicity and recent volcanism, forming the transition from the offshore Reyk-janes Ridge in the west to the South Iceland Seismic Zone in the east (Einarsson, 1991). Earthquake surveys on the western part of the peninsula have revealed that the seismic zone is not a single fault but rather a series of strike-slip and normal faults (Klein et al., 1973, 1977). Analyses of the seismicity since early earthquake recordings in 1926 show that there is a systematic change in the seis-micity on the Reykjanes Peninsula, from primarily swarm activity in the west to mainshock-aftershock sequences in the east (Tryggvason, 1973; Einarsson, 1991; Keiding et al., 2009). The largest earthquakes on the peninsula reach magnitudes above 6 on the eastern part of the peninsula. A pioneering geodetic study us-ing electronic distance measurements from 1968–1972 indicated a combination of left-lateral motion and extension (Brander et al., 1976). Recent modelling of GPS data from 2000–2006 has confirmed that the observed deformation is consistent with the predicted oblique plate motion on a regional scale (Árnadóttir et al., 2006; Keiding et al., 2008).

The peninsula is almost entirely covered with postglacial lavas with lesser in-terglacial lavas and hyaloclastites (Sæmundsson and Einarsson, 1980). Eruptive activity on the Reykjanes Peninsula appears to repeat itself in a thousand-year cycle, consisting of an eruptive period lasting a few hundred years and a non-eruptive period lasting several hundred years (Sigurgeirsson, 1995). The most recent eruption occurred in the 13th century (Thordarson and Larsen, 2007). The volcanic eruptions on the peninsula have occurred from a series of NE-trending eruptive fissures, which are grouped into four en-echelon volcanic fissure swarms (Sæmundsson, 1978). The fissure swarms comprise many normal faults and ex-tensional tension fractures in addition to the eruptive fissures (Figure 1.2). A change in the structural style is apparent from the distribution of eruptive fis-sures. On the western part of the peninsula the fissures are relatively short and widely distributed, while they become longer and focussed into narrow zones as we move eastward along the peninsula (Amy Clifton, personal communication, 2008).

The fissure swarms are intersected at an oblique angle by a series of km-scale near-vertical N–S right-lateral strike-slip faults, located in an E–W trending zone
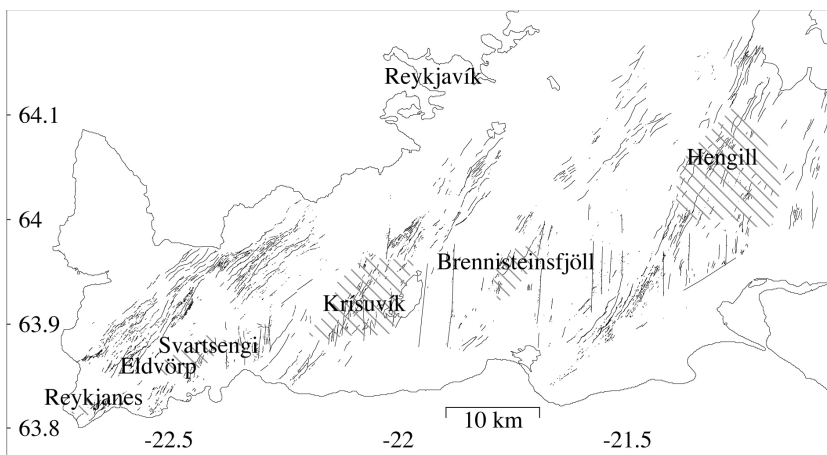
Figure 1.2: Tectonic map of the Reykjanes Peninsula, with fracture locations from Clifton and Kattenhorn (2006). The hatched areas show the locations of high-temperature geothermal fields.

along the southern part of the peninsula (Clifton and Kattenhorn, 2006). Left-lateral shear along the plate boundary is accommodated by right-lateral slip on the N–S strike-slip faults, in a similar manner to the book-shelf faulting in the South Iceland Seismic Zone (e.g. Árnadóttir et al., 2004). Almost all the seismic energy is released by strike-slip earthquakes, and the larger earthquakes, of magnitude 5 or above, have all occurred on the prominent N–S strike-slip faults. Micro-earthquakes with normal and even reverse mechanisms are, however, frequently observed (Keiding et al., 2009).

A number of high-temperature geothermal fields are present on the Reykjanes Peninsula (see Figure 1.2), located primarily at the intersection of the eruptive fissures and the strike-slip faults (Amy Clifton, personal communication, 2009). From west to east the geothermal fields are the Reykjanes, Eldvörp, Svartsengi, Krísuvík and Brennisteinsfjöll fields. The Reykjanes Peninsula is bounded to the east by the Hengill fissure swarm which comprises one of the largest geothermal fields in Iceland. Energy has been harnessed from the Svartsengi field since 1976, and from the Hengill field since 1990. New power plants were installed on Hellisheidi in the southern Hengill field and in the Reykjanes geothermal field

during 2006. The extraction of geothermal fluids causes local deformation that is often so large that it obscures the deformation due to tectonic processes such as plate boundary deformation. The host rock deformation associated with geothermal fluid extraction can provide important insight in the extent, morphology and dynamics of the subsurface fluid reservoirs.

1.2 Methods

1.2.1 GPS

The Global Navigation Satellite System (GNSS) is a space-based positioning system that provides accurate position and time information to users on ground, sea, air or space. At present, the GNSS includes the American NAVSTAR Global Positioning System (GPS) and the Russian GLONASS. The GPS constellation consists of at least 24 satellites located in six 12-hour orbits at an altitude of 20,200 km above the surface of the Earth, inclined 55° with respect to equator (Figure 1.3). The constellation is optimised to give the best coverage between ±75° latitude.
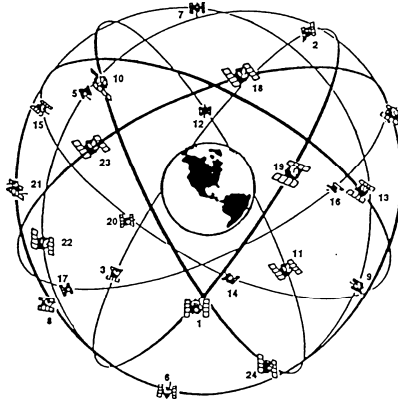
Figure 1.3: GPS satellite constellation, viewed from latitude of approximately 30°.

The satellite orbits are tracked by a network of monitoring and control facilities on ground. Precise orbits are computed from the tracking data by the International GNSS Service (IGS) and the Center for Orbit Determination (CODE) in Europe. Rapid orbits are available from both IGS and CODE within a few hours, while the final orbits are available after 1–2 weeks.

The GPS satellites have atomic clocks, solar panels and radio transmitters. They transmit digital time signals at two carrier frequencies, L1 ($\lambda_1 \approx 19$ cm) and L2 ($\lambda_2 \approx 24$ cm). The two carriers are modulated with a pseudo-random noise

code (P-code), which may be encrypted. In addition to the code, the carriers transmit a navigation message that contains information such as the readings of the satellite clocks and the orbital parameters.

The GPS receivers use the time signals broadcast by the satellites to compute the travel times of the signals and thereby estimate the range between each satellite and the receiver. For GPS positioning, at least four satellites must be in view of the receiver at the same time, to solve for the 3-D position and the receiver clock error. Treating the clock error as the fourth unknown, enables the receivers to be built with an inexpensive crystal clock rather than an expensive atomic clock.

The time measurement has to be very precise, because the signal travels at the speed of light. For example, an error of three nanoseconds in the time measurement is equivalent to an error of $\sim$1 m on the estimated distance. There are several sources of error on the GPS signal, of which the ionospheric delay is the most important. The ionosphere is the upper part of the atmosphere from approximately 80 km to 1000 km, where there is a high concentration of charged particles due to ionisation caused by solar and cosmic radiation. The ionospheric delay is frequency-dependent, hence the effect of the ionospheric delay can be accurately estimated from direct measurements of the delay on the L1 and L2 signals along the signal path. Another source of error is the tropospheric delay due to dry air and water vapour in the lower part of the atmosphere. The delay due to the dry air makes up the main part of the tropospheric delay and can be easily modelled, while the delay due to variations in water vapour is more unevenly distributed. Other important sources of error are the receiver clock error and satellite clock syncronisation, electronic noise on the signal, and multipath errors caused by signals bouncing of buildings and other reflecting surfaces.

The distance from the satellite to the receiver is computed as the travel time multiplied with the speed of light, and referred to as pseudoranges. There are two ways of estimating the pseudoranges: using either measurements of the code or of the carrier phase. Code pseudoranges are estimated using the absolute time difference by the modulated signal from the satellite and a reference signal that the receiver generates using a copy of the known code for this particular satellite. The code pseudorange measurement is used for real-time, low-accuracy positioning. Phase pseudoranges are estimated using the relative phase difference

between the satellite carrier, which is reconstructed by the receiver using a copy of the known code, and a reference signal generated by the receiver. The phase pseudoranges for the ith satellite and the kth receiver are given by

$$
\begin{aligned}
D^i_{1k} &= \rho^i_k + c\,\delta_k - c\,\delta^i - I^i_k + T^i_k + \lambda_1 n^i_{1k} + \epsilon_1 \\
D^i_{2k} &= \rho^i_k + c\,\delta_k - c\,\delta^i - \frac{f^2_1}{f^2_2} I^i_k + T^i_k + \lambda_2 n^i_{2k} + \epsilon_2
\end{aligned}
\tag{1.1}
$$

where ρ is the geometric distance due to the measured phase difference, c is the speed of light, δ is the clock error on receiver or satellite, f is the carrier frequency, I is the ionospheric delay for L1, T is the tropospheric delay, λ is the carrier wavelength and n is the integer number of cycles (Dach et al., 2007). The subscripts 1, 2 refer to the two carriers L1 and L2. The noise term ϵ is due to the uncertainty of the measured value of ρ and is usually 1–3 mm for phase pseudoranges. The advantage of the phase pseudorange measurement is that the phase difference can be measured with high precision. However, the integer number of cycles is unknown, which adds another unknown to the equation, the so-called 'initial phase ambiguity'. The initial phase ambiguity is constant as long as the receiver is locked onto the satellite signal, but every time there is a cycle slip, for example when the signal gets blocked by a building or mountain, then another initial phase ambiguity is added to the unknowns.

In this project, the GPS data were post-processed using the Bernese software (Dach et al., 2007), with precise CODE orbits. The Bernese software processes observations of phase pseudoranges to compute daily solutions for coordinates and covariances. During processing, some of the unknowns are eliminated by forming differences of the original observations. Single difference observations are formed between one satellite and two receivers, while double difference observations are formed between two satellites and two receivers (Figure 1.4). By forming double difference observations the receiver and satellite clock errors can be eliminated. The ionospheric delay is estimated by measurements of the frequency-dependent delays on the two carriers, and the tropospheric delay is estimated through modelling. The initial phase ambiguities usually make up most of the unknown parameters. These can be resolved as real-valued parameters when the clock errors and ionospheric and tropospheric delays have been eliminated from equation (1.1). The resolution of the ambiguities is aided by including a large

number of measurements in the processing, thus the solution is improved with the length of the observation session.
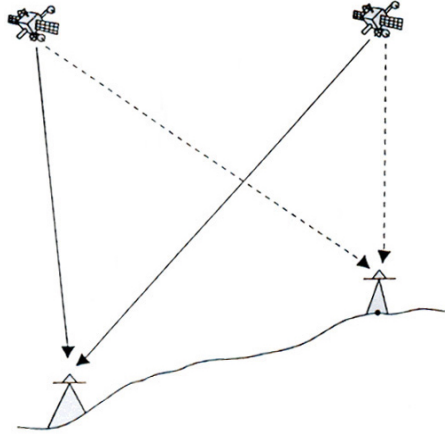
Figure 1.4: Double difference GPS measurement between two satellites and two receivers.

A number of international IGS stations are included in the processing to aid the stabilisation in a global reference frame (Dow et al., 2005). The daily solutions output by Bernese are then combined into campaign solutions and stabilised in the International Terrestrial Reference Frame (ITRF) 2005 (Altamimi et al., 2007), using the GLOBK software (Herring et al., 2006). Finally, time series are formed and velocities computed from the campaign solutions.

Measurements

Campaign GPS measurements for crustal deformation studies are done using permanent benchmarks mounted in solid bedrock. The antenna is installed exactly above the benchmark and the antenna height is measured (Figure 1.5). A receiver is then connected to the antenna and the instrument is left to measure for 2–3 days. Two successive measurements can be combined to give a displacement of an instantaneous event, given that the background velocity is known and can be subtracted. Repeated measurements over a number of years can be used to generate an estimate of the long-term velocity.

Figure 1.5: GPS campaign measurement. The antenna is installed exactly above the benchmark and the antenna height is measured. Photo: Erik Sturkell.

Figure 1.6 shows examples of time series at two GPS stations, with the north, east and vertical components in ITRF2005. The station RNES is located on the tip of the peninsula where the Reykjanes geothermal power plant was put into operation in 2006. Following the start of production a subsidence bowl has evolved around the power plant due to compaction of the rocks in the geothermal reservoir, affecting both the vertical and horizontal motion at RNES. The station HH04 shows horizontal offset of several cm due to two M_W 6.0–6.1 earthquakes that occurred in the western South Iceland Seismic Zone on 29 May 2008 (Hreinsdóttir et al., 2009). The uncertainties vary systematically for the east, north and vertical components due to the geometry of station network and satellite orbits. The vertical measurements have the largest uncertainties because all stations are basically at the same vertical position compared to the satellites 20,200 km above the Earth's surface. Larger uncertainties are recorded for the north component than for the east component in Iceland, because the satellite constellation tracks more east-west than north-south at the latitude of Iceland.

A network of continuous GPS stations in Iceland is operated by the Icelandic Meteorological Office (Geirsson et al., 2006). The continuous GPS stations are
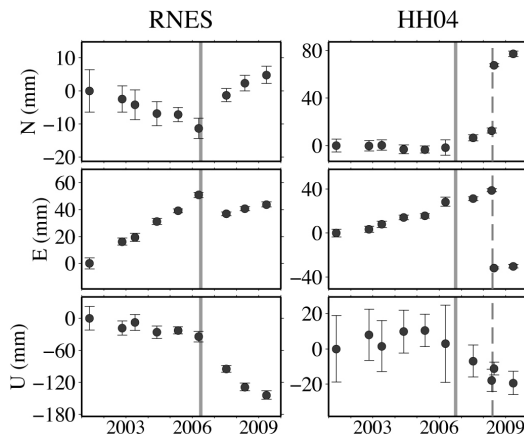
Figure 1.6: North, east and vertical time series at the campaign stations RNES and HH04 on the Reykjanes Peninsula, in the ITRF2005 reference frame (Altamimi et al., 2007). Error bars indicate 1σ uncertainties. The solid vertical lines show the approximate start of production at the Reykjanes and Hellisheidi geothermal power plants. The stippled line shows the time of an earthquake sequence on 29 May 2008.

installed at permanent monuments and transmit data in real-time to the central operating office by modem or radio connection. The data are processed daily using the predicted CODE orbits, and published immediately on the web. Subsequent processing using precise CODE orbits is performed for crustal deformation studies.

1.2.2 InSAR

Interferometric Synthetic Aperture Radar (InSAR) is a recent development in space-borne radar measurements of the Earth's surface (e.g. Bürgmann et al., 2000). Whereas ground-based observations, such as GPS, are usually sparse, the radar technique can provide very dense spatial sampling of the ground deformation. However, the SAR data only provide 1-dimensional observations in the look direction from satellite to ground.

The SAR satellites travel at approximately 800 km height and have a side-looking geometry, illuminating a 100 km wide swath of the ground. The satellites travel either approximately northward (ascending) or southward (descend-

ing) in various different orbits. The radar transmits electromagnetic pulses to the Earth's surface and detects the echoes, which are then focussed to form a raw image. Resolution is improved in the direction perpendicular to the flight direction (range) by pulse compression, while resolution in the flight direction (azimuth) is improved by analysis of Doppler frequency shifts of the echoes. The Doppler frequency analysis uses the fact that two points, at slightly different azimuth angles, have different speeds relative to the moving radar. Hence, two points that are in the beam at the same time can be distinguished by their different Doppler frequency shifts. The use of these techniques enables a SAR image resolution of approximately 5 m in the flight direction and 20 m perpendicular to the flight direction.
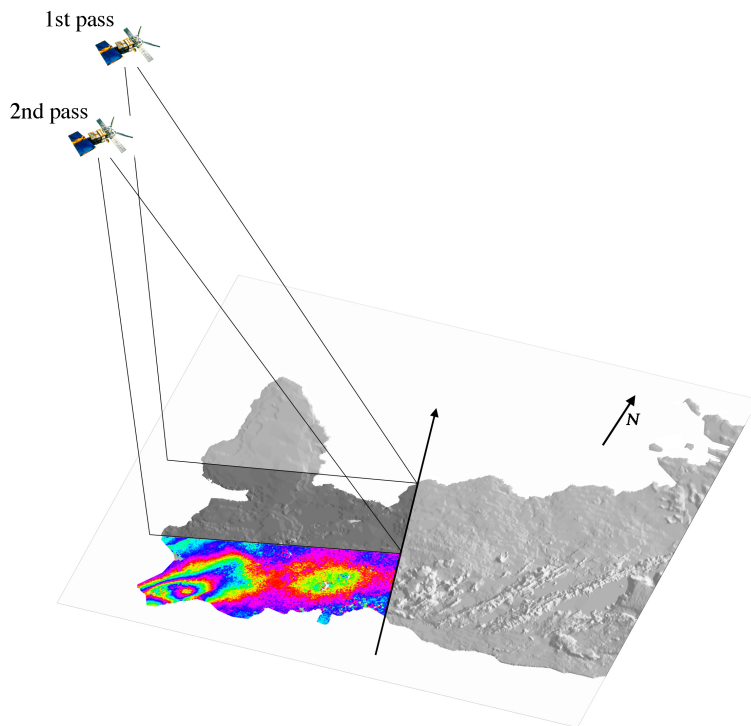
Figure 1.7: Schematic figure of two ascending SAR passes covering the southwestern Reykjanes Peninsula. The viewing angle for the ascending satellite is approximately N78°E.

If two SAR images are acquired from approximately the same position in space, that is, within a distance of up to a few hundred meters, then the images can be combined to give an interfered image, a so-called InSAR image (Figure 1.7). Each pixel in the InSAR image has a measurement of amplitude and a measurement of phase. The amplitude of the echo is a measure of the ground surface reflectivity and speckle. The phase is the two-way propagation phase delay, which provides a measure of the change in the line-of-sight distance to the ground between the two acquisitions.

The phase difference ϕ between the two acquisitions is proportional to the difference in the range Δr between the sensor and the ground

$$\phi = -\frac{4\pi}{\lambda}\,\Delta r, \tag{1.2}$$

where λ is the wavelength of the signal. The minus sign is due to the definition of ϕ as the phase delay. The measured phase is the 2π modulus of the absolute phase. Hence, the phase relative to some point in the image must be determined by integration of the phase difference between all neighboring pixels in the interferogram, a process referred to as phase unwrapping.

The measured phase depends on both topography and surface deformation. If there is no surface deformation between two acquisitions, then the topography can be estimated by subtracting the phase due to the Earth reference ellipsoid from the measured phase. In case there is surface deformation between two acquisitions, then the phase due to deformation can be estimated by subtracting both the phase due to the reference ellipsoid and the phase due to topography.

Persistent scatterer and small baselines methods

Each ground resolution element contains a number of different reflectors, or scatterers, hence the pixel amplitude and phase are always the sums of the echoes from all scatterers within that particular ground resolution element. Coherent radar echoes, that is, those with measurable amplitude and phase, will be correlated if each represents nearly the same interaction with a scatterer or a set of scatterers (Zebker and Villasenor, 1992). However, the sum of the scatterers depends on the geometry, so differences in position and orientation of the master and slave sensor result in decorrelation, referred to as spatial decorrelation.

Further decorrelation is caused by physical changes at the surface, particularly changes in vegetation, and referred to as temporal decorrelation. Another important limitation to InSAR is the delay of the signal due to varying atmospheric conditions.

The problems of spatial and temporal decorrelation can be addressed by processing multiple acquisitions, using either a persistent scatterer or a small baseline approach. The persistent scatterer (PS) method identifies resolution elements that are dominated by the echo from a single bright scatterer and therefore have little decorrelation due to changes in satellite geometry or variations in the less bright scatterers. The small baselines (SB) method, on the other hand, minimises the decorrelation by considering the phase from interferograms with short time spans (temporal baselines) and small perpendicular difference between the positions of the acquiring satellites (spatial baselines). In this project, InSAR data are processed using the multi-temporal StaMPS/MTI software (Hooper et al., 2007; Hooper, 2008), which invokes both a PS and SB approach. The combination of the two data sets has the potential for improving the spatial sampling considerably, and thereby increase the resolution of deformation signals and aid a more reliable phase unwrapping.

Image processing

Before PS and SB processing the interferograms are formed using the Doris software (Kampes et al., 2003). For the single-master PS processing a master is chosen that minimises the sum of decorrelation of all interferograms. The decorrelation depends on the time interval, the perpendicular baseline, the difference in Doppler centroid frequency, as well as thermal noise which can usually be assumed constant. For the SB processing, a number of interferograms are formed with varying master images.

Each of the slave images is resampled to the master geometry to eliminate the difference in geometry of the images. The phase due to the difference in position and orientation of the master and slave sensor is corrected for in two steps. First, the reference ellipsoid (here we use WGS84) is estimated and subtracted, a process referred to as flattening. Second, the interferograms are corrected for the phase due to the elevation of the real surface above the reference ellipsoid, using an independently determined Digital Elevation Model (DEM). This step introduces
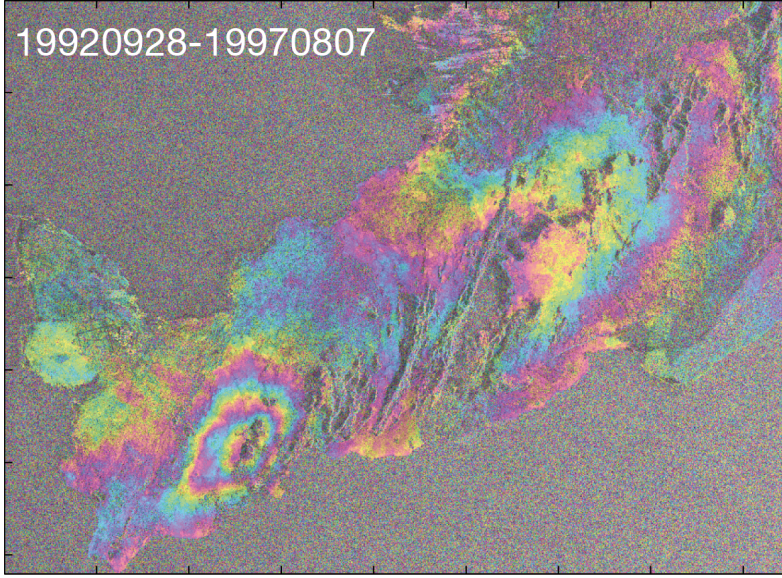
Figure 1.8: A wrapped interferogram of the Reykjanes peninsula spanning 28 September 1992 - 7 August 1997, from ERS descending track 138. The interferogram shows two full fringes (∼5 cm) of subsidence in the line-of-sight direction around the Svartsengi power plant.

the look angle error, which is almost entirely due to error in the DEM, hence it is commonly referred to as the DEM error. Finally, the radar coded positions are converted to geocoded coordinates, that is, to a known reference system, using the orbital parameters and the DEM.

Both PS and SB pixels are defined by their phase stability, and the algorithm used to identify the pixels is the same. The pixels that may be selected as stable-phase pixels are those where the noise is small enough that it does not completely obscure the signal. Apart from the noise, the measured phase has spatially correlated contributions from the phase due to ground displacement, temporal variations in atmospheric delay, orbital inaccuracies and DEM errors, which can be estimated through bandpass filtering of adjacent pixels. A spatially uncorrelated look angle error, which includes spatially uncorrelated DEM error and an error due to the deviation in the position of the pixel phase cen-

tre from its physical centre, can be estimated through its correlation with the perpendicular baseline length. Once the spatially correlated and uncorrelated contributions have been estimated and subtracted, the stable-phase pixels can be selected with a threshold determined by the user. The PS and SB data sets are then combined and the phase unwrapped using a statistical cost flow algorithm applicable to single- or multiple-master time series (Hooper et al., 2009). Finally, the unwrapped phase is corrected for atmosphere, orbit and DEM errors, using a combination of temporal and spatial filtering (Hooper et al., 2007).

1.2.3 Surface deformation modelling

The observed surface deformation can provide important information about the sub-surface deformation sources. This is done through modelling by approximating the observed deformation using Earth models with simplified source geometries and rheology. The use of simplified source geometries, such as a spherical or rectangular source, is justified when the distance from the source to the observation is large enough that the irregularities of the source have negligible effect on the resultant displacement field. This is due to the fact that the rocks surrounding the source act as a low-pass filter on the details of the source (Dvorak and Dzurisin, 1997). Simplified rheologies are also commonly assumed, for example, isotropic elastic rheology is often applied in crustal deformation models. The behaviour of the Earth depends mainly on the temperature and the time scale of the deformation processes. On short time scales of seconds to hours (for example, earthquake faulting or the passing of seismic waves), the Earth behaves elastically, with some imperfections due to delayed elastic response (e.g. Ranalli, 1995). On time scales of months to years (for example, post-seicmic deformation) or at elevated temperatures (volcano processes), the viscous behaviour of the Earth must be taken into account. On very long time scales of thousands of years (plate tectonics), the rheology of the lithosphere is elastic or high-viscous viscoelastic, while the mantle behaves viscously.

Several analytical solutions have been derived that relate elastic half-space sources to the resulting displacements or velocities at the surface. Commonly, earthquake sources or the deformation at plate boundaries are described by approximating the sources with rectangular dislocations (Okada, 1985). The dislocation source is defined by ten parameters, of which seven are related to the

geometry and location of the dislocation, and three parameters describe the deformation in terms of strike-slip, dip-slip and opening. Volcanic studies often apply the point pressure source (Mogi, 1958), which is a point source defined by its 3D location and volume change, or the finite ellipsoidal pressure source (Yang et al., 1988), defined by seven parameters related to its geometry and location and the pressure at the surface of the ellipsoid. During recent years, the vast increase in geodetic observations of crustal deformation has allowed more detailed modelling, typically using finite elements, to distinguish between complicated source geometries and heterogeneous Earth properties (e.g. Masterlark and Hughes, 2008; Pedersen et al., 2009).

In general, surface deformation is a non-linear function of the model geometry and source location. A robust non-linear optimisation scheme for obtaining the optimal model parameters is to use a simulated annealing algorithm, followed by a derivative-based method (e.g. Cervelli et al., 2001). The simulated annealing performs a random search through the model parameter space and finds the valley containing the global minimum in the multidimensional misfit space, while the randomness permits it to escape local minima. The result from the simulated annealing is then passed to the derivative-based algorithm, which finds the bottom of the misfit valley. The mean and confidence intervals of the model parameters can for example be estimated using a bootstrap algorithm, that performs the optimisations on a large number of randomly resampled data sets and compute the confidence intervals from the range of the estimated optimal parameters (Efron and Tibshirani, 1986). The bootstrap algorithm provides a reasonable measure of the confidence intervals and gives important information on correlations between the model parameters.

1.2.4   Earthquake analysis

Continuous instrumental earthquake recordings have been carried out in Iceland since 1926. During 1926–1951, only one seismometer was operating in Iceland, a Mainka instrument installed in Reykjavík, but a seismic network was initiated in 1951. The catalogue for southwest Iceland is assumed to be complete down to magnitude 4 from 1926, and down to magnitude 2.5 during 1967–1990. Since 1990, earthquakes in Iceland have been recorded by the SIL seismic network, operated by the Icelandic Meteorological Office (Bödvarsson et al., 1999; Jakob-

sdóttir, 2008). The SIL network is optimised for micro-earthquakes and records events down to M_L less than zero in the areas with the densest network. The routine SIL analysis determines both earthquake locations and magnitudes as well as focal mechanisms for all events. The focal mechanisms are estimated assuming a double-couple source, using both spectral amplitudes for P, SV, and SH waves and P wave polarities (Rögnvaldsson and Slunga, 1993). In addition to the optimal solution, the SIL algorithm provides a range of acceptable focal mechanisms, within some confidence level of the optimal mechanism.
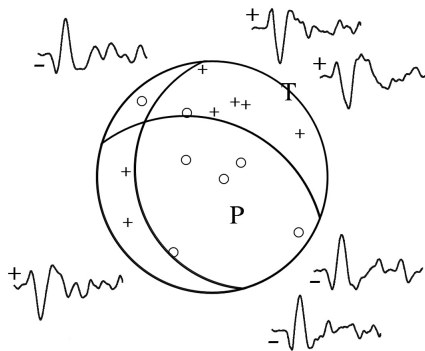
Figure 1.9: The earthquake focal mechanism is a lower-hemisphere stereographic projection showing the distribution of the seismographs around the earthquake epicentre and the first motions of the waveforms, circles indicate that the first motion was down, plusses indicate first motion up. P is the compressive axis, and T is the tensile axis.

The earthquake data spanning more than 80 years provide direct evidence of the long-term seismotectonic processes acting along the plate boundary, while the large amount of data available from the SIL catalogue allow detailed analysis of the seismicity during recent years. Important insight in the brittle deformation can be obtained by studying the spatial and temporal clustering of earthquakes as well as their focal mechanisms. Additional information is gained through standard seismological analysis, such as b-values, which is a measure of the ratio of small to large earthquakes. Moreover, the earthquake data from the SIL catalogue have been used for detailed mapping of the seismogenic structures using relative relocation (Hjaltadóttir and Vogfjörd, 2005, 2006).

1.2.5   Stress tensor inversion

The geometric information from the earthquake focal mechanisms can be used to estimate the causative state of stress in the crust where the earthquakes occur. Stress is defined as the vector force acting on three orthogonal surfaces, and the stress state is often visualised as the forces acting on the sides of an infinitesimal cube (Figure 1.10).
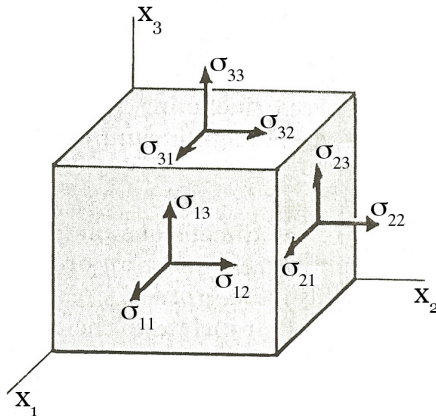
Figure 1.10: The nine stresses acting on an infinitesimal cube.

Each stress vector is decomposed into three components acting normal or perpendicular to the surface, giving a total of nine stresses. However, it is usually assumed that there is no rotation (i.e. $\sigma_{ij} = \sigma_{ji}$), hence the stress tensor is symmetric and has only six independent components. The symmetric stress tensor is orthogonally diagonalizable with the real eigenvalues $\sigma_1 > \sigma_2 > \sigma_3$, that is, the three principal stresses.

A single focal mechanism reflects the coseismic strain associated with that particular event, but the P and T axes from a fault plane solution may vary significantly from the principal stress directions depending on the orientation of the fault plane within the stress field (McKenzie, 1969). By using several focal mechanisms it is possible to search for the stress state that is compatible with all the observations, and calculate the optimal solution that minimises the difference between the observation and prediction (e.g. Gephart and Forsyth, 1984).

In this project, focal mechanisms from the SIL seismic catalogue are inverted for the state of stress using the inversion scheme of Lund and Slunga (1999), which takes advantage of some of the special features of the SIL system. Prior to the stress inversion, closely located events with similar focal mechanisms are identified using the amplitude correlation method of (Lund and Bödvarsson, 2002). A group of similar events does not contribute more than one data point to the inversion, hence all but the most well-determined event are excluded. Not including these redundant events produces a more reliable estimate of the confidence limits of the optimal stress tensor and significantly reduces the computing time. The amplitude correlation also gives important information on the nature of the seismicity.

All methods of stress tensor inversion are based on two fundamental assumptions: that faults slip in the direction of maximum shear traction on the fault plane (Bott, 1959), and that the state of stress is homogeneous within the time and space of the inverted events. The stress tensor inversion uses the geometric information of strike, dip and rake of the fault plane solutions to estimate four of the six independent components of the stress tensor, namely the directions of the three principal stress axes, as well as the relative size of the stresses, $R = (\sigma_1 - \sigma_2)/(\sigma_1 - \sigma_3)$. The remaining two components of the stress tensor, the magnitude of the maximum shear stress $(\sigma_1 - \sigma_3)/2$ and the isotropic lithostatic component, cannot be estimated without additional information on the stress magnitudes or on the shear modulus, pressure and the average depth.

The stress tensor inversion scheme minimises the absolute angle, within the fault plane, between the directions of computed shear stress $\boldsymbol{\tau}$ and observed slip $\mathbf{s}$, $\alpha = \arccos(\boldsymbol{\tau} \cdot \mathbf{s})$. In the principal stress coordinate system the shear stress on a plane with normal $\mathbf{n} = (n_1, n_2, n_3)$ can be expressed as

$$\boldsymbol{\tau} = (\sigma_1 - \sigma_3)\big(K\, n_1, (K - R)\, n_2, (K - 1)\, n_3\big) \tag{1.3}$$

where R is the relative size of the principal stresses defined above and $K = n_3^2 + R\, n_2^2$. This formula shows that the direction of maximum shear stress only depends on the orientation of the plane in the stress field and the ratio R, hence it can be calculated for each tested stress state.

The inversion algorithm performs a grid search through the principal stress directions and values of R. During inversion, a given fraction of the acceptable

focal mechanisms from the SIL catalogue is included for each event to account for the uncertainty in the focal mechanism estimates. Hence, for each stress tensor a range of acceptable focal mechanisms for all events are considered. For each of the considered focal mechanisms, the fault plane is selected from the two nodal planes as the plane with the highest relative Coulomb failure stress. The misfit α is computed for the selected fault plane of each considered focal mechanism, and the focal mechanism that best fits the tested stress tensor is chosen for each event. Then the misfits for all events are added into a final misfit for the tested stress tensor. When the entire grid has been searched, the confidence limits of the best fitting stress tensor are computed, using statistics for one-norm misfits (Parker and McNutt, 1980). Finally, the directions of greatest and least compressive horizontal stress is computed from the optimal stress tensor (Lund and Townend, 2007).

1.3 Outline of work

1.3.1 Summary of first paper

In this paper, we use annual GPS observations on the Reykjanes Peninsula from 2000–2006 to generate maps of the velocity and strain rate fields of the active plate boundary zone. The data set includes around 50 campaign stations that each has been observed at least three times during 2000–2006, and six continuous GPS stations. The GPS data reveal coseismic deformation due to a $M_W 5.0$ earthquake that occurred in the Krísuvík area on 23 August 2003, deformation due to plate motion and local subsidence around the Svartsengi geothermal power plant.

The August 2003 $M_W 5.0$ earthquake caused coseismic horizontal displacements of up to 11 mm on nearby GPS stations. The observed coseismic offsets can be modelled using a rectangular uniform-slip dislocation (Okada, 1985), which predicts right-lateral strike-slip on a N–S trending near-vertical fault. We correct the velocities on the Reykjanes Peninsula for the coseismic offsets due to the August 2003 earthquake and use the velocities to derive a kinematic model for the plate boundary (Figure 1.11), based on the work by Árnadóttir et al. (2006).

The plate boundary is modelled as a series of vertical dislocations with left-lateral motion and opening, while local subsidence around the Svartsengi power plant is approximated using a point pressure source (Mogi, 1958). The optimal model predicts left-lateral motion of 18^{+4}_{-3} mm/yr and opening of 7^{+3}_{-2} mm/yr below a locking depth of 7^{+1}_{-2} km (95% confidence levels). The resulting deep motion of 20^{+4}_{-3} mm/yr in the direction of N(100^{+8}_{-6})°E agrees well with the predicted relative North America - Eurasia rate (DeMets et al., 1994; Sella et al., 2002). This conclusion is consistent with an early geodetic study using electronic distance measurements from 1968–1972, which indicated that a combination of left-lateral motion and extension is accommodated on the Reykjanes Peninsula (Brander et al., 1976). In an earlier GPS study on the peninsula, the velocities observed
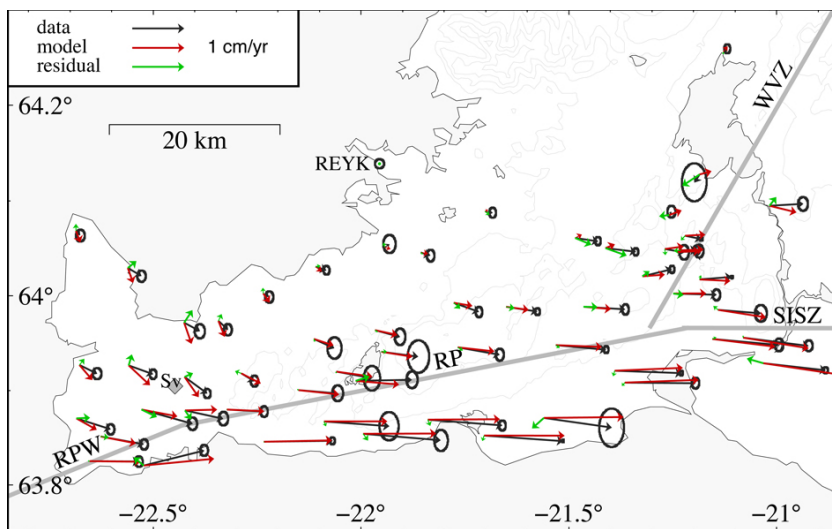
Figure 1.11: Observed horizontal GPS velocities during 2000–2006 and results of kinematic plate boundary modelling. The velocity arrows show observations (black, 2σ confidence ellipses), predictions (red), and residuals (green). The model dislocations are shown with thick gray lines, Reykjanes Peninsula West (RPW), Reykjanes Peninsula (RP), South Iceland Seismic Zone (SISZ), Western Volcanic Zone (WVZ), and the Svartsengi (Sv) point source is shown with a gray diamond.

during 1993–1998 were modelled using a simple screw dislocation model which only allows transform motion, leading to the conclusion that little extension was observed across the peninsula (Hreinsdóttir et al., 2001). Our more complicated kinematic model indicates that significant opening is in fact occurring, and that the observed deformation during 2000–2006 is consistent with the plate motion models.

Strain rate fields are estimated from the 1993–1998 and 2000–2006 velocities (Figure 1.12), using the method of Haines et al. (1998). The strain rate fields capture details that are difficult to see directly from the velocity fields, and reveal spatial and temporal variations within the plate boundary zone. During 1993–1998, high shear strain rates and areal expansion are observed on the eastern part of the peninsula, indicating that widening occurred across the Hengill fissure swarm as a result of an inflation of the volcanic system during 1994–1998.

During 2000–2006, a pronounced zone of high shear strain rates is observed on the central part of the peninsula, in areas characterised by high background seismicity. The strain rate fields on the western part of the peninsula during both periods mainly reflect the subsidence around the Svartsengi geothermal power plant, which induces both areal contraction and horizontal shear.
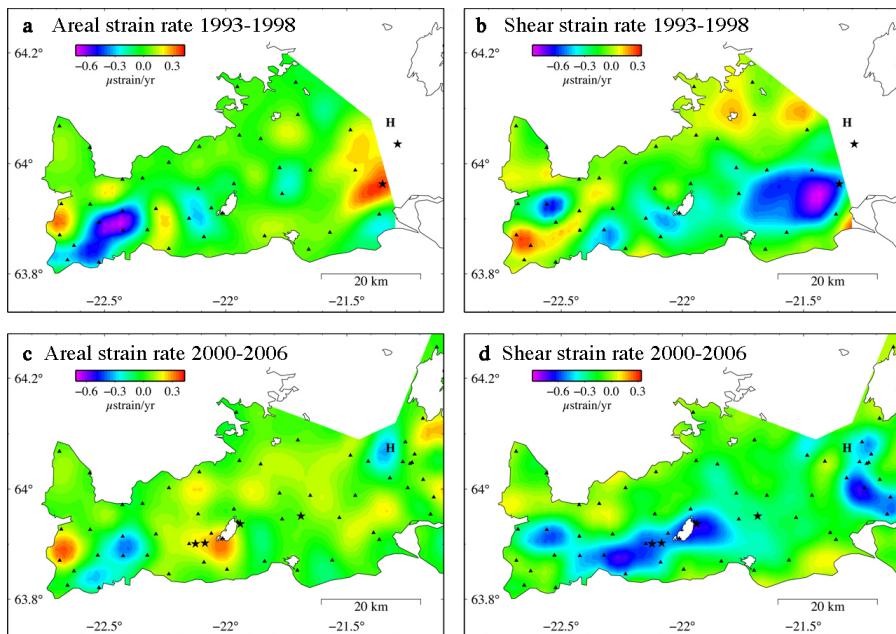
Figure 1.12: Areal $(\frac{1}{2}(\dot{\epsilon}_{xx} + \dot{\epsilon}_{yy}))$ and shear $(\dot{\epsilon}_{xy})$ strain rates for 1993–1998 and 2000–2006. The black triangles show the locations of the GPS stations that were surveyed during each period. The central Hengill volcano is marked (H). The stars show epicentres of $M_W 5$ earthquakes in 1998, 2000 and 2003.

In summary, we find that the surface deformation on the Reykjanes Peninsula is consistent with oblique plate boundary motion on a regional scale, although considerable temporal and spatial strain rate variations due to shallow sources are observed within the plate boundary zone.

1.3.2 Summary of second paper

This paper presents the first comprehensive analysis of the seismicity on the Reykjanes Peninsula. We compile a data set of all $M_L \geq 4$ earthquakes on the peninsula since early instrumental earthquake recordings in Iceland in 1926 (Figure 1.13), in order to evaluate the long-term seismotectonic processes of the plate boundary. The seismicity on the peninsula shows a systematic change from primarily earthquake swarms in the west to mainshock-aftershock sequences in the east, reflecting the transition from the seafloor spreading along the Reykjanes Ridge to the transform motion in the South Iceland Seismic Zone. We use the compilation of $M_L \geq 4$ earthquakes to obtain an estimate of the seismic moment release along the peninsula and compare the seismic moment to the estimated
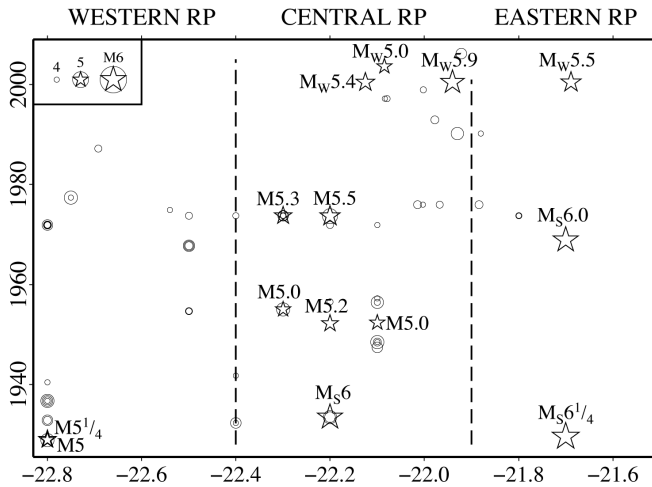
Figure 1.13: Time versus longitude plot of $M_L \geq 4$ earthquakes on the Reykjanes Peninsula during 1926–2006. The magnitudes are Icelandic local magnitude (M_L), unless otherwise indicated. The stars indicate mainshocks, circles are swarms or undefined events.

moment accumulation from plate motion. The estimated moment accumulation and release agree well on the central and eastern parts of the peninsula, but some discrepancy between the moments is observed on the western part of the peninsula, probably related to aseismic moment release.

For the time period 1997–2006, we use earthquake locations, magnitudes and focal mechanisms for more than 16,000 earthquakes from the SIL seismic catalogue for a detailed analysis of the seismicity. During 1997–2006, most earthquakes on the Reykjanes Peninsula were located in two areas, Fagradalsfjall and Krísuvík on the central part of the peninsula. Pronounced swarm activity was observed in both areas, as well as moderate mainshocks in the Krísuvík area. The Krísuvík area is an active geothermal field, suggesting that geothermal activity has some influence on the seismicity in this area.

We estimate the state of stress from inversion of micro-earthquake focal mechanisms from the SIL catalogue. The state of stress is mainly oblique strike-slip, with a tendency towards a normal stress state, consistent with the obliquity of the plate boundary. We map the directions of least compressive horizontal stress (S_{hmin}) using stress inversions of small clusters of earthquakes, and compare the S_{hmin} directions to the directions of greatest extensional strain rate ($\dot{\epsilon}_{Hmax}$), derived from GPS velocities spanning 2000–2006 (Keiding et al., 2008). The S_{hmin} directions trend consistently ESE with an average of N(120±6)°E, in excellent agreement with the $\dot{\epsilon}_{Hmax}$ directions, which average N(121±3)°E in the areas with earthquakes and stress data (Figure 1.14). The agreement between the directions of stress at depth and strain rate observed at the surface indicates that the earthquakes are primarily driven by plate motion, although there may be geothermal fluid triggering effects in the Krísuvík area.
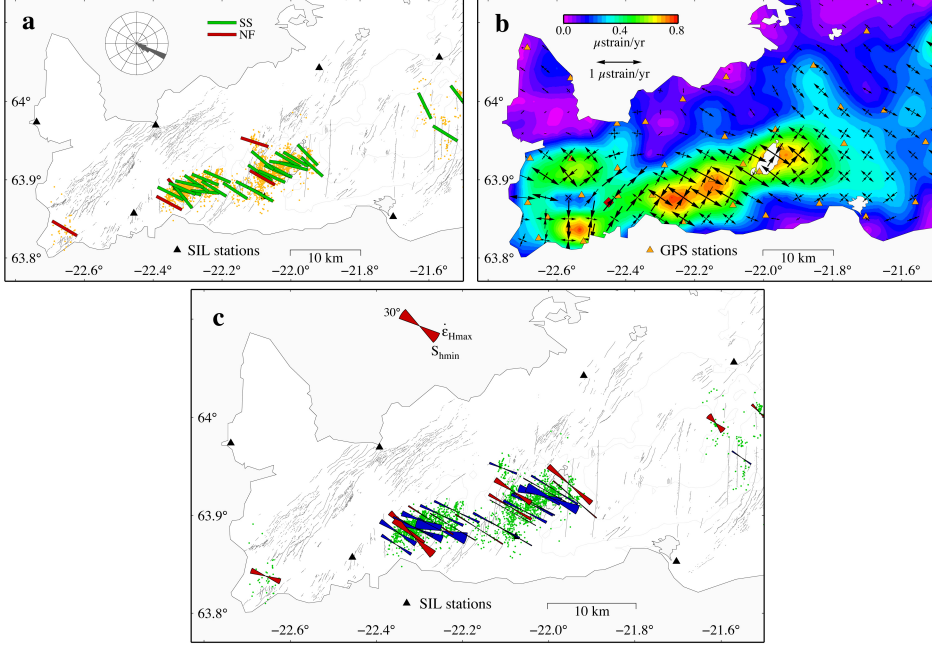
Figure 1.14: a) Estimated directions of S_{hmin} from stress inversions of earthquake focal mechanisms during 2000–2006. The bars are coloured according to stress state: strike-slip (green) and normal (red). Yellow dots show the earthquakes that were included in the inversions. The inset rose diagram shows the directions of S_{hmin} in $10°$ bins. b) Geodetic strain rates computed from 2000–2006 GPS velocities. The greatest extensional ($\dot{\epsilon}_{Hmax}$) and contractional ($\dot{\epsilon}_{hmin}$) horizontal strain rates are shown with the arrows, while the magnitude of the maximum horizontal shear strain rate, $\frac{1}{2}(\dot{\epsilon}_{Hmax} - \dot{\epsilon}_{hmin})$, is shown by the contours. c) Comparison of the S_{hmin} directions in panel a and the $\dot{\epsilon}_{Hmax}$ directions in panel b. The bow-ties show the differences between the orientations of S_{hmin} and $\dot{\epsilon}_{Hmax}$, with the radii scaled to the magnitudes of the maximum shear strain rate, and fill colours indicating whether S_{hmin} is oriented clockwise (red) or counter-clockwise (blue) to $\dot{\epsilon}_{Hmax}$. Green dots are earthquakes.

1.3.3   Summary of third paper

Keiding, M., T. Árnadóttir, S. Jónsson, J. Decriem, and A. Hooper, 2009. Plate boundary deformation and man-made subsidence around geothermal fields on the Reykjanes Peninsula, Iceland, *to be submitted to J. Volcanol. Geoth. Res.*

In this paper, we examine the crustal deformation on the Reykjanes Peninsula during 1992–2009, using InSAR and GPS data. The geodetic data show deformation due to the plate motion, anthropogenic subsidence around the Reykjanes, Svartsengi and Hellisheidi geothermal fields and, possibly, increasing pressure in the Krísuvík geothermal system.

Figure 1.15 shows the mean descending line-of-sight (LOS) velocity fields for the time periods 1992–1999, 2003–2005 and 2006–2009. All three images show increasing LOS rates moving from north to south across the peninsula, as illustrated with the profiles perpendicular to the trend of the plate boundary in the bottom panel of Figure 1.15. This increase in LOS rates is at least in part due to the increase in eastwards velocities across the plate boundary zone. A subtle zone of negative LOS rates is observed along the central part of the peninsula during 2003–2005 and 2006–2008, with negative rates of 0–4 mm/yr relative to Reykjavík, most likely reflecting subsidence due to the extension across the plate boundary. During 2006–2008, a marked signal of negative LOS rates appears around the Reykjanes geothermal field, reflecting subsidence caused by geothermal fluid extraction in the new Reykjanes power plant. Negative LOS rates are also observed around the new power plant in the Hellisheidi field in the east. Finally, an anomaly of positive LOS rates is observed in the Krísuvík area on the central part of the peninsula, probably due to increasing pressure in the Krísuvík geothermal system.

We investigate the subsidence around the Reykjanes field on the western Reykjanes Peninsula in more detail. Figure 1.16 shows the near-vertical radar displacements field during June 2005 – May 2008, obtained from addition of ascending and descending LOS rates. The Reykjanes subsidence signal is clearly elongated in the NE–SW direction, thus aligning with the trend of the fractures in the area. The elongation of the subsidence bowl shows that the permeability in the reservoir is highly anisotropic. We model the observed surface subsidence using point and ellipsoidal sources in elastic half-space and find that the Reykjanes subsidence
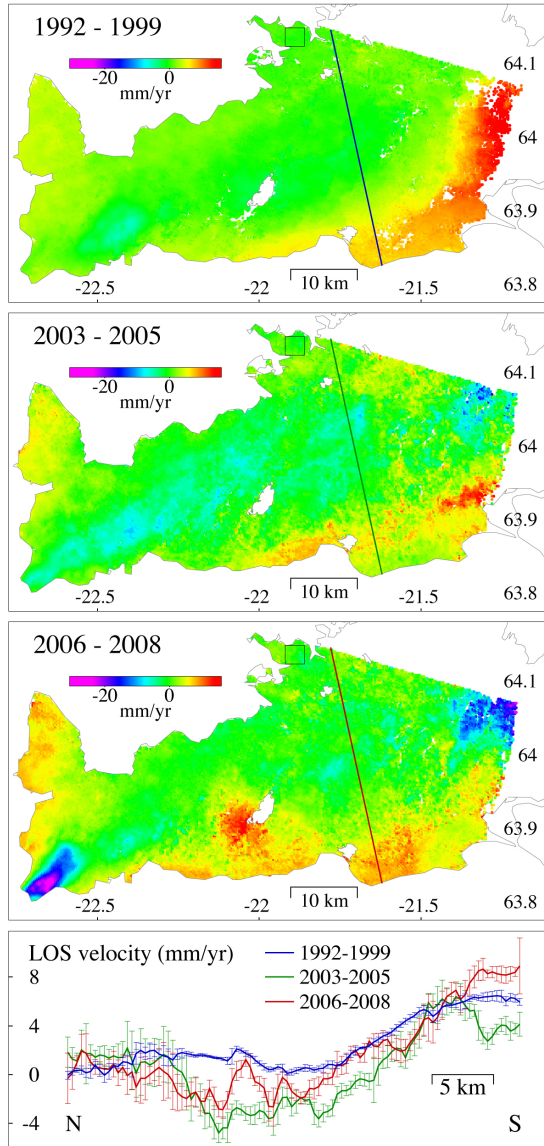
Figure 1.15: Residual mean LOS velocity fields after removal of bilinear ramps, relative to the mean value during each period in the area near Reykjavík (shown with the box). The time spans of the images are 11 May 1992–16 Sep 1999 (18 ERS images), 25 Sep 2003–29 Sep 2005 (9 Envisat images) and 6 Jul 2006–1 May 2008 (9 Envisat images). The profiles in the bottom panel show moving averages of the mean LOS rates and 1σ standard deviations along the line shown on the maps.

can be fitted well using three ellipsoidal sources. Two of the sources are elongated in the horizontal NE–SW direction and located at 1.1–1.6 km depth, within the depth range of the production bore holes in the area. The third source, which has the largest volume change, is plunging steeply and centred at a larger depth of 4 km. Thus the modelling indicates that water flows to the well field primarily from below, but there is also considerable lateral flow due to the anisotropic permeability.
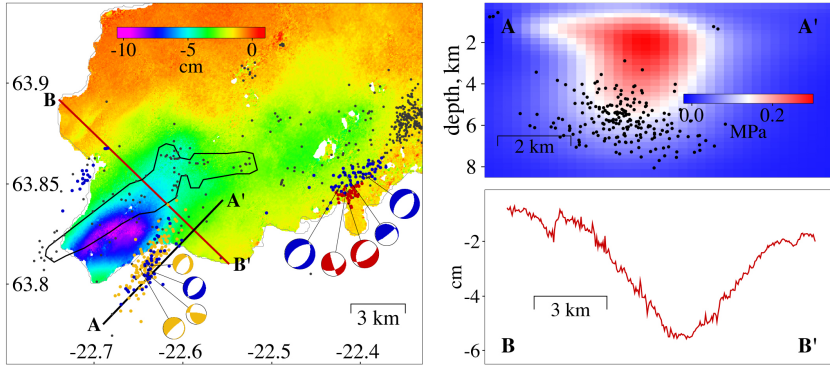
Figure 1.16: Close-up on the near-vertical radar displacement field during June 2005 – May 2008, computed from the addition of ascending and descending InSAR data. Earthquake locations and focal mechanisms from the SIL seismic catalogue are shown as background events (small black dots), and distinct swarm events in 2006 (orange), 2007 (red) and 2008 (blue). Also shown are focal mechanisms for some of the largest swarm events with local magnitudes ranging 2.9–4.1. The black outline shows the approximate location of the 1972 swarm activity (redrawn from Klein et al., 1977, their Figure 5). Profile AA' shows the predicted change in Coulomb failure stress, for normal slip on NE-SW trending fault planes, computed from a three-ellipsoid elastic halfspace model for the subsidence around the Reykjanes geothermal field. Profile BB' shows the observed near-vertical radar displacement across the Reykjanes subsidence bowl.

Interestingly, a change in the pattern of seismicity is observed following the start of production in the Reykjanes power plant (see Figure 1.16). During the first months after the start of production, the SIL seismic network recorded three short-lived earthquake swarms SE of the tip of the peninsula, along the periphery of the subsidence bowl. The contraction in geothermal reservoirs stresses the surrounding crust and can in some cases trigger earthquakes, as discussed by

Segall and Fitzgerald (1998) and Fialko and Simons (2000). Our three-ellipsoid elastic half-space model indicates that the Coulomb Failure Stress for normal faulting on NE-trending planes along profile AA' in Figure 1.16 can have increased by 0.3 MPa, which may be enough to trigger earthquakes. Thus, the earthquake swarms most likely occurred as a result of the geothermal fluid extraction at the Reykjanes power plant. Subtle discontinuities that probably reflect aseismic fault movement are observed near the NW and SE ends of near-vertical displacement profile BB' in Figure 1.16.

1.4   Concluding remarks

Plate tectonics has established itself as the most fundamental concept of modern-day geology and geophysics by explaining most first-order geophysical observations on Earth in a self-consistent manner (Kreemer et al., 2003). The concept of plate tectonics is based on the assumptions of rigid plates and narrow plate boundary zones (1–60 km). However, many plate boundaries in both continental and oceanic lithosphere are not narrow but are hundreds to thousands kilometers wide, and plate boundary zones cover approximately 15% of the Earth's surface area (Gordon and Stein, 1992). During recent years, the vast increase in geodetic observations of crustal deformation has considerably improved our understanding of the dynamics of plate boundary zones. Furthermore, the earthquake catalogues are being unified and expanded in time (e.g. Grünthal et al., 2009), making it possible to relate the distributed strain at the surface with the discrete brittle deformation at depth.

Although the Icelandic plate boundary is relatively narrow (less than 100 km) compared to many continental plate boundary zones, considerable spatial and temporal complexity is observed within its deforming zones. The most recent rifting episode in Iceland, the 1975–1984 Krafla fires in the Northern Volcanic zone, caused more than 9 meters of extension across the rift zone, corresponding to 450 years of accumulated plate motion (Tryggvason, 1994). The first paper of this thesis demonstrates that the regional surface deformation field on the Reykjanes Peninsula is consistent with the long-term plate spreading. However, it is quite likely that the periodic eruptive activity will alter the stress field and cause a strain pattern that is different from that of the present steady-state strain field. Detailed mapping of the fractures on the Reykjanes Peninsula does in fact reveal structural complexity that can be reconciled with magmatic periodicity (Clifton and Kattenhorn, 2006).

The integration of geodetic and seismological data has great potential for improving our understanding of the seismotectonic processes acting along Earth's active plate boundaries. To date, only a few studies have compared geodetic strain rates with stress estimates obtained from earthquake data (e.g. Townend and Zoback, 2006). In the second paper of this thesis we compare the directions of strain rate observed by GPS with the directions of stress inferred from earthquake focal mechanisms along the Reykjanes Peninsula, and find that the stress driving

the earthquakes is consistent with the stress due to plate motion. This novel approach provides new and detailed information about the driving mechanisms behind the earthquakes, and could be applied in other active regions. In the case of the Reykjanes Peninsula it is still an unresolved question if there are particular triggering mechanisms behind the seismicity. The geothermal activity in the Krísuvík area is likely to affect the seismicity, and the existence of a buried geothermal system in the Fagradalsfjall area could explain the pronounced swarm activity there.

The fluid extraction from geothermal fields enables us to gain insight in the dynamics of the fluid migration in the sub-surface reservoirs. The third paper of this thesis demonstrates that there are strong structural constraints on the fluid migration in the Reykjanes geothermal field, as the geothermal water tends to flow along high-permeable zones parallel to the fractures in the area. One of the main unanswered questions about the dynamics of the Reykjanes Peninsula plate boundary is how much the structures, for example the fractures formed under periods of magmatic activity, influence the surface deformation due to plate spreading during the present non-magmatic period. This question can only be resolved if more detailed observations of the surface deformation are obtained and analysed through advanced modelling techniques.

Bibliography

Altamimi, Z., X. Collilieux, J. Legrand, B. Garayt and C. Boucher, 2007. ITRF2005: A new release of the International Terrestrial Reference Frame based on time series of station positions and Earth Orientation Parameters. *J. Geophys. Res.*, **112**, B09401. doi:10.1029/2007JB004949.

Árnadóttir, T., H. Geirsson and P. Einarsson, 2004. Coseismic stress changes and crustal deformation on the Reykjanes Peninsula due to triggered earthquakes on 17 June 2000. *J. Geophys. Res.*, **109**, B09307. doi:10.1029/2004JB003130.

Árnadóttir, T., W. Jiang, K. L. Feigl, H. Geirsson and E. Sturkell, 2006. Kinematic models of plate boundary deformation in southwest Iceland derived from GPS observations. *J. Geophys. Res.*, **111**, B07402. doi:10.1029/2005JB003907.

Bödvarsson, R., S. T. Rögnvaldsson, R. Slunga and E. Kjartansson, 1999. The SIL data acquisition system - at present and beyond year 2000. *Phys. Earth Planet. Inter.*, **113**, 89–101.

Bott, M. H. P., 1959. The mechanics of oblique slip faulting. *Geol. Mag.*, **96** (2), 109–117.

Brander, J. L., R. G. Mason and R. W. Calvert, 1976. Precise distance measurements in Iceland. *Tectonophysics*, **31**, 193–206.

Bürgmann, R., P. A. Rosen and E. J. Fielding, 2000. Synthetis Aperture Radar Interferometry to measure Earth's surface topography and its deformation. *Annu. Rev. Earth Planet. Sci.*, **28**, 169–209.

Cervelli, P., M. H. Murray, P. Segall, Y. Aoki and T. Kato, 2001. Estimating source parameters from deformation data, with an application to the March 1997 earthquake swarm off the Izu Peninsula, Japan. *J. Geophys. Res.*, **106** (B6), 11,217–11,238.

Clifton, A. E. and S. A. Kattenhorn, 2006. Structural architecture of a highly oblique divergent plate boundary segment. *Tectonophysics*, **419**, 27–40.

Dach, R., U. Hugentobler, P. Fridez and M. Meindl, 2007. *Bernese GPS software version 5.0*. Switzerland.

DeMets, C., R. G. Gordon, D. F. Argus and S. Stein, 1994. Effect of recent revisions to the geomagnetic reversal time scale on estimates of current plate motions. *Geophys. Res. Lett.*, **21** (20), 2191–2194.

Dow, J. M., R. E. Neilan and G. Gendt, 2005. The International GPS Service (IGS): Celebrating the 10th anniversary and looking to the next decade. *Adv. Space Res.*, **36** (3), 320–326. doi:10.1016/j.asr.2005.05.125.

Dvorak, J. J. and D. Dzurisin, 1997. Volcano geodesy: the search for magma reservoirs and the formation of eruptive fissures. *Rev. Geophys.*, **35** (3), 343–384.

Efron, B. and R. Tibshirani, 1986. Bootstrap methods for standard errors, confidence intervals, and other measures of statistical accuracy. *Statistical Science*, **1** (1), 54–75.

Einarsson, P., 1991. Earthquakes and present-day tectonism in Iceland. *Tectonophysics*, **189**, 261–279.

Einarsson, P. and K. Sæmundsson, 1987. Earthquake epicenters 1982-1985 and volcanic systems in Iceland (map). In T. Sigfússon (ed.), *Í Hlutarsins Edli: Festschrift for Thorbjorn Sigurgeirsson*. Menningarsjódur, Reykjavík.

Fialko, Y. and M. Simons, 2000. Deformation and seismicity in the Coso geothermal area, Inyo County, California: Observations and modeling using satellite radar interferometry. *J. Geophys. Res.*, **105** (B9), 21,781–21,793.

Geirsson, H., T. Árnadóttir, C. Völksen, W. Jiang, E. Sturkell, T. Villemin, P. Einarsson, F. Sigmundsson and R. Stefánsson, 2006. Current plate movements across the Mid-Atlantic Ridge determined from 5 years of continuous GPS measurements in Iceland. *J. Geophys. Res.*, **111**, B09407. doi:10.1029/2005JB003717.

Gephart, J. W. and D. W. Forsyth, 1984. An improved method for determining the regional stress tensor using earthquake focal mechanism data: Application to the San Fernando earthquake sequence. *J. Geophys. Res.*, **89** (B11), 9305–9320.

Gordon, R. G. and S. Stein, 1992. Global tectonics and space geodesy. *Science*, **256** (5055), 333–342. doi:10.1126/science.256.5055.333.

Grünthal, G., R. Wahlström and D. Stromeyer, 2009. The unified catalogue of earthquakes in central, northern, and northwestern Europe (CENEC) - updated and expanded to the last millennium. *J. Seis.*, **13** (4), 517–541. doi:10.1007/s10950-008-9144-9.

Haines, A. J., J. A. Jackson, W. E. Holt and D. C. Agnew, 1998. Representing distributed deformation by continuous velocity fields. Report 98/5, Institute of Geology and Nuclear Science, Lower Hutt, New Zealand.

Herring, T. A., R. W. King and S. C. McClusky, 2006. GLOBK Reference Manual, Global Kalman filter VLBI and GPS analysis program, Release 10.3. Technical report, Massachusetts Institute of Technology, USA.

Hjaltadóttir, S. and K. S. Vogfjörd, 2005. Subsurface fault mapping in Southwest Iceland by relative location of the June 2000 earthquakes. Report no. 21, Icelandic Meteorological Office, Reykjavík.

Hjaltadóttir, S. and K. S. Vogfjörd, 2006. Mapping fractures in Fagradalsfjall on the Reykjanes Peninsula with micro-earthquakes (in Icelandic). Report no. 06001, Icelandic Meteorological Office, Reykjavík.

Hooper, A., 2008. A multi-temporal InSAR method incorporating both persistent scatterer and small baseline approaches. *Geophys. Res. Lett.*, **35**, L16302. doi: 10.1029/2008GL034654.

Hooper, A., R. Pedersen and F. Sigmundsson, 2009. Constraints on magma intrusion at Eyjafjallajökull and Katla volcanoes in Iceland, from time series SAR interferometry. In C. J. B. et al. (ed.), *The VOLUME Project, VOLcanoes: Understanding subsurface mass moveMEnt*, pages 13–24.

Hooper, A., P. Segall and H. Zebker, 2007. Persistent scatterer interferometric synthetic aperture radar for crustal deformation analysis, with application to Volcán Alcedo, Galápagos. *J. Geophys. Res.*, **112**, B07407,. doi:10.1029/2006JB004763.

Hreinsdóttir, S., T. Árnadóttir, J. Decriem, H. Geirsson, A. Tryggvason, R. A. Bennett and P. LaFemina, 2009. A complex earthquake sequence captured by the continuous GPS network in SW Iceland. *Geophys. Res. Lett.*, **36**, L12309. doi: 10.1029/2009GL038391.

Hreinsdóttir, S., P. Einarsson and F. Sigmundsson, 2001. Crustal deformation at the oblique spreading Reykjanes Peninsula, SW Iceland: GPS measurements from 1993 to 1998. *J. Geophys. Res.*, **106** (B7), 13,803–13,816.

Jakobsdóttir, S. S., 2008. Seismicity in Iceland: 1994–2007. *Jökull*, **58**, 75–100.

Kampes, B., R. Hanssen and Z. Perski, 2003. Radar Interferometry with Public Domain Tools. In *Proceedings of FRINGE 2003*. ESA ESRIN, Frascati, Italy.

Keiding, M., T. Árnadóttir, E. Sturkell, H. Geirsson and B. Lund, 2008. Strain accumulation along an oblique plate boundary: the Reykjanes Peninsula, southwest Iceland. *Geophys. J. Int.*, **172**, 861–872. doi:10.1111/j.1365-246X.2007.03655.x.

Keiding, M., B. Lund and T. Árnadóttir, 2009. Earthquakes, stress and strain along an obliquely divergent plate boundary: the Reykjanes Peninsula, southwest Iceland. *J. Geophys. Res.*, **114**, B09306. doi:10.1029/2008JB006253.

Klein, F. W., P. Einarsson and M. Wyss, 1973. Microearthquakes on the Mid-Atlantic plate boundary on the Reykjanes Peninsula in Iceland. *J. Geophys. Res.*, **78** (23), 5084–5099.

Klein, F. W., P. Einarsson and M. Wyss, 1977. The Reykjanes Peninsula, Iceland, earthquake swarm of September 1972 and its tectonic significance. *J. Geophys. Res.*, **82** (5), 865–888.

Kreemer, C., W. E. Holt and A. J. Haines, 2003. An integrated global model of present-day plate motions and plate boundary deformation. *Geophys. J. Int.*, **154**, 8–34.

Lund, B. and R. Bödvarsson, 2002. Correlation of microearthquake body-wave spectral amplitudes. *Bull. Seis. Soc. Am.*, **92** (6), 2419–2433.

Lund, B. and R. Slunga, 1999. Stress tensor inversion using detailed microearthquake information and stability constraints: Application to Ölfus in southwest Iceland. *J. Geophys. Res.*, **104** (B7), 14,947–14,964.

Lund, B. and J. Townend, 2007. Calculating horizontal stress orientations with full or partial knowledge of the tectonic stress tensor. *Geophys. J. Int.*, **170**, 1328–1335. doi:10.1111/j.1365-246X.2007.03468.x.

Masterlark, T. and K. L. H. Hughes, 2008. Next generation of deformation models for the 2004 M9 Sumatra-Andaman earthquake. *Geophys. Res. Lett.*, **35**, L19310. doi:10.1029/2008GL035198.

McKenzie, D. P., 1969. The relation between fault plane solutions for earthquakes and the directions of the principal stresses. *Bull. Seis. Soc. Am.*, **59** (2), 591–601.

Mogi, K., 1958. Relations between the eruptions of various volcanoes and the deformations of the ground surfaces around them. *Bull. Earthquake Res. Inst. Univ. Tokyo*, **36**, 99–134.

Okada, Y., 1985. Surface deformation due to shear and tensile faults in a half-space. *Bull. Seis. Soc. Am.*, **75** (4), 1135–1154.

Parker, R. L. and M. K. McNutt, 1980. Statistics for the one-norm misfit measure. *J. Geophys. Res.*, **85** (B8), 4429–4430.

Pedersen, R., F. Sigmundsson and T. Masterlark, 2009. Rheologic controls on inter-rifting deformation of the Northern Volcanic Zone, Iceland. *Earth Planet. Sci. Lett.*, **281**, 14–26. doi:10.1016/j.epsl.2009.02.003.

Ranalli, G., 1995. *Rheology of the Earth*. Chapman & Hall, London.

Rögnvaldsson, S. T. and R. Slunga, 1993. Routine fault plane solutions for local networks: A test with synthetic data. *Bull. Seis. Soc. Am.*, **83** (4), 1232–1247.

Sæmundsson, K., 1978. Fissure swarms and central volcanoes of the neovolcanic zones of Iceland. *Geol. J. Special Issue*, **10**, 415–432.

Sæmundsson, K. and S. Einarsson, 1980. Geological map of Iceland, sheet 3, SW-Iceland, second edition, scale 1:250,000.

Segall, P. and S. D. Fitzgerald, 1998. A note on induced stress changes in hydrocarbon and geothermal reservoirs. *Tectonophysics*, **289**, 117–128.

Sella, G. F., T. H. Dixon and A. Mao, 2002. REVEL: A model for Recent plate velocities from space geodesy. *J. Geophys. Res.*, **107** (B4), 2081. doi:10.1029/2000JB000033.

Sigurgeirsson, M., 1995. The Younger-Stampar eruption at Reykjanes, SW-Iceland (in Icelandic). *Náttúrufrœdingurinn*, **64**, 211–230.

Thordarson, T. and G. Larsen, 2007. Volcanism in Iceland in historical time: Volcano types, eruption styles and eruptive history. *J. Geodyn.*, **43**, 118–152.

Townend, J. and M. D. Zoback, 2006. Stress, strain, and mountain building in central Japan. *J. Geophys. Res.*, **111**, B03411. doi:10.1029/2005JB003759.

Tryggvason, E., 1973. Seismicity, earthquake swarms, and plate boundaries in the Iceland region. *Bull. Seis. Soc. Am.*, **63** (4), 1327–1348.

Tryggvason, E., 1994. Surface deformation at the Krafla volcano, North Iceland, 1982–1992. *Bull. Volc.*, **56** (2), 98–107.

Yang, X.-M., P. M. Davis and J. H. Dieterich, 1988. Deformation from inflation of a dipping finite prolate spheroid in an elastic half-space as a model for volcanic stressing. *J. Geophys. Res.*, **93** (B5), 4249–4257.

Zebker, H. A. and J. Villasenor, 1992. Decorrelation in interferometric radar echoes. *IEEE Transactions on Geoscience and Remote Sensing*, **30** (5), 950–959.

Chapter 2

Compilation of papers

Paper I

Strain accumulation along an oblique plate boundary: the Reykjanes Peninsula, southwest Iceland

M. Keiding,[1] T. Árnadóttir,[1] E. Sturkell,[1] H. Geirsson[2] and B. Lund[3]

[1]*Nordic Volcanological Center, Institute of Earth Science, University of Iceland, Reykjavík, Iceland. E-mail: marie@hi.is*
[2]*Iceland Meteorological Office, Reykjavík, Iceland*
[3]*Department of Earth Sciences, Uppsala University, Uppsala, Sweden*

SUMMARY
We use annual GPS observations on the Reykjanes Peninsula (RP) from 2000 to 2006 to generate maps of surface velocities and strain rates across the active plate boundary. We find that the surface deformation on the RP is consistent with oblique plate boundary motion on a regional scale, although considerable temporal and spatial strain rate variations are observed within the plate boundary zone. A small, but consistent increase in eastward velocity is observed at several stations on the southern part of the peninsula, compared to the 1993–1998 time period. The 2000–2006 velocities can be modelled by approximating the plate boundary as a series of vertical dislocations with left-lateral motion and opening. For the RP plate boundary we estimate left-lateral motion 18^{+4}_{-3} mm yr^{-1} and opening of 7^{+3}_{-2} mm yr^{-1} below a locking depth of 7^{+1}_{-2} km. The resulting deep motion of 20^{+4}_{-3} mm yr^{-1} in the direction of N(100^{+8}_{-6})°E agrees well with the predicted relative North America–Eurasia rate. We calculate the areal and shear strain rates using velocities from two periods: 1993–1998 and 2000–2006. The deep motion along the plate boundary results in left-lateral shear strain rates, which are perturbed by shallow deformation due to the 1994–1998 inflation and elevated seismicity in the Hengill–Hrómundartindur volcanic system, geothermal fluid extraction at the Svartsengi power plant, and possibly earthquake activity on the central part of the peninsula.

Key words: Satellite geodesy; Plate motions; Earthquake ground motions; Kinematics of crustal and mantle deformation.

1 INTRODUCTION

Iceland is the surface expression of the interaction between the Mid-Atlantic Ridge and the North-Atlantic mantle plume, which is currently located beneath the northwestern part of the Vatnajökull ice cap in central Iceland (Fig. 1). The northwest motion of the Mid-Atlantic Ridge relative to the mantle plume causes an increasing offset of the active plate boundary in Iceland from the offshore Mid-Atlantic Ridge. As a result, a considerable part of the plate boundary in Iceland is oblique, with the most pronounced obliquity on the Reykjanes Peninsula (RP). The NUVEL-1A and REVEL plate motion models predict a relative North America–Eurasia (NA–EU) rate of 19–20 mm yr^{-1} in a direction of N(101–103)°E at 63.9°N, 22.0°W (DeMets *et al.* 1994; Sella *et al.* 2002). The plate boundary is highly oblique to this direction with an approximate strike of N80°E. The obliquity of the plate boundary leads to a complex deformation zone in which both left-lateral shear and extension are accommodated. Knowledge of the surface velocity field across an active plate boundary zone is important for understanding the deep processes that are causing the surface deformation. In recent years, the amount of geodetic observations has increased considerably and made it possible to measure velocities and strain rates within diffuse plate boundary zones with high accuracy (e.g. Kreemer *et al.* 2003).

Here we present velocities calculated from annual GPS surveys on the RP during 2000–2006. We model the observed surface velocities with a 3-D dislocation model approximating the plate boundary, and show that the observed surface deformation is consistent with oblique plate boundary motion on a regional scale. We also generate maps of areal and shear strain rates, using 1993–1998 velocities from Hreinsdóttir *et al.* (2001) and 2000–2006 velocities from this study. Considerable spatial and temporal variations in elastic strain accumulation are observed within the plate boundary zone due to shallow deformation related to episodic magmatic and seismic activity, and subsidence caused by geothermal fluid extraction.

2 GEOLOGICAL BACKGROUND

The Mid-Atlantic plate boundary comes onshore on the RP and continues to the Hengill triple junction, where it splits into the Western Volcanic Zone (WVZ) and the South Iceland Seismic Zone (SISZ) (Fig. 1). Rifting along the RP and WVZ was initiated 6–7 Ma ago, after an eastward rift jump from the Snæfellsnes Peninsula (Sæmundsson 1978). The centre of spreading started migrating further east 2–3 Ma ago with the formation of the Eastern Volcanic Zone (EVZ) (Sæmundsson 1974), which is currently propagating

GJI Volcanology, geothermics, fluids and rocks
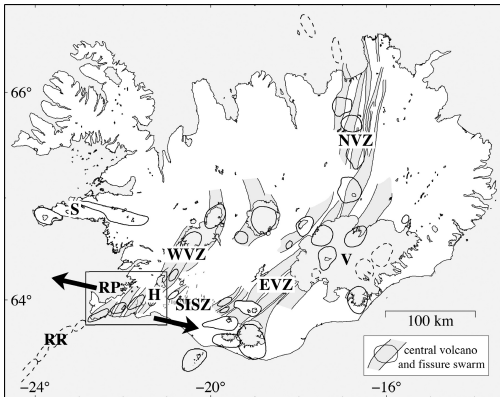
Figure 1. Tectonic map of Iceland. Central volcanoes are shown with oval outlines and volcanic fissure swarms in shaded grey (Einarsson & Sæmundsson 1987). The arrows show the predicted relative North America–Eurasia rate across the Reykjanes Peninsula from the NUVEL-1A plate model (DeMets *et al.* 1994). Reykjanes Ridge (RR), Reykjanes Peninsula (RP), Hengill (H), South Iceland Seismic Zone (SISZ), Snæfellsnes (S), Western Volcanic Zone (WVZ), Eastern Volcanic Zone (EVZ), Northern Volcanic Zone (NVZ) and Vatnajökull (V) are labelled. The box shows the location of the study area in Fig. 2.

N(40–60)°E and located either at the edges of the volcanic systems or outside of them (Clifton & Kattenhorn 2006). A number of km-scale N–S oriented right-lateral strike-slip faults lie along an E–W trending zone on the southern part of the peninsula. These faults are seismically active and accommodate left-lateral shear in the E–W direction in a similar manner as the 'book-shelf' faulting in the SISZ transform (Sigmundsson *et al.* 1995).

The seismic activity on the RP is recorded by the SIL seismic network, operated by the Icelandic Meteorological Office (e.g. Bödvarsson *et al.* 1999; Jakobsdóttir *et al.* 2002; Hjaltadóttir *et al.* 2005). The current seismicity delineates a zone that trends approximately N80°E along most of the peninsula, but the seismic zone bends towards SW at the transition to the off-shore Reykjanes Ridge. Most earthquakes occur on the central RP at 4–6 km depth, but seismicity reaches down to 7–8 km depth.

The largest instrumentally observed earthquake on the RP was a $M_S = 6.2$ earthquake that occurred on the 10 km long N–S oriented Hvalhnúkur strike-slip fault in 1929 (Erlendsson & Einarsson 1996). Several historic moderate size earthquakes have occurred on this fault, which is located only 25 km from Reykjavík. On 2000 June 17, three $M \sim 5$ earthquakes were triggered on the RP within a few minutes of a $M_W = 6.6$ earthquake in the SISZ, 80 km east of the RP (Vogfjörd 2003; Antonioli *et al.* 2006). The triggered events occurred on the Hvalhnúkur fault and two other large N–S oriented strike-slip faults near Kleifarvatn and Núpshlíðarháls (Fig. 2) and caused considerable surface deformation (Clifton *et al.* 2003; Pagli *et al.* 2003; Árnadóttir *et al.* 2004). The largest earthquake on the RP within the period of this study was a $M_W = 5.1$ earthquake that occurred on 2003 August 23 and ruptured a N–S oriented strike-slip fault beneath the Sveifluháls hyaloclastite ridge west of Lake Kleifarvatn (Vogfjörd *et al.* 2004, Harvard CMT Catalogue).

The peninsula is almost entirely covered with postglacial lavas with lesser interglacial lavas and hyaloclastites (Sæmundsson & Einarsson 1980). Eruptive activity on the RP is episodic and repeats itself in a cycle on the order of 1000 yr. Each eruptive cycle consists of an eruptive period lasting a few hundred years and a

southwards, causing a gradual deactivation of the WVZ in the direction of EVZ propagation (Einarsson 1991; LaFemina *et al.* 2005).

The main structural features on the RP are five NE trending volcanic fissure swarms, arranged in a right-stepping en-echelon pattern (Jakobsson *et al.* 1978). Most fractures on the RP are extensional tension fractures and normal faults (Fig. 2). The longest fractures are located within the fissure swarms and strike N(20–40)°E, parallel to the eruptive fissures. Most fractures are however oriented

Figure 2. Tectonic map of the Reykjanes Peninsula with locations of fractures from Clifton & Kattenhorn (2006). The fractures are mainly NE oriented tension fractures and normal faults, primarily located within the five volcanic fissure swarms. A series of N–S oriented strike-slip faults are located along an E–W trending zone on the southern part of the peninsula. Four strike-slip faults are labelled: Núpshlíðarháls (N), Sveifluháls (S), Kleifarvatn (K), Hvalhnúkur (H). The stars show epicentres of $M \sim 5$ earthquakes in 1998 June and November (blue), 2000 June (red) and 2003 August (green). Three power plants are labelled: Svartsengi (Sv), Hellisheidi (HH), Nesjavellir (Ne). The box shows the location of the area in Fig. 5.

non-eruptive period lasting several hundred years. The most recent eruption occurred in the 13th century (Thordarson & Larsen 2007). Since then, the only known magmatic event was the inflation of the Hengill–Hrómundartindur volcanic system during 1994–1998. This inflation caused elevated seismicity and uplift of up to 2 cm yr^{-1} (Sigmundsson *et al.* 1997; Feigl *et al.* 2000; Clifton *et al.* 2002), but it ceased in 1998 without an eruption.

Several high-temperature geothermal fields are present on the RP. Energy has been harnessed from the Svartsengi geothermal field on the western RP since 1976, and from the Nesjavellir geothermal field in the Hengill area since 1990 (Fig. 2). Two new power plants have recently been constructed, one on the western tip of the RP, and another at Hellisheidi in the central Hengill area.

3 PREVIOUS GEODETIC WORK

A pioneering geodetic study using precise distance measurements from 1968 to 1972 showed that a combination of left-lateral motion and extension was occurring on the RP (Brander *et al.* 1976). An InSAR study from 1992 to 1995 suggested a subsidence rate of 6.5 mm yr^{-1} along the plate boundary, which was interpreted by the authors to indicate insufficient inflow of magma at depth (Vadon & Sigmundsson 1997). A signal of subsidence around the Svartsengi geothermal power plant was first recorded in 1992 by levelling and gravity observations (Eysteinsson 1993), and was later confirmed by InSAR (Vadon & Sigmundsson 1997) and GPS observations (Hreinsdóttir *et al.* 2001; Magnússon & Thorbergsson 2004).

GPS observations in Iceland started in 1986 with a countrywide campaign (Foulger *et al.* 1987). Sturkell *et al.* (1994) used GPS data at seven campaign stations, surveyed in 1986 and 1992, to estimate a left-lateral shear strain rate of 0.22 ± 0.05 µstrain yr^{-1}, assuming a uniform strain field. Hreinsdóttir *et al.* (2001) modelled the 1993–1998 GPS velocities at 38 stations on the RP, using a 2-D screw dislocation model. They concluded that left-lateral motion of ~16.5 mm yr^{-1} below a locking depth of ~6.5 km was consistent with the horizontal velocity parallel to the strike of the plate boundary at the GPS stations in the central part of the peninsula. Furthermore, they stated that 'little extension was observed across

the peninsula', and suggested that this part of the plate motion was accommodated during discrete episodes of magmatic activity in the fissure swarms. Árnadóttir *et al.* (2006) refined this model, using GPS data from a more extensive network, by approximating the plate boundary in southwest Iceland with a 3-D dislocation and point source model. Their optimal model for the 1992–2000 GPS velocities indicated 18^{+6}_{-5} mm yr^{-1} left-lateral slip and 9 ± 3 mm yr^{-1} opening below 9 ± 3 km, implying extension across the RP. The spreading rate across the WVZ has been estimated from GPS measurements spanning 1994–2003 by LaFemina *et al.* (2005), who found an increase from 2.6 ± 0.9 mm yr^{-1} in the northeast to 7.0 ± 0.4 mm yr^{-1} in the southwest.

4 DATA ACQUISITION AND ANALYSIS

We use GPS data collected on the RP in annual campaigns from 2000 to 2004 (Árnadóttir *et al.* 2006), 2005 and 2006. The 2000 campaign was performed in July, hence our data set spans six years following the 2000 June earthquake sequence. The RP network includes 51 campaign stations that each have been surveyed at least three times during the study period, as well as data from six CGPS stations (Geirsson *et al.* 2006). The campaign stations were normally observed for at least 48 hr, and the data were processed using the Bernese software V4.2 (Hugentobler *et al.* 2001) with orbit information from the Center of Orbit Determination (CODE) in ITRF2000, as described by Geirsson *et al.* (2006). We scale the formal uncertainties to account for systematic errors, so that the uncertainties of individual observations equal the root mean square (rms) from the comparison of repeated baseline lengths. This yields average 1σ uncertainties on individual position estimates of 1–2 mm in the horizontal components and 5–10 mm in the vertical component. The average GPS station velocities are calculated from the GPS time series by linear regression of the annual position estimates (Fig. 3), generated using the GLOBK software (McClusky *et al.* 2000; Herring 2003).
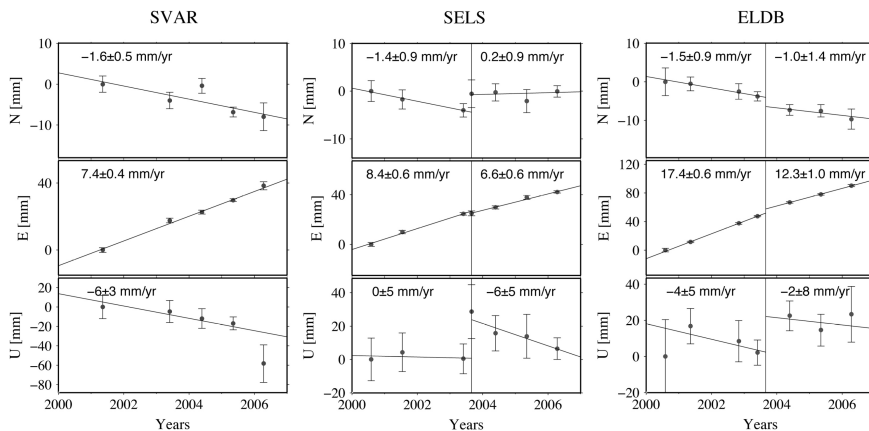

Figure 3. Time series for three GPS campaign stations: SVAR, SELS, and ELDB with North, East, and vertical displacements relative to the reference station REYK. The error bars on station positions are 1σ. The vertical lines show the time of the 2003 August 23 M_W = 5.1 earthquake on the Sveifluháls fault. The station locations are shown in Figs 4 and 5.

4.1 The RP velocity field

We calculate the horizontal velocities relative to the CGPS station in Reykjavík, REYK (Table 1, Fig. 4), as in Hreinsdóttir *et al.* (2001). The principal feature of the horizontal surface velocity field is the change in velocities across the plate boundary. The stations in the northern part of the peninsula move at approximately the same rate and direction as the reference station in Reykjavík, while the velocities increase across the plate boundary towards the southern part of the peninsula. The stations furthest south of the plate boundary move eastwards with velocities of about 15 mm yr^{-1}, relative to REYK. This value constitutes about 80 per cent of the predicted relative North America–Eurasia rate, indicating that the deformation zone is broader than the peninsula. The continuous GPS station VMEY on Heimaey, an island south of Iceland, is moving at almost the full predicted relative NA–EU rate (Árnadóttir *et al.* 2006). A local deformation signal is observed in the area around the Svartsengi geothermal power plant, where the stations move towards the power plant in response to subsidence caused by geothermal fluid extraction (Eysteinsson 1993). Local deformation is also observed at the stations in the Kleifarvatn area due to the 2003 August 23 M_W = 5.1 Sveifluháls earthquake.

The 1993–1998 velocities from Hreinsdóttir *et al.* (2001) are shown in Fig. 4 for comparison. The largest differences are observed on the eastern RP, and are probably due to the 1994–1998 inflation of the Hengill–Hrómundartindur volcanic system. During 1993–1998, several of the stations on the eastern RP show significantly less eastward motion, the station KAFF located close to the centre of inflation even has westward velocity, and the station TVEG at the southeastern RP shows a large southward component. Further differences between the two periods are observed along the southern shore of the peninsula, where several stations show a velocity increase on the order of 2–4 mm yr^{-1} from 1993–1998 to 2000–2006. The observed velocity increase should not necessarily be interpreted as an increase at these particular stations, but rather as an increase in the relative plate motion across the peninsula. However, the signal is small and the total plate motion is not well constrained because the peninsula is narrower than the plate boundary zone. All of these observed velocity variations are consistent with the results of Árnadóttir *et al.* (2006), from their analysis of GPS data in SW Iceland spanning 1992–2004, using GAMIT/Globk.

The vertical velocities show a pronounced signal of subsidence around the Svartsengi power plant, in agreement with previous studies (e.g. Vadon & Sigmundsson 1997; Hreinsdóttir *et al.* 2001), but we do not observe the signal of subsidence along the plate boundary, suggested by Vadon & Sigmundsson (1997). The detail of the vertical GPS deformation field is difficult to resolve due to small signal to noise ratio (Table 1). The vertical velocities are included in our modelling but will not be described in detail here.

4.2 Correction for the Sveifluháls 2003 earthquake

The Sveifluháls earthquake occurred on 2003 August 23, and ruptured a N–S oriented fault with right-lateral strike-slip motion below the Sveifluháls hyaloclastite ridge. The M_W = 5.1 main shock occurred at 4 km depth and was followed by a swarm of more than 1200 aftershocks at 1.5–5 km depth. Half of the aftershocks occurred on the main Sveifluháls fault, while the other half occurred on a series of intervening short fault segments extending 3 km towards NE from the middle of the Sveifluháls fault (Vogfjörd *et al.* 2004). Coseismic displacements of up to 11 mm in the horizontal components were observed on nearby GPS stations (Table 2, Figs 3 and 5).

Table 1. GPS station velocities 2000–2006, relative to REYK.

Site	Latitude (°N)	Longitude (°W)	East	North	Vertical
ALMA	64.26	21.13	0.8 ± 0.2	0.6 ± 0.4	4 ± 1
ARSE	63.91	22.42	4.4 ± 0.3	−3.2 ± 0.4	−6 ± 2
ARST	63.88	22.53	9.8 ± 0.4	−2.7 ± 0.5	−7 ± 2
ASFJ	64.05	21.94	0.9 ± 0.5	0.6 ± 0.7	1 ± 4
AUDS	63.95	21.15	12.8 ± 0.3	−1.2 ± 0.5	3 ± 3
BLAF	63.99	21.65	6.0 ± 0.2	−0.9 ± 0.3	1 ± 1
BREN	63.95	21.77	8.1 ± 0.3	−1.4 ± 0.5	4 ± 2
BURG	64.05	21.86	1.9 ± 0.3	−0.6 ± 0.5	6 ± 2
DRAU	64.05	21.41	5.9 ± 0.2	−0.7 ± 0.3	−1 ± 1
ELDB*	63.85	21.99	16.5 ± 0.3	−1.9 ± 0.4	2 ± 2
GARD	64.07	22.69	0.9 ± 0.3	−0.9 ± 0.5	3 ± 2
GEIT	63.95	21.53	9.7 ± 0.2	−0.9 ± 0.3	5 ± 1
GLJU	63.99	21.14	8.3 ± 0.5	−0.7 ± 0.7	6 ± 3
GRHO	63.97	22.43	3.0 ± 0.4	−1.6 ± 0.6	−2 ± 3
GRIN	63.99	21.78	4.9 ± 0.3	−1.7 ± 0.4	4 ± 2
HAFN	63.93	22.68	3.4 ± 0.3	−1.7 ± 0.4	−1 ± 2
HERD	63.87	21.84	14.3 ± 0.3	−1.1 ± 0.4	6 ± 2
HH04	64.02	21.32	5.7 ± 0.2	1.4 ± 0.3	2 ± 1
HLBV	64.03	22.56	2.6 ± 0.3	−1.5 ± 0.5	−1 ± 2
HLID	63.92	21.39	12.8 ± 0.1	−0.5 ± 0.2	3 ± 0
HOLM	64.09	21.70	1.5 ± 0.3	−0.3 ± 0.4	1 ± 2
HOSK*	63.95	22.11	3.4 ± 0.3	0.1 ± 0.4	3 ± 2
HVER	64.02	21.18	6.2 ± 0.1	0.5 ± 0.1	0 ± 0
KAFF	64.06	21.48	4.4 ± 0.2	−0.7 ± 0.3	7 ± 1
KAMB	64.00	21.25	8.4 ± 0.3	−0.2 ± 0.4	3 ± 2
KAST	63.88	22.32	7.2 ± 0.3	−0.4 ± 0.4	−2 ± 2
KINN	63.87	22.68	6.6 ± 0.3	−2.1 ± 0.4	−2 ± 2
KLAM	64.05	21.23	3.0 ± 0.2	0.0 ± 0.3	3 ± 2
KLEI*	63.94	21.95	6.2 ± 0.4	−0.5 ± 0.7	−2 ± 3
KLOF*	63.96	21.97	3.8 ± 0.2	−0.6 ± 0.3	3 ± 1
KOGU	63.96	21.08	12.6 ± 0.3	−1.6 ± 0.4	9 ± 2
KRIS*	63.87	22.09	13.8 ± 0.3	−1.1 ± 0.5	7 ± 3
KUAG	64.00	22.23	1.1 ± 0.3	−0.6 ± 0.4	4 ± 2
LAMB*	63.91	22.01	10.3 ± 0.2	−1.0 ± 0.3	3 ± 2
LJOS	64.09	21.02	6.5 ± 0.4	0.4 ± 0.4	4 ± 3
MOHA*	63.92	22.06	4.2 ± 0.3	−2.4 ± 0.5	5 ± 2
MOLD	64.05	21.24	4.2 ± 0.3	0.1 ± 0.5	0 ± 2
NAUF	63.92	22.29	2.5 ± 0.3	−1.5 ± 0.4	4 ± 2
NV16	64.13	21.19	−1.0 ± 1.0	−1.5 ± 1.5	2 ± 8
OLKE	64.06	21.22	3.1 ± 0.1	−0.6 ± 0.1	1 ± 0
REYK	64.14	21.96	0.0 ± 0.4	0.0 ± 0.4	0 ± 0
RNES	63.83	22.65	9.5 ± 0.3	−0.1 ± 0.4	−3 ± 2
SAND	64.09	21.26	0.4 ± 0.3	0.6 ± 0.5	6 ± 2
SEHE	63.87	21.56	13.0 ± 1.0	−1.9 ± 1.5	−2 ± 8
SELA	63.85	22.23	13.3 ± 0.2	0.2 ± 0.3	0 ± 1
SELF	63.93	21.03	12.0 ± 0.2	−1.4 ± 0.2	5 ± 1
SELS*	63.90	22.15	7.1 ± 0.2	0.3 ± 0.4	1 ± 1
STAD	63.82	22.52	11.7 ± 0.3	2.9 ± 0.4	−1 ± 2
STGR	64.03	22.11	2.1 ± 0.2	−0.7 ± 0.3	−4 ± 2
SVAR	63.88	22.42	7.4 ± 0.4	−1.6 ± 0.5	−6 ± 3
SVIN	64.05	21.27	3.7 ± 0.4	−0.7 ± 0.6	1 ± 3
THRE	63.99	21.46	8.1 ± 0.3	−0.5 ± 0.4	0 ± 2
TJAL	63.85	22.63	8.4 ± 0.3	−1.5 ± 0.4	0 ± 2
TVEG	63.91	21.37	13.6 ± 0.3	−0.1 ± 0.4	7 ± 2
URDA	63.93	22.56	4.7 ± 0.3	−1.7 ± 0.4	−2 ± 2
VOGA	63.97	22.34	1.8 ± 0.3	−1.7 ± 0.5	−1 ± 2
VOGS	63.85	21.70	15.2 ± 0.1	−1.1 ± 0.1	2 ± 0

Uncertainties are 1σ. The star (*) denotes stations with a coseismic offset caused by the 2003 August 23 M_W = 5.1 Sveifluháls earthquake.
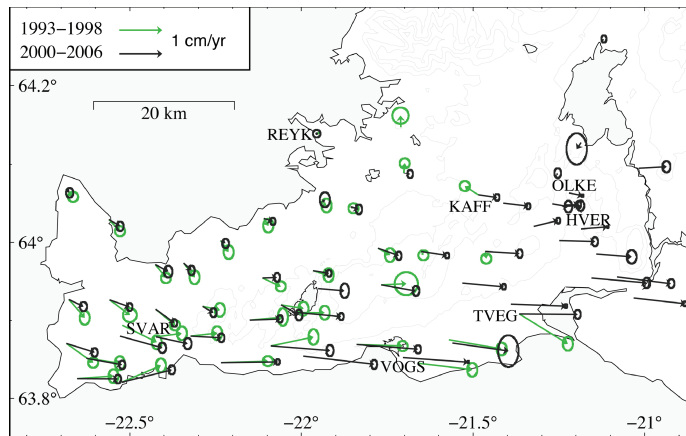
Figure 4. Horizontal GPS velocities for 2000–2006 (black) and 1993–1998 (green, from Hreinsdóttir *et al.* 2001). The velocities are shown relative to the reference station REYK, with 2σ confidence ellipses. Three campaign station (SVAR, KAFF, TVEG) and four continuous GPS stations (REYK, VOGS, OLKE, HVER) are labelled.

Table 2. Estimated coseismic displacements and corrected 2000–2006 velocities at eight stations affected by the 2003 August 23 $M_W = 5.1$ Sveifluháls earthquake.

Site	Latitude (°N)	Longitude (°W)	Coseismic displacements (mm)			Corrected velocities (mm yr^{-1})		
			East	North	Vertical	East	North	Vertical
ELDB	63.85	21.99	5.8 ± 1.5	-2.4 ± 2.1	22 ± 12	15.0 ± 0.5	-1.2 ± 0.8	-3 ± 4
HOSK	63.95	22.11	-4.6 ± 1.6	10.4 ± 2.5	-4 ± 14	3.9 ± 0.6	-1.8 ± 0.8	2 ± 4
KLEI	63.94	21.95	-4.2 ± 1.4	3.0 ± 2.5	2 ± 13	7.1 ± 0.8	-0.9 ± 1.3	-3 ± 6
KLOF	63.96	21.97	-2.8 ± 1.2	0.5 ± 2.0	8 ± 11	4.8 ± 0.4	-1.3 ± 0.7	0 ± 3
KRIS	63.87	22.09	5.0 ± 1.9	-1.4 ± 2.7	2 ± 16	12.6 ± 0.8	-0.9 ± 1.1	4 ± 6
LAMB	63.91	22.01	1.3 ± 2.1	-6.4 ± 3.3	-13 ± 19	10.8 ± 0.4	0.2 ± 0.7	2 ± 3
MOHA	63.92	22.06	-8.0 ± 1.7	-3.1 ± 2.7	4 ± 15	6.9 ± 0.6	-1.3 ± 1.0	1 ± 5
SELS	63.90	22.15	-1.7 ± 2.2	3.8 ± 3.2	28 ± 18	7.6 ± 0.4	-0.6 ± 0.6	-3 ± 3

The coseismic displacements are estimated as the offsets in the station positions that are observed when the pre- and post seismic velocities are extrapolated to the time of the earthquake. The uncertainties (1σ) are propagated using the uncertainties on pre- and post-quake station positions and the extrapolated velocities.

The coseismic displacements are estimated as the offsets in the station positions that are observed when the pre- and post-seismic velocities are extrapolated to the time of the earthquake. Two of the stations, SELS and LAMB (see Fig. 5), were surveyed a few days after the earthquake on 2003 August 23, while the other six stations were surveyed during the annual campaigns in 2003 May and 2004 May.

We estimate the long-term interseismic velocity field after correcting the 2000–2006 time-series for coseismic offsets due to the 2003 August earthquake at eight stations in the Kleifarvatn area. The corrected velocities are then used for our kinematic modelling of the plate boundary deformation in the following section.

5 MODELLING

In the following sections we derive source models to match the observed surface deformation on the RP. First, we invert the estimated coseismic displacements at eight stations in the Kleifarvatn area for the source parameters of the $M_W = 5.1$ Sveifluháls 2003 earthquake. We then present a kinematic model of the long-term plate boundary deformation. Finally, we estimate the continuous strain rate field for

two different time periods: 1993–1998 and 2000–2006, using GPS velocities published by Hreinsdóttir *et al.* (2001) and results from this study.

5.1 Modelling approach

We model the observed deformation on the RP using vertical dislocations (Okada 1985) and a point source (Mogi 1958), in isotropic and homogeneous elastic half-space with a Poisson's ratio of 0.25. We approximate the plate boundary as a series of vertical dislocations and a local area of subsidence as a point source, whereas in the earthquake case, we assume a single planar dislocation. We apply an inversion approach to find the set of model parameters that minimizes the weighted residual sum of squares, WRSS $= \mathbf{r}^T \sum^{-1} \mathbf{r}$, where $\mathbf{r}$ is the difference between the observed and predicted displacements or velocities, and $\sum$ is the data covariance matrix. In general, the surface deformation is a non-linear function of the model geometry and source location. We therefore, obtain the optimal model parameters with a non-linear optimization scheme, that uses a simulated annealing algorithm, followed by a derivative-based method, as described by Cervelli *et al.* (2001). The simulated
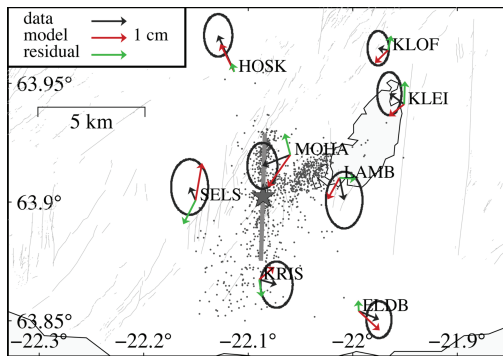
Figure 5. Horizontal coseismic displacements at eight GPS stations in the Kleifarvatn area due to a $M_W = 5.1$ earthquake on the Sveifluháls fault on 2003 August 23. The arrows show observed coseismic displacements (black, 2σ confidence ellipses), predicted surface displacements (red), and residuals (green). The estimated location of the Sveifluháls fault from the dislocation modelling is shown with the thick grey line. The grey star shows the main shock epicentre and the dots show the more than 1200 aftershocks that occurred on August 23–24 (Vogfjörd *et al.* 2004).

annealing performs a random search through the model parameter space and finds the valley containing the global minimum in the multidimensional misfit space, while the randomness permits it to escape local minima. The result from the simulated annealing is then passed to the derivative-based algorithm, which finds the bottom of the misfit valley. The mean and confidence intervals of the model parameters are estimated using a bootstrap algorithm (Efron & Tibshirani 1986), that resamples the data set randomly a large number of times (here we use 1000 times). We resample each station using all three components, that is, the east, north and vertical, while allowing the same station to be resampled more than once or not at all. The optimal model parameters are then estimated for each resampled data set, and the 95 per cent confidence limits are found by discarding the top and bottom 2.5 per cent of the sorted bootstrap parameters. The bootstrap algorithm provides a reasonable measure of the confidence intervals and gives important information on correlations between the model parameters. We report the level of fit to the data using the reduced chi-squared, calculated as $\chi_\nu{}^2 = \frac{WRSS}{N-m}$, where N is the number of data and m is the number of unknown model parameters.

5.2 The Sveifluháls 2003 earthquake

The Sveifluháls earthquake is modelled as a rectangular dislocation with uniform slip, using the bootstrap inversion scheme described in Section 5.1 and minimizing the WRSS, where **r** is the difference between the observed and predicted coseismic displacements. We estimate seven parameters for the location and the geometry of the fault plane as well as the amount of right-lateral strike-slip, which gives $m = 8$ unknown model parameters for $N = 24$ data. The optimal model has $\chi_\nu{}^2 = 2.8$. The estimated fault plane has a length of 6 ± 1 km and a width of 4 ± 2 km below 1^{+3}_{-1} km depth (2σ uncertainties). The slip is 13^{+34}_{-8} cm, assuming uniform right-lateral slip over the entire area of the fault plane. The fault strikes $N(2^{+3}_{-7})°E$ and dips 78^{+11}_{-8} degrees towards west. The estimated displacements generally have a small signal to noise ratio (Fig. 5, Table 2), hence the bounds on the parameters are large. The geodetic moment is

9.5×10^{16} N m, calculated as $M_0 = \mu Au$, where μ is the shear modulus (here we use $\mu = 30$ GPa), A is the area of the fault plane, and u is the slip. The geodetic moment corresponds to a $M_W = 5.3 \pm 0.6$ earthquake (using the formula $M_W = \frac{2}{3} \cdot \log M_0 - 6.03$), close to the estimate of $M_W = 5.1$ from the Harvard CMT Catalogue. The small discrepancy between the magnitude estimates is probably due to our uniform slip assumption.

5.3 Kinematic plate boundary models

We approximate the plate boundary with a series of vertical dislocations parallel to the trend of the plate boundary (Fig. 6). We use the model geometry suggested by Árnadóttir *et al.* (2006) for their modelling of the plate boundary deformation in SW Iceland from 1992 to 2000. The RP plate boundary is represented by two dislocations due to a bend in the plate boundary on the western part of the peninsula. The central RP dislocation strikes N79°E and the RPW dislocation strikes N68°E. In addition to these, the model has dislocations for each of the SISZ and the WVZ, and a point source for the subsidence at Svartsengi.

The non-linear optimization and estimation of the bounds on model parameters are done applying the bootstrap methodology described in Section 5.1, minimizing the WRSS, where **r** is now the difference between the observed and predicted surface velocities. We estimate the depth to the upper edge of the four dislocations, representing the locking depths, below which the dislocations are assumed to slip freely. We allow both left-lateral slip and opening along the RP and RPW, left-lateral motion along the SISZ, and opening across the WVZ. In addition to the dislocation parameters, we estimate the location, depth and volume change of the Svartsengi point source. This yields a total of $m = 14$ unknown model parameters for $N = 171$ data. We fix 30 model parameters *a priori*, mainly the parameters related to the geometry of the plate boundary.

The estimated model parameters are given in Table 3, together with the 1992–2000 parameters from Árnadóttir *et al.* (2006). In Table 3, we also state the resulting 'deep motion' and 'azimuth', which are calculated as the magnitude and direction of the vector sum of the left-lateral slip rate and the opening rate. For the RP we estimate left-lateral motion 18^{+4}_{-3} mm yr^{-1} and opening of 7^{+3}_{-2} mm yr^{-1} below a locking depth of 7^{+1}_{-2} km. The resulting deep motion of 20^{+4}_{-3} mm yr^{-1} in the direction of N$(100^{+8}_{-6})°$E agrees well with the predicted relative North America–Eurasia rate. The model has a reduced chi-squared $\chi_\nu{}^2 = 4.6$, and residuals are generally large on the western RP and in the Hengill area (see Fig. 6). Our model predicts a considerable component of opening, that is, about one fourth of the total motion, in agreement with the 1992–2000 parameters from Árnadóttir *et al.* (2006). We also test a model with no opening across the RP and RPW, but find that this model has a considerably worse fit to the data ($\chi_\nu{}^2 = 6.5$).

We consider several other models to investigate if we can fit the data better by including additional sources of deformation. We use the statistical *F*-test to determine whether the improvement in the fit to the data resulting from the addition of more source parameters is significant on a 99 per cent confidence level (e.g. Stein & Gordon 1984). One such model has right-lateral slip on an additional NS-oriented dislocation on the central RP, to examine if there could be afterslip following the 2000 June earthquakes in the Kleifarvatn area. This model predicts left-lateral slip rather than the expected right-lateral slip, and it does not improve the fit to the data according to the *F*-test. Another model we test has opening across a NE-oriented dislocation, to examine if we can detect any
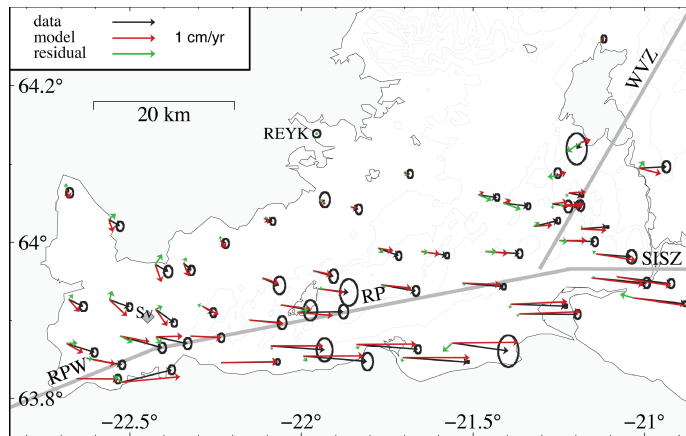
Figure 6. Results of kinematic plate boundary modelling of the 2000–2006 velocities, corrected for coseismic offsets due to a $M_W = 5.1$ earthquake on the Sveifluháls fault on 2003 August 23. The velocity arrows show observed (black, 2σ confidence ellipses), predicted (red), and residual velocities (green). The dislocations are shown with thick gray lines and labelled: Reykjanes Peninsula West (RPW), Reykjanes Peninsula (RP), South Iceland Seismic Zone (SISZ), Western Volcanic Zone (WVZ) and the Svartsengi (Sv) point source is shown with a grey diamond.

Table 3. Estimated dislocation parameters for kinematic plate boundary models.

	Depth (km)	Left-lateral (mm yr^{-1})	Opening (mm yr^{-1})	Deep motion (mm yr^{-1})	Azimuth (N°E)
Simplest plate boundary model, $\chi_\nu^2 = 4.6$					
RP	7^{+1}_{-2}	18^{+4}_{-3}	7^{+3}_{-2}	20^{+4}_{-3}	100^{+8}_{-6}
RPW	4 ± 2	29 ± 5	5^{+6}_{-8}	30^{+5}_{-6}	78^{+12}_{-16}
SISZ	6 ± 3	22^{+4}_{-5}	–	–	–
WVZ	3^{+3}_{-1}	–	11^{+4}_{-3}	–	–
Fissure swarm model, $\chi_\nu^2 = 3.4$					
RP	8^{+2}_{-3}	18^{+3}_{-4}	3^{+6}_{-4}	19^{+3}_{-5}	87^{+20}_{-11}
FISSURE	2^{+5}_{-2}	–	6^{+7}_{-4}	–	–
RPW	6 ± 3	24^{+6}_{-4}	-2^{+6}_{-9}	24^{+6}_{-4}	62^{+14}_{-19}
SISZ	6 ± 3	22 ± 4	–	–	–
WVZ	3^{+4}_{-3}	–	6 ± 3	–	–
Plate boundary model for 1992–2000 GPS velocities[a]					
RP	9 ± 3	18^{+6}_{-5}	9 ± 3	20^{+6}_{-5}	106^{+11}_{-9}
RPW	6^{+2}_{-1}	36^{+2}_{-3}	–	–	–
SISZ	15^{+8}_{-10}	19^{+10}_{-9}	–	–	–
WVZ	5^*	–	7^*	–	–

Notes: The mean and 2σ confidence limits of the model parameters are estimated from 1000 resampled data sets, using the bootstrap method described in Section 5.1. Fixed model parameters are marked with *. The 'deep motion' and the 'azimuth' are the magnitude and direction of the vector sum of the left-lateral deep slip and opening.
[a]Model parameters from Árnadóttir *et al.* (2006, their table 3).

extension across the fissure swarm at the central RP. This model has a $\chi_\nu^2 = 3.4$, which is a statistically significant improvement of the fit. The NE-oriented dislocation has an estimated opening rate of 6^{+7}_{-4} mm yr^{-1} below a locking depth of 2^{+5}_{-2} km (see Table 3), while the RP dislocation has a similar left-lateral rate of 18^{+3}_{-4} mm yr^{-1},

but a lower opening rate of 3^{+6}_{-4} mm yr^{-1} below 8^{+2}_{-3} km depth. The results of this model indicates that there may be a partitioning of the oblique plate motion in the upper crust, so that the left-lateral shear is mainly taken up by the seismically active NS-oriented strike-slip faults that lie along an E–W trending zone on the southern part of the peninsula, while the opening is mainly accommodated within the fissure swarms (see Fig. 2). Our kinematic model is, however, non-unique due to the limitations of the data and the complexity of the region, and more advanced modelling is needed to resolve the details of the deformation field. In the following discussion, we therefore, choose to refer to the simplest possible model.

The deformation on the RPW is complicated due to the change in strike of the plate boundary and the local deformation around the Svartsengi geothermal power plant. The Svartsengi point source has an estimated volume decrease of $(0.6^{+0.4}_{-0.5}) \times 10^6$ m^3 yr^{-1} at a depth of 5^{+5}_{-4} km. The uncertainties on these estimates are generally large, and there is considerable trade-off between the depth and the estimated volume change of the point source. All the models that we and Árnadóttir *et al.* (2006) tested yield higher left-lateral slip rates and lower opening rates on the RPW than on the RP. This behaviour is opposite to what we expect, because the change in the strike of the plate boundary should rather induce a larger component of opening. It therefore, seems likely that our kinematic models do not fully explain the complicated deformation observed in this area. The shallower depth to the RPW dislocation, compared to the RP dislocation, is consistent with thinning of the brittle crust from east to west, but the decrease probably occurs more gradually along the length of the peninsula than is allowed by our simple model.

5.4 Strain field

We estimate the strain rate field from the 1993–1998 velocities (Hreinsdóttir *et al.* 2001) and the 2000–2006 velocities, using the method by Haines *et al.* (1998) and Beavan & Haines (2001). The strain calculation is done in two steps. First, an interpolated velocity field is calculated on a rectangular 6×6 km grid by bicubic spline interpolation of the observed GPS velocities. Second, the average

principal strain rates at the centre of each grid cell are calculated as the derivative of the velocities, and the strain solution is then interpolated onto a finer mesh.

We present the results in terms of the areal strain rates [$\frac{1}{2}(\dot{\epsilon}_{xx} + \dot{\epsilon}_{yy})$], and shear strain rates ($\dot{\epsilon}_{xy}$), where x is E–W and y is N–S. Positive areal strain rates indicate expansion and negative strain rates indicate contraction. The areal strain rate fields for 1993–1998 and 2000–2006 are shown in Figs 7(a) and (e). A principal feature of the areal strain rate fields is the marked zone of contraction around the Svartsengi power plant, which is observed for both periods although the signal is stronger during 1993–1998. Small zones of expansion are observed at about 15 km distance from the power plant, especially at its western side. An elongated zone of marked expansion is observed on the eastern RP during 1993–1998, and a circular zone of contraction is observed in the Hengill area during 2000–2006.

The shear strain rates in Figs 7(b) and (f) are primarily negative, consistent with left-lateral shear on E–W structures or right-lateral shear on N–S structures. The plate boundary on the central and eastern RP is generally characterized by negative shear strain rates, but large variations are observed. The largest shear strain rates are observed on the eastern RP during 1993–1998 and on the central RP during 2000–2006. The Hengill area and the transition towards the SISZ also show high shear strain rates during 2000–2006. The area around Svartsengi shows a consistent pattern of high negative shear strain rates in the NW and SE quadrants and lower shear strain rates in NE and SW quadrants, at distances of about 15 km from the centre of contraction.

The strain rates mapped by this study show considerable spatial and temporal variation within the plate boundary zone. In order to examine how well the kinematic models capture the subtle velocity variations, we calculate strain rates from the predicted velocities at the GPS station locations using the estimated model parameters from Árnadóttir *et al.* (2006) for the 1993–1998 time period (Figs 7c and d), and the estimated model parameters from this study (Table 3, the simplest plate boundary model) for the 2000–2006 period (Figs 7g and h). The sources of deformation are the left-lateral transform motion and opening of the plate boundary segments, the inflation of the Hengill–Hrómundartindur volcanic system during 1994–1998, and the subsidence around the Svartsengi geothermal power plant. The strain rate maps will be discussed in more detail below.

The resolution of the location and magnitude of the estimated strain rate signals depends on the spatial and temporal density of the geodetic data. The station density increased somewhat from 1993–1998 to 2000–2006, hence the spatial resolution is generally better in the latter data set. In particular, the observed signals of areal expansion and high shear strain rates on the eastern RP during 1993–1998 (Figs 7a and b) are uncertain because the signal is due to large velocity differences between a few stations. We have compared the predicted strain rates in Fig. 7 to strain rates calculated from the same models, but using a rectangular grid instead of the GPS station locations, in order to investigate how the estimated strain rate signals are affected by station geometry. We found that the strong signal of areal expansion west of Svartsengi is a product of the Svartsengi point source and the network geometry, but that the other modelled strain rate signals are not significantly biased by the station locations.

6 DISCUSSION

6.1 Local velocity changes in the Kleifarvatn area

Many of the stations in the Kleifarvatn area show a small velocity increase between the 1993–1998 and 2000–2006 time periods (Fig. 4).

Furthermore, some stations show velocity decreases again in year 2003 (see Fig. 3), although the decrease is usually only significant at the 1σ level. Hence, the GPS data seem to show subtle velocity variations that may be related to stress changes following the moderate earthquakes in 2000 June and 2003 August. The triggered earthquakes on 2000 June 17 caused considerable surface deformation, particularly around the Kleifarvatn fault (Pagli *et al.* 2003), and a coseismic offset of several cm was observed at the CGPS station VOGS (Geirsson *et al.* 2006). Static coseismic Coulomb failure stress calculations indicate that the 2000 June 17 Núpshlíðarháls event increased the Coulomb failure stress at the 2003 August 23 hypocentre Árnadóttir *et al.* (2004). However, the short interseismic time series in this area makes the velocity estimates uncertain, and great care has to be taken when interpreting these subtle velocity variations.

6.2 Regional plate boundary deformation

Our kinematic model of the surface deformation field provides an estimate of the far-field plate motion, represented by deep aseismic slip below the brittle crust. The brittle crust on the RP deforms in a highly complicated system of fractures, but it appears to be driven by an E–W oriented aseismic shear zone at depth (e.g. Einarsson 1991). In our model, the deep aseismic slip is approximated by a series of vertical dislocations aligned along the trend of the plate boundary, allowing opening to account for the extension across the plate boundary.

Hreinsdóttir *et al.* (2001) modelled the 1993–1998 GPS velocities using a screw dislocation model to represent left-lateral transform motion along the RP. The simple screw dislocation model does not include a component of opening to account for oblique plate motion, nor does it allow one to model the effect of local sources of inflation or subsidence. The authors suggested that the apparent discrepancy between the observed motion and the predicted oblique plate motion may be explained by the lack of magma intrusion into the crust, and that extension perpendicular to the eruptive fissures primarily occurs during magmatic periods. Their conclusion was based on observations from the Krafla volcanic system in the Northern Volcanic Zone, where rifting events are clearly episodic and are triggered by magma injection into the crust (Einarsson 1991; Buck *et al.* 2006). Our kinematic model indicates that the current plate motion on the RP involves a significant component of opening across the plate boundary. We therefore argue that the observed surface deformation is consistent with the continuous oblique plate motion induced by the far field stresses.

The observed opening across the RP plate boundary does not, however, preclude that the plate motion is affected by temporal variations in magmatic activity on a longer time scale. The magmatism on the RP is episodic like most other mid-oceanic plate boundaries, and we would expect the episodic inflow of magma at shallow depth to perturb the stress field and cause additional extension perpendicular to the fissure swarms. The close spatial relationship of the fractures and the volcanic systems on the RP furthermore indicates that magmatism has had an important influence on the development of the surface fractures (Clifton & Kattenhorn 2006).

Our geodetic evidence for the oblique motion is in general agreement with structural analysis of the fracture pattern on the RP. Analogue clay model experiments show that highly complex fracture patterns develop in oblique plate boundary zones, and similarities to the observed fracture pattern on the RP has been described by Clifton & Schlische (2003). They conclude that discrepancies
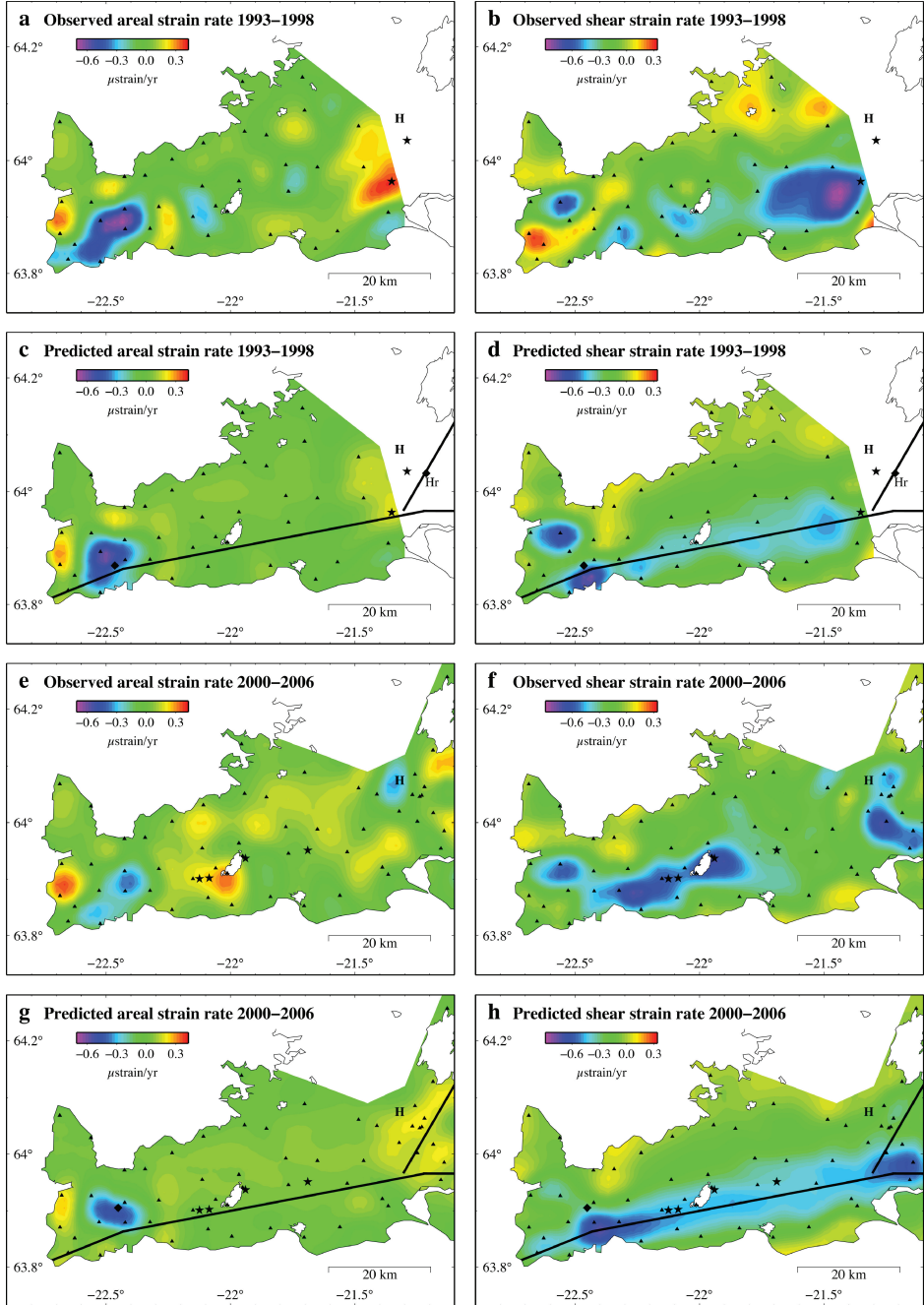
Figure 7. Observed and predicted areal ($\frac{1}{2}(\dot{\epsilon}_{xx} + \dot{\epsilon}_{yy})$) and shear ($\dot{\epsilon}_{xy}$) strain rates for 1993–1998 and 2000–2006. The black triangles show the locations of the GPS stations that were surveyed during each period. The predicted strain rates are obtained from kinematic modelling of the velocity fields. The dislocations are shown with black lines and the Svartsengi and Hrómundartindur (Hr) point sources with black diamonds. The central Hengill volcano is marked (H). The stars show epicentres of $M \sim 5$ earthquakes in 1998, 2000 and 2003 (see Fig. 2).

between the clay model analogue and the observed fracture pattern on the RP are mainly observed within the fissure swarms and are ascribed in general to magmatic activity.

Better constraint on the vertical deformation is required in order to determine whether there is currently sufficient inflow of magma at depth to make up for the component of opening perpendicular to the plate boundary. There is no clear evidence from our campaign GPS data for subsidence along the plate boundary, but these data are hampered by large uncertainties. Analysis of new InSAR data on the RP will presumably help resolve this important question in future.

6.3 Strain rate variations

The plate boundary on the RP is generally characterized by negative shear strain rates, but we observe considerable variation in the intensity and distribution of the observed shear strain rates, as well as local anomalies in the areal strain rates. Our kinematic model predicts a continuous zone of negative shear due to the left-lateral slip along the plate boundary and local perturbations of the strain rate fields around the Svartsengi point source, but it does not reproduce all the observed variation. In the following sections we discuss the perturbations of the regional strain rate fields caused by shallow sources.

6.3.1 The eastern Reykjanes Peninsula and the Hengill area

The 1993–1998 strain rate maps show pronounced signals of areal expansion and shear on the eastern RP (Figs 7a and b). These strain anomalies are probably related to the 1994–1998 inflation and elevated seismicity in the Hengill–Hrómundartindur volcanic system. The inflation was observed by synthetic aperture radar (SAR) interferometry, which show concentric fringes of uplift near the Hrómundartindur volcanic centre in the Hengill area (Feigl *et al.* 2000). The authors used point source modelling of the SAR images to show that the observed uplift could be explained by an inflating magma chamber at 7 km depth. The primary effect of the expanding Hrómundartindur point source is increased areal strain rates, but the point source also induces horizontal shear that perturbs the strain rate field, as demonstrated by Sigmundsson *et al.* (1997). Near the surface, the left-lateral shear strain is enhanced NE and SW of the point source, in quadrants around the direction of maximum regional horizontal strain, and diminished NW and SE of the point source, in quadrants around the direction of minimum regional strain. The centre of inflation is located outside the 1993–1998 GPS network, hence the predicted effects on the eastern RP strain field are small (Figs 7c and d), although the estimated volume change of the point source is large. The general pattern of the observed strain rates on the eastern part of the 1993–1998 network (Figs 7a and b) is consistent with the prediction from the model, although the observed signals are much larger, with a clear elongated zone of areal expansion and a zone of pronounced shear strain on the eastern RP. As stated above, these strain anomalies are due to large velocity differences between a few stations, hence the estimated magnitudes and locations of the signals depend somewhat on the station distribution. However, the discrepancy between the predicted and observed strain rate magnitudes indicates that the Mogi source model from Feigl *et al.* (2000) may not capture the whole deformation signal observed during the inflation of the Hengill–Hrómundartindur volcanic system. A possible explanation for this discrepancy may be that some widening occurred across the Hengill fissure swarm dur-

ing the 1994–1998 inflation, although there is no clear evidence for shallow magma injection in the area.

Elevated seismicity was observed in the Hengill area during 1994–1998. The earthquakes mainly occurred in swarms, but two $M \sim 5$ main shock–aftershock sequences also struck the area in 1998 June and November (Vogfjörd *et al.* 2005). The 1998 November sequence occurred in the area where we observe the shear strain anomaly during 1993–1998 (Fig. 7b), and micro-earthquake activity leading up to the earthquake sequence indicated that the fractures were already close to failure. The 1998 GPS campaign was performed in June and August, hence the 1993–1998 displacements are not affected by the 1998 November sequence, but a signal induced by the 1998 June sequence cannot be excluded.

During 2000–2006, the eastern RP is characterized by very low shear strain rates (Fig. 7f), but we observe considerable shear strain again in the Hengill area. The area of low shear strain corresponds closely to the area of the shear strain anomaly during 1993–1998, indicating that the eastern RP may be in a stress shadow following the 1994–1998 inflation and elevated seismicity in the Hengill–Hrómundartindur volcanic system.

We observe a contraction signal in the central Hengill area during 2000–2006 (Fig. 7e). The contraction is observed ca. 8 km west of the centre of the 1994–1998 inflation and thus cannot be related to a subsequent deflation of this volcanic system. The signal of contraction suggests subsidence of the central part of the Hengill area, which is supported by the fact that the two CGPS stations in the area (OLKE and HVER, see Fig. 4) have been subsiding relative to REYK since 2002. Extensive geothermal production takes place at the Nesjavellir power plant in the northern part of the Hengill area, and prospecting drilling has been performed at Hellisheidi (see Fig. 2) during the period under study. The observed contraction may, therefore, be related to subsidence or local faulting caused by geothermal fluid extraction.

6.3.2 Svartsengi geothermal power plant

We observe strong signals of areal contraction and perturbed shear strain rates around the Svartsengi power plant. The clear decrease in the magnitude of the strain rates from 1993–1998 to 2000–2006 is related to a decrease in the rate of subsidence between the two periods. This observation is supported by vertical GPS velocities from repeated surveys of a dense network around Svartsengi (Magnússon & Thorbergsson 2004). The subsidence at Svartsengi varies approximately linearly with observed pressure decrease in the geothermal reservoir, indicating that the subsidence is mainly due to compaction of pore space in the rock matrix (Eysteinsson 2000).

During both periods the zone of contraction around Svartsengi is elongated in the NE–SW direction (Figs 7a and e), hence a single point source is not sufficient to explain the observed deformation. The zone of contraction extends parallel to the strike of the tension fractures and normal faults and includes another not yet utilized geothermal field, Eldvörp, located five km southwest of Svartsengi. Geodetic observations and bore hole measurements suggest that there is a pressure link between Svartsengi and Eldvörp (Eysteinsson 2000), which could explain the elongation of the observed contraction signal.

6.3.3 The central Reykjanes Peninsula

During 2000–2006, a continuous zone of pronounced shear is observed from Svartsengi to the area east of Kleifarvatn (Fig. 7f).

This shear strain signal is not reproduced by the kinematic model (Fig. 7h). The areal strain rates in the Kleifarvatn area also show variations that are not reproduced by the model. A small signal of contraction is observed west of Lake Kleifarvatn during 1993–1998 (Fig. 7a), while expansion is observed in the same area during 2000–2006 (Fig. 7e). The estimated strain rates on the central RP do not include coseismic deformation, although some bias may be caused by the correction for the coseismic offset at the Sveifluháls 2003 earthquake. However, the area between Svartsengi and Kleifarvatn has been characterized by elevated background seismicity since the late 1990s, hence the shear strain and areal strain anomalies may be related to earthquake activity. Both the 2000 June 17 Núpshlíðarháls and Kleifarvatn earthquakes as well as the Sveifluháls 2003 earthquake occurred in the area where we observe pronounced shear strain rates during 2000–2006.

7 CONCLUSIONS

We find that the surface deformation on the RP observed by annual GPS measurements during 2000–2006 is consistent with the oblique plate boundary motion on a regional scale. This study and the study by Árnadóttir *et al.* (2006) have resolved a significant component of opening perpendicular to the RP plate boundary. Here, we have also mapped the temporal and spatial variations in velocity and strain rate fields within the plate boundary zone with a previously unattained level of detail.

We observe a small, but consistent increase in eastward velocity at several stations on the southern RP from 1993–1998 to 2000–2006, indicating that the relative plate motion across the peninsula may have increased. We also observe subtle velocity variations in the Kleifarvatn area, which may be related to stress changes following the moderate earthquakes in 2000 June and 2003 August. We find that the observed surface deformation on the RP can be approximated by deep motion along the plate boundary with left-lateral motion 18^{+4}_{-3} mm yr^{-1} and opening of 7^{+3}_{-2} mm yr^{-1} below a locking depth of 7^{+1}_{-2} km. The resulting deep motion of 20^{+4}_{-3} mm yr^{-1} in the direction of N(100^{+8}_{-6})°E agrees well with the predicted relative NA–EU rate on the RP. Our modelling indicates that there may be a partitioning of the oblique plate motion in the upper crust, so that the left-lateral shear is taken up by the seismically active NS-oriented strike-slip faults, while the opening is mainly accommodated within the fissure swarms. The kinematic models are, however, non-unique due to the data limitations and the complexity of the region, and more advanced models are needed to fully explain the observed surface deformation.

We have calculated the areal and shear strain rates using the 1993–1998 velocities from Hreinsdóttir *et al.* (2001) and the 2000–2006 velocities from this study. The regional plate boundary deformation forms an E–W trending zone of left-lateral shear strain rates, which are perturbed by shallow deformation due to volcanic unrest, geothermal fluid extraction, and possibly seismic activity.

The eastern RP is characterized by pronounced areal and shear strain rate anomalies during 1993–1998, and very low shear strain rates during 2000–2006. The high 1993–1998 rates are not reproduced by our kinematic model, indicating additional sources of deformation, probably related to the 1994–1998 inflation and elevated seismicity in the Hengill–Hrómundartindur volcanic system. The low shear strain rates during 2000–2006 suggest that the eastern RP is in a stress shadow following the 1994–1998 activity. Geothermal fluid extraction at the Svartsengi geothermal power plant causes continued subsidence in the area, although the rate of subsidence has

decreased since the 1990s. A signal of contraction is also observed in the central Hengill area during 2000–2006, most likely due to subsidence or local faulting caused by geothermal fluid extraction. High shear strain rates on the central RP during 2000–2006 may be related to elevated background seismicity in this area.

REFERENCES

Antonioli, A., Belardinelli, M.E., Bizzarri, A. & Vogfjörd, K.S., 2006. Evidence of instantaneous dynamic triggering during the seismic sequence of year 2000 in south Iceland, *J. geophys. Res.,* **111,** B03302, doi:10.1029/2005JB003935.

Árnadóttir, T., Geirsson, H. & Einarsson, P., 2004. Coseismic stress changes and crustal deformation on the Reykjanes Peninsula due to triggered earthquakes on 17 June 2000, *J. geophys. Res.,* **109,** B09307, doi:10.1029/2004JB003130.

Árnadóttir, T., Jiang, W., Feigl, K.L., Geirsson, H. & Sturkell, E., 2006. Kinematic models of plate boundary deformation in southwest Iceland derived from GPS observations, *J. geophys. Res.,* **111,** B07402, doi:10.1029/2005JB003907.

Beavan, J. & Haines, J., 2001. Contemporary horizontal velocity and strain rate fields of the Pacific-Australian plate boundary zone through New Zealand, *J. geophys. Res.,* **106**(B1), 741–770.

Brander, J.L., Mason, R.G. & Calvert, R.W., 1976. Precise distance measurements in Iceland, *Tectonophysics,* **31,** 193–206.

Bödvarsson, R., Rögnvaldsson, S.T., Slunga, R. & Kjartansson, E., 1999. The SIL data acquisition system—at present and beyond year 2000, *Phys. Earth planet. Inter.,* **113,** 89–101.

Buck, W.R., Einarsson, P. & Brandsdóttir, B., 2006. Tectonic stress and magma chamber size as controls on dike propagation: constraints from the 1975–1984 Krafla rifting episode, *J. geophys. Res.,* **111,** B12404, doi:10.1029/2005JB003879.

Cervelli, P., Murray, M.H., Segall, P., Aoki, Y. & Kato, T., 2001. Estimating source parameters from deformation data, with an application to the March 1997 earthquake swarm off the Izu Peninsula, Japan, *J. geophys. Res.,* **106**(B6), 11 217–11 238.

Clifton, A.E. & Kattenhorn, S.A., 2006. Structural architecture of a highly oblique divergent plate boundary segment, *Tectonophysics,* **419,** 27–40.

Clifton, A.E. & Schlische, R.W., 2003. Fracture populations on the Reykjanes Peninsula, Iceland: comparison with experimental clay models of oblique rifting. *J. geophys. Res.,* **108**(B2), 2074, doi:10.1029/2001JB000635.

Clifton, A.E., Sigmundsson, F., Feigl, K.L., Gudmundsson, G. & Árnadóttir, T., 2002. Surface effects of faulting and deformation resulting from magma accumulation at the Hengill triple junction, SW Iceland, 1994–1998, *J. Volc. Geotherm. Res.,* **115,** 233–255.

Clifton, A.E., Pagli, C., Jónsdóttir, J.F., Eythorsdóttir, K. & Vogfjörd, K., 2003. Surface effects of triggered fault slip on Reykjanes Peninsula, SW, Iceland, *Tectonophysics,* **369,** 145–154.

DeMets, C., Gordon, R.G., Argus, D.F. & Stein, S., 1994. Effect of recent revisions to the geomagnetic reversal time scale on estimates of current plate motions, *Geophys. Res. Lett.,* **21**(20), 2191–2194.

Efron, B. & Tibshirani, R., 1986. Bootstrap methods for standard errors, confidence intervals, and other measures of statistical accuracy, *Stat. Sci.,* **1**(1), 54–75.

Einarsson, P., 1991. Earthquakes and present-day tectonism in Iceland, *Tectonophysics,* **189,** 261–279.

Einarsson, P. & Sæmundsson, K., 1987. Earthquake epicenters 1982–1985 and volcanic systems in Iceland (map), in *Í Hlutarsins Edli: Festschrift for Thorbjorn Sigurgeirsson,* ed. Sigfússon, T., Menningarsjódur, Reykjavík.

Einarsson, P., Björnsson, S., Foulger, G., Stefánsson, R. & Skaftadóttir, T., 1981. Seismicity pattern in the South Iceland seismic zone, in *Earthquake Prediction–An International Review,* Maurice Ewing Ser. Vol. 4, eds Simpson, D. & Richards, P., Am. Geophys. Union, 141–151.

Erlendsson, P. & Einarsson, P., 1996. The Hvalhnúkur fault, a strike-slip fault mapped within the Reykjanes Peninsula oblique rift, Iceland, in *Seismology in Europe, XXV ESC General Assembly,* pp. 498–505, ed. Thorkelsson, B., Icelandic Meteorological Office, Reykjavík.

Eysteinsson, H., 1993. Leveling and gravity measurements in the outer part of the Reykjanes Peninsula 1992, *Sci. rep. OS-93029,* Nat. Energy Auth., Reykjavík, Iceland.

Eysteinsson, H., 2000. Elevation and gravity changes at geothermal fields on the Reykjanes Peninsula, SW Iceland, *Proceedings World Geothermal Congress 2000,* 559–564.

Feigl, K.L., Gasperi, J., Sigmundsson, F. & Rigo, A., 2000. Crustal deformation near Hengill volcano, Iceland 1993–1998: Coupling between magmatic activity and faulting inferred from elastic modeling of satellite radar interferograms, *J. geophys. Res.,* **105**(B11), 25 655–25 670.

Foulger, G.R., Bilham, R., Morgan, W.J. & Einarsson, P., 1987. The Iceland GPS geodetic field campaign 1986, *EOS, Trans. Am. geophys. Un.,* **68,** p. 1809.

Geirsson, H. et al., 2006. Current plate movements across the Mid-Atlantic Ridge determined from 5 years of continuous GPS measurements in Iceland, *J. geophys. Res.,* **111,** B09407, doi:10.1029/2005JB003717.

Haines, A.J., Jackson, J.A., Holt, W.E. & Agnew, D.C., 1998. Representing distributed deformation by continuous velocity fields, *Sci. rep. 98/5,* Institute of Geology and Nuclear Science, Lower Hutt, New Zealand, pp. 110.

Herring, T.A., 2003. GLOBK: Global Kalman filter VLBI and GPS analysis program version 4.1, *Tech. rep.,* Massachusetts Institute of Technology, Cambridge.

Hjaltadóttir, S., Geirsson, H. & Skaftadóttir, T., 2005. Seismic activity in Iceland during 2004, *Jökull,* **55,** 107–119.

Hreinsdóttir, S., Einarsson, P. & Sigmundsson, F., 2001. Crustal deformation at the oblique spreading Reykjanes Peninsula, SW Iceland: GPS measurements from 1993 to 1998, *J. geophys. Res.,* **106**(B7), 13 803–13 816.

Hugentobler, U., Schaer, S. & Fridez, P., 2001. Bernese GPS software version 4.2, Astronomical Institute, University of Berne, Switzerland.

Jakobsdóttir, S.S., Gudmundsson, G.B. & Stefánsson, R.S., 2002. Seismicity in Iceland 1991-2000 monitored by the SIL seismic system, *Jökull,* **51,** 87–94.

Jakobsson, S.P., Jónsson, J. & Shido, F., 1978. Petrology of the Western Reykjanes Peninsula, Iceland, *J. Petrol.,* **19**(4), 669–705.

Kreemer, C., Holt, W.E. & Haines, A.J., 2003. An integrated global model of present-day plate motions and plate boundary deformation, *Geophys. J. Int.,* **154,** 8–34.

LaFemina, P.C., Dixon, T.H., Malservisi, R., Árnadóttir, T., Sturkell, E., Sigmundsson, F. & Einarsson, P., 2005. Geodetic GPS measurements in

south Iceland: Strain accumulation and partitioning in a propagating ridge system, *J. geophys. Res.,* **110,** B11405, doi:10.1029/2005JB003675.

Magnússon, I.T. & Thorbergsson, G., 2004. GPS-mæ lingar á utanverdum Reykjanesskaga 2004, *Sci. rep. IV Hluti,* Iceland GeoSurvey, Reykjavík.

McClusky, S. *et al.,* 2000. Global Positioning System constraints on plate kinematics and dynamics on the eastern Mediterranean and Caucasus, *J. geophys. Res.,* **105**(B3), 5695–5720.

Mogi, K., 1958. Relations between the eruptions of various volcanoes and the deformations of the ground surfaces around them, *Bull. Earthquake Res. Inst. Univ. Tokyo,* **36,** 99–134.

Okada, Y., 1985. Surface deformation due to shear and tensile faults in a half-space, *Bull. seism. Soc. Am.,* **75**(4), 1135–1154.

Pagli, C., Pedersen, R., Sigmundsson, F. & Feigl, K.L., 2003. Triggered fault slip on June 17, 2000 on the Reykjanes Peninsula, SW-Iceland captured by rader interferometry, *Geophys. Res. Lett.,* **30**(6), doi:10.1029/2002GL015310.

Sella, G.F., Dixon, T.H. & Mao, A., 2002. REVEL: A model for Recent plate velocities from space geodesy, *J. geophys. Res.,* **107**(B4), 2081, doi:10.1029/2000JB000033.

Sigmundsson, F., Einarsson, P., Bilham, R. & Sturkell, E., 1995. Rift-transform kinematics in south Iceland: deformation from Global Positioning System measurements, 1986 to 1992, *J. geophys. Res.,* **100**(B4), 6235–6248.

Sigmundsson, F., Einarsson, P., Rognvaldsson, S., Foulger, G., Hodgkinson, K. & Thorbergsson, G., 1997. The 1994–1995 seismicity and deformation at the Hengill triple junction, Iceland: Triggering of earthquakes by minor magma injection in a zone of horizontal shear stress, *J. geophys. Res.,* **102**(B7), 15 151–15 161.

Sturkell, E., Sigmundsson, F., Einarsson, P. & Bilham, R., 1994. Strain accumulation 1986–1992 across the Reykjanes Peninsula plate boundary, Iceland, determined from GPS measurements, *Geophys. Res. Lett.,* **21**(2), 125–128.

Sæmundsson, K., 1974. Evolution of the axial rifting zone in northern Iceland and the Tjörnes fracture zone, *Geol. Soc. Am. Bull.,* **85,** 495–504.

Sæmundsson, K., 1978. Fissure swarms and central volcanoes of the neo-volcanic zones of Iceland, *Geol. J. Special Issue,* **10,** 415–432.

Sæmundsson, K. & Einarsson, S., 1980. Geological map of Iceland, sheet 3, SW-Iceland, second edition, scale 1:250,000, Museum of Natural History and the Iceland Geodetic Survey, Reykjavík.

Stein, S. & Gordon, R.G., 1984. Statistical tests of additional plate boundaries from plate motion inversions. *Earth planet. Sci. Lett.,* **69,** 401–412.

Thordarson, T. & Larsen, G., 2007. Volcanism in Iceland in historical time: Volcano types, eruption styles and eruptive history, *J. Geodyn.,* **43,** 118–152.

Vadon, H. & Sigmundsson, F., 1997. Crustal deformation from 1992 to 1995 at the mid-Atlantic ridge, southwest Iceland, mapped by satellite radar interferometry, *Science,* **275,** 193–197.

Vogfjörd, K.S., 2003. Triggered seismicity in SW Iceland after the June 17, Mw = 6.5 earthquake in the south Iceland seismic zone: The first five mintues, *Geophys. Res. Abstr.,* **5,** Abstract EAE03-A-11251.

Vogfjörd, K.S., Geirsson, H. & Sturkell, E., 2004. Krísuvíkurhrinan í ágúst 2003: kortlagning brotflata med eftirskjálftum og GPS mælingum, *Geoscience Society of Iceland. Spring Meeting 2004,* p. 41.

Vogfjörd, K.S., Hjaltadóttir, S. & Slunga, R., 2005. Volcano-tectonic interaction in the Hengill region, Iceland during 1993–1998, *Geophys. Res. Abstracts,* **Vol. 7,** EGU05-J-09947, EGU General Assembly, Vienna, Austria.

Wessel, P. & Smith, W.H.F., 1998. New, improved version of the Generic Mapping Tools released. *EOS, Trans. Am. geophys. Un.,* **79,** p. 579.

Paper II

Keiding, M., B. Lund, and T. Árnadóttir, 2009. Earthquakes, stress and strain along an obliquely divergent plate boundary: the Reykjanes Peninsula, southwest Iceland, *J. Geophys. Res.*, **114**, doi:10.1029/2008JB006253.

Click Here for Full Article

Earthquakes, stress, and strain along an obliquely divergent plate boundary: Reykjanes Peninsula, southwest Iceland

M. Keiding,[1] B. Lund,[2] and T. Árnadóttir[1]

[1]   We investigate the seismicity and the state of stress along the obliquely divergent Reykjanes Peninsula plate boundary and compare the directions of stress from inversion of earthquake focal mechanisms with the directions of strain rate from GPS data. The seismicity on the peninsula since early instrumental recordings in 1926 shows a systematic change from primarily earthquake swarms in the west to main shock–aftershock sequences in the east. The largest earthquakes on the Reykjanes Peninsula typically occur by right-lateral slip on N-S faults and reach magnitude 6 on the eastern part of the peninsula. During 1997–2006 most earthquakes on the Reykjanes Peninsula were located in two areas, Fagradalsfjall and Krísuvík on the central part of the peninsula, as recorded by the South Iceland Lowland (SIL) seismic network. The state of stress estimated by inversion of microearthquake focal mechanisms from the SIL catalogue is mainly oblique strike slip, with a tendency toward a normal stress state. Mapping the directions of the least compressive horizontal stress ($S_{h\min}$) shows an average $S_{h\min}$ direction of N(120±6)°E and a remarkable agreement with the directions of greatest extensional strain rate ($\dot{\epsilon}_{H\max}$) derived from GPS velocities during 2000–2006. The agreement between the directions of stress at depth and strain rate observed at the surface indicate that the earthquakes are primarily driven by plate motion.

Citation: Keiding, M., B. Lund, and T. Árnadóttir (2009), Earthquakes, stress, and strain along an obliquely divergent plate boundary: Reykjanes Peninsula, southwest Iceland, *J. Geophys. Res.*, *114*, B09306, doi:10.1029/2008JB006253.

1.   Introduction

[2]   During recent years, the vast increase in geodetic observations of crustal deformation as well as earthquake recordings has considerably improved our understanding of the behavior of plate boundary zones. The strain rates of the Earth's deforming plate boundaries have been mapped using primarily geodetic data or geologic fault slip data [e.g., *Haines and Holt*, 1993]. Seismically derived strain rates have proved useful for strain inversions of geodetic data, by adding constraints on the style and direction of deformation in areas where the geodetic data are sparse [e.g., *Kreemer et al.*, 2003; *Delescluse and Chamot-Rooke*, 2007]. Complimentary to the kinematic information from geodesy, mapping of the directions of horizontal stress in the crust, using earthquake, borehole and geologic data, is becoming increasingly important in the interpretation of plate boundary interactions and the mechanics of plate bounding fault zones [e.g., *Hardebeck and Michael*, 2004; *Townend and Zoback*, 2004], volcanic eruptions [*Roman et al.*, 2004], and large earthquakes [*Bohnhoff et al.*, 2006].

[3]   In areas where sufficient geodetic data and earthquake recordings are available it is possible to relate the brittle seismic deformation at depth with the distributed strain at the surface. To date, only a few studies have compared stress estimates obtained from earthquake data with geodetic strain rates. *Becker et al.* [2005] used joint inversion of GPS velocities and stress observations to improve the estimates of fault slip rates in the San Andreas fault system. *Townend and Zoback* [2006] compared the directions of stress and geodetic strain rates in Japan, with the aim to evaluate how crustal stresses are related to the horizontal strain rates produced by different tectonic processes. They found that the directions of greatest compressive horizontal stress obtained from intraplate crustal earthquake data agreed well with the direction of greatest contractional strain rate only after the effects of interseismic subduction thrust locking on geodetic observations had been subtracted. In the complex tectonic setting of Japan the strain rates are caused by both subduction thrusts and mountain-building processes, while the stresses reflect only the latter. Our approach in this study is similar to that of *Townend and Zoback* [2006].

[4]   In this paper, we investigate the seismicity and seismically derived state of stress along the oblique divergent plate boundary on the Reykjanes Peninsula and compare these to the surface deformation observed by GPS. We present a review of the seismicity on the Reykjanes Peninsula since the start of instrumental earthquake recordings in

[1]Nordic Volcanological Centre, Institute of Earth Sciences, University of Iceland, Reykjavík, Iceland.
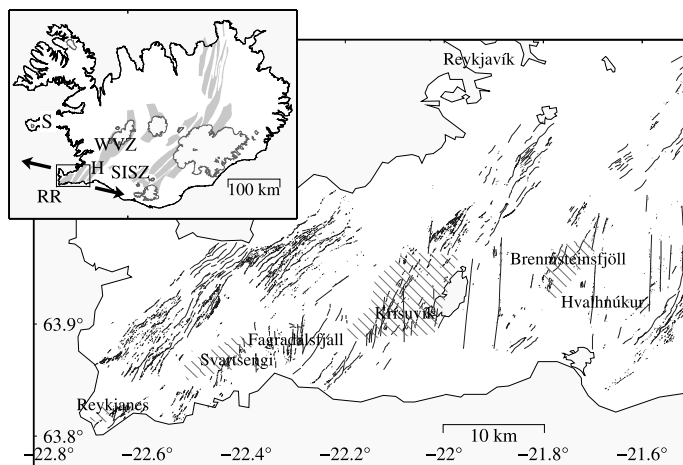[2]Department of Earth Sciences, Uppsala University, Uppsala, Sweden.

Figure 1. Tectonic map of the Reykjanes Peninsula, with fracture locations from *Clifton and Kattenhorn* [2006]. The fractures are mainly NE-SW trending normal faults arranged within three volcanic fissure swarms, the Reykjanes, Krísuvík, and Brennisteinsfjöll fissure swarms [*Sæmundsson*, 1978]. The hatched areas show the locations of high-temperature geothermal fields. The Iceland inset shows the neovolcanic zones (grey shades) and the location of the study area. H, Hengill volcano; RR, Reykjanes Ridge; WVZ, western Volcanic Zone; SISZ, South Iceland Seismic Zone; S, Snæfellsnes Peninsula. The arrows show the direction of the full 2 cm/a spreading across the RP between North America and Eurasia.

Iceland in 1926. The seismicity during 1997–2006 is analyzed in more detail, using earthquake locations, magnitudes, and focal mechanisms from the South Iceland Lowland (SIL) seismic network operated by the Icelandic Meteorological Office [*Bödvarsson et al.*, 1999; *Jakobsdóttir*, 2008]. We estimate the state of stress by inversion of microearthquake focal mechanisms, and compare the directions of stress with the directions of strain rate derived from GPS velocities. We find that the state of stress is mainly oblique strike slip with a tendency toward a normal stress state, reflecting the transtensional nature of the plate boundary. The stress directions we estimate are consistent with the geodetic strain rate directions, indicating that the earthquakes are driven by the tectonic stresses induced by the plate motion.

2. Tectonic Background

[5] The active plate boundary in Iceland is considerably offset from the offshore Mid-Atlantic Ridge due to the presence of the mantle plume beneath Iceland. As a result, most of the plate boundary in Iceland is oriented at an oblique angle with respect to the overall direction of plate motion, such as the Reykjanes Peninsula (RP) plate boundary, which accommodates both left-lateral transform motion and extension (Figure 1). The plate boundary along the RP is expressed as a zone of high seismicity and recent volcanism, forming the transition from the offshore Reykjanes Ridge in the west to the South Iceland Seismic Zone in the east [*Einarsson*, 1991]. Rifting on the Reykjanes Peninsula began after a ridge jump from the Snæfellsnes Peninsula

6–7 Ma ago [*Sæmundsson*, 1978]. According to plate motion models, North America and Eurasia are currently moving apart at a rate of 19–20 mm/a in a direction of N(101–103)°E at 63.9°N, 22.0°W [*DeMets et al.*, 1994; *Sella et al.*, 2002].

[6] The plate boundary on the RP can be defined as a narrow zone of seismicity, forming the shallow expression of a deeper-seated and aseismic deformation zone [*Klein et al.*, 1977; *Einarsson*, 1991]. The zone of seismicity trends approximately N80°E on the central RP, but bends toward south on the western part of the peninsula, before connecting to the offshore Reykjanes Ridge. Pioneering earthquake surveys on the western part of the peninsula revealed that the seismic zone is not a single fault but rather a series of strike-slip and normal faults [*Klein et al.*, 1973, 1977]. The obliquity of the plate boundary deformation on the RP was first documented by a geodetic study using precise distance measurements from 1968–1972, which indicated a combination of left-lateral motion and extension [*Brander et al.*, 1976]. Recent kinematic modeling of GPS data from 2000–2006 confirms that the deformation is consistent with the predicted oblique spreading on the RP between North America and Eurasia [*Árnadóttir et al.*, 2006; *Keiding et al.*, 2008].

[7] The main tectonic features on the peninsula are a large number of NE-SW trending volcanic fissures and normal faults and a series of N-S oriented right-lateral strike-slip faults [*Clifton and Kattenhorn*, 2006] (Figure 1). The fissures and normal faults are grouped into a number of fissure swarms arranged in a right-stepping en echelon pattern, from west to east they are the Reykjanes, Krísuvík
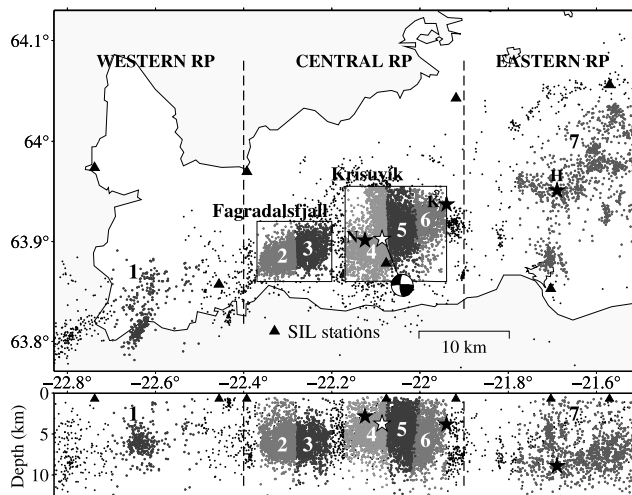
Figure 2. Time versus longitude plot of $M_L \geq 4$ earthquakes on the Reykjanes Peninsula during 1926–2006. The magnitudes are Icelandic local magnitude (M_L), unless otherwise indicated. The stars indicate main shocks; circles are swarms or undefined events.

and Brennisteinsfjöll fissure swarms on the RP and the Hengill fissure swarm located immediately east of our study area [*Sæmundsson*, 1978]. A number of high-temperature geothermal fields are present on the peninsula, the largest of which is the Krísuvík field on the central RP. Energy has been harnessed from the Svartsengi field since 1976, causing a localized bowl of subsidence revealed by GPS and interferometric synthetic aperture radar (InSAR) [*Vadon and Sigmundsson*, 1997; *Hreinsdóttir et al.*, 2001; *Arnadóttir et al.*, 2006; *Keiding et al.*, 2008]. The NE-SW trending volcanic fissures and normal faults are crosscut by a number of kilometer-scale near-vertical N-S right-lateral strike-slip faults. The N-S faults are sometimes difficult to trace at the surface and some have been mapped by earthquakes alone [*Clifton and Kattenhorn*, 2006]. The largest earthquakes on the RP occur on these faults, reaching magnitude 6 on the eastern part of the peninsula. The N-S faults are the surface expressions of the E-W shear at depth, and as such resemble the bookshelf faulting in the South Iceland Seismic Zone.

[8] The crustal structure along the Reykjanes Peninsula has been imaged by a number of seismic tomography studies. Results of an offshore-onshore seismic experiment in 1996 indicate that the crustal thickness on the peninsula increases from 14 km in the west to 17 km in the east [*Weir et al.*, 2001]. Relatively low velocities down to depths of 6–8 km are observed along the central part of the plate boundary zone, correlating well with the distribution of volcanic centers [*Tryggvason et al.*, 2002]. A tomography study using five months of local microearthquake data suggests localized anomalies of low Vp/Vs ratios in the geothermal fields of Svartsengi and Krísuvík, interpreted as zones of increased fluid temperature and pressure [*Geoffroy and Dorbath*, 2008].

3. Seismicity on the Reykjanes Peninsula

[9] Here we present an overview of the seismicity on the Reykjanes Peninsula since the first instrumental earthquake

recordings in Iceland in 1926. During 1926–1951 only one seismometer was operating in Iceland, a Mainka instrument installed in Reykjavík, but a seismic network was initiated in 1951. The catalogue for southwest Iceland is assumed to be complete down to magnitude 4 from 1926, and down to magnitude 2.5 during 1967–1991. The first SIL seismic station was installed on the Reykjanes Peninsula in 1991, and by 1997 there were seven stations. No changes were made in the station configuration during 1997–2006.

[10] A compilation of $M \geq 4$ earthquakes recorded on the Reykjanes Peninsula during 1926–2006 is summarized in Figure 2 (see also auxiliary material).[1] The 1926–1990 earthquake data are from the Seismological Bulletin of the Icelandic Meteorological Office as well as reports published by the Science Institute at the University of Iceland [*Ottósson*, 1980; *Tryggvason*, 1978a, 1978b, 1979]. The Seismological Bulletin reports local magnitude (M_L) estimates with quarter fractions for the oldest data, and with one decimal place from 1951. The 1991–2006 data are from the SIL catalogue, reported as M_L with one decimal place. The Icelandic local magnitude scale saturates around $M_L 5.5$; hence, the largest events are reported either with surface wave magnitudes (M_S) from the international catalogues [*Tryggvason*, 1973], or from other sources as specified.

3.1. Seismicity During 1926–1996

[11] Since 1926, periods of high seismicity on the RP have occurred at an interval of 25–30 years. High seismicity was observed during the early 1930s, the mid-1950s, during 1967–1977, and most recently in 2000. Both earthquake swarms and main shock–aftershock sequences are observed on the Reykjanes Peninsula. We refer to a sequence as a main shock–aftershock sequence if it is initiated by a main shock that is at least 1.2 magnitudes larger than the largest aftershock, according to Båth's law [*Båth*, 1973]. We refer to a sequence as a swarm if it builds up and terminates gradually and is not dominated by a single large earthquake [*Mogi*, 1962; *Hainzl*, 2004].

[12] A systematic change in the pattern of seismicity is observed along the RP (Figure 2). The western RP (west of 22.4°W) is characterized by mostly swarm activity, and rare main shock–aftershock sequences. High seismicity was observed in the west during 1928–1936, including one or two moderate main shocks and a very intense swarm with at least 12 $M_L 4-4\frac{3}{4}$ earthquakes. The eastern RP (east of 21.9°W), on the other hand, is characterized by main shock–aftershock sequences, while swarms in this area are rare. On 23 July 1929 a main shock with $M_S 6\frac{1}{4}$ struck in Brennisteinsfjöll on the eastern RP. This is the largest instrumentally recorded earthquake on the Reykjanes Peninsula, and is inferred to have been located on the Hvalhnúkur fault [*Erlendsson and Einarsson*, 1996]. Another main shock ($M_S 6.0$) struck in Brennisteinsfjöll in 1968. The central part of the peninsula acts as a transition between these two styles of seismicity, with both swarms and main shock–aftershock sequences. In 1933 a main shock with $M_S 6.0$ struck on the central RP, and several swarms and moderate main shocks occurred in the area during the 1950s and 1967–1977.

Figure 3. Map and depth profile showing hypocenter locations for 16,000 earthquakes from the SIL seismic catalogue recorded during 1997–2006. The four stars show hypocenters of $M_W \geq 5$ earthquakes on 17 June 2000 (three black stars labeled N, K, and H for the Núpshlídarháls, Kleifarvatn, and Hvalhnúkur events, respectively) and 23 August 2003 (white star). The numbers and grey scale coloring of the earthquakes show seven spatial subsets used for the stress tensor inversions in Figure 7.

3.2. Seismicity During 1997–2006

[13] The SIL network is optimized for microearthquakes and records events down to M_L less than zero in the areas with the densest network. The SIL catalogue for 1997–2006 includes a total of 16,000 events in the area shown in Figure 3. Most of these events were located in the Fagradalsfjall and Krísuvík areas on the central part of the peninsula, while very few events were located on the western and eastern RP. The earthquakes are mainly located at 2–9 km depth. The SIL hypocenter locations on the RP usually have uncertainties of 1–2 km in the horizontal direction and 4–7 km in the vertical direction. Recent work on the velocity model on the Reykjanes Peninsula indicates that the earthquake depths reported in the SIL catalogue, and used here, may be a little too deep (K. Vogfjörd, personal communication, 2008).

[14] The earthquakes in the Fagradalsfjall area form a spatially dense cluster, mostly located at 4–8 km depth (Figure 3). The seismicity is characterized by pronounced swarm activity superimposed on a relatively low background rate (Figure 4). Three swarms of $M_L < 4$ events occurred in the area during 1997–2006, in August 1998, in November 2000, and in July 2004. Each of the swarms lasted a few days and typically built-up and terminated gradually, and included occasional subswarms or embedded main shock–aftershock sequences.

[15] The earthquakes in the Krísuvík area cover a larger area than in Fagradalsfjall and show considerable variation in depth (Figure 3). The deepest earthquakes reach 9 km in the NE part of the area but only 6 km in the SW part. The shallowest earthquakes are located in the central Krísuvík area, where considerable geothermal alteration is observed

at the surface. Both earthquake swarms and main shock–aftershock sequences occurred in the Krísuvík area during 1997–2006. A high background seismicity rate was observed during 1997–2000, with an intense swarm during June–July 1999 (Figure 4). The summer 1999 activity occurred in a series of localized, short-lived subswarms and embedded main shock–aftershock sequences, initiated by $M_L 3.0–3.8$ events.

[16] An earthquake sequence in southwest Iceland was initiated on 17 June 2000 by a $M_W 6.5$ earthquake in the South Iceland Seismic Zone. Within 5 min of this main shock, three moderate size earthquakes were triggered on the RP, up to a distance of 80 km [e.g., *Antonioli et al.*, 2006]. The triggered events were located on the Hvalhnúkur fault in Brennisteinsfjöll and on the Kleifarvatn and Núpshlídarháls faults in the Krísuvík area (see Figure 3). The magnitudes, mechanisms and precise locations of these secondary events could not be determined from the SIL seismic data because the waveforms of the main shock and the triggered events interfered [*Antonioli et al.*, 2006]. Instead moment magnitudes (M_W), ranging from 5.4 to 5.9, were estimated from geodetic models of the surface deformation observed by GPS and InSAR [*Pagli et al.*, 2003; *Árnadóttir et al.*, 2004; *Sudhaus and Jónsson*, 2009]. Surprisingly, few aftershocks were observed following the triggered earthquakes on the RP. Some aftershocks occurred on the Hvalhnúkur and Kleifarvatn faults, but hardly any aftershocks were recorded on the Núpshlídarháls fault [*Hjaltadóttir and Vogfjörd*, 2005].

[17] Following the June 2000 events there was a sharp decrease in the seismicity rate in the Krísuvík area (Figure 4). On 23 August 2003, a $M_W 5.0$ event struck another N-S
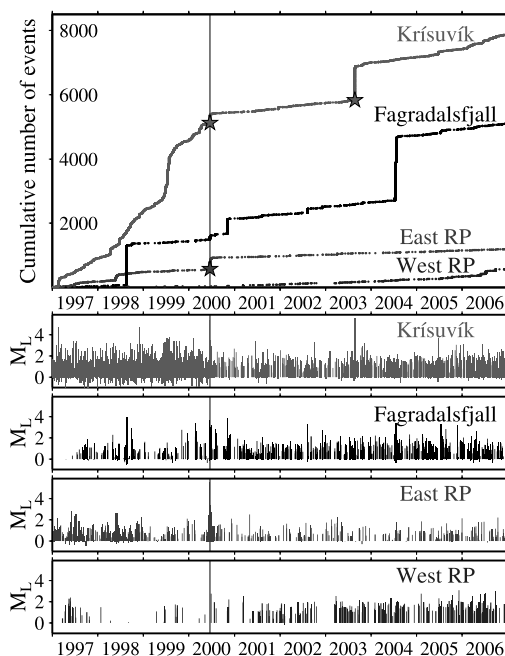
Figure 4. Time series of cumulative number of earthquakes and local magnitudes (M_L) for the western Reykjanes Peninsula, Fagradalsfjall, Krísuvík, and the eastern Reykjanes Peninsula (see Figure 3). The vertical line shows the time of the June 2000 events, and the stars show $M_W \geq 5$ events.

strike-slip fault in the Krísuvík area. The main shock was followed by more than one thousand aftershocks at 1.5–5 km depth. Half of the aftershocks were located on the same fault as the main shock, while the other half were located on a series of intervening short fault segments in the NE quadrant of the main fault [*Vogfjörd et al.*, 2004]. Static Coulomb failure stress calculations indicate that the 2003 event may have been advanced by a positive stress change due to the June 2000 earthquakes in the area [*Árnadóttir et al.*, 2004]. The seismicity in the Krísuvík area is increasing again following August 2003, but it has not reached the level of activity observed during the late 1990s.

[18] Interestingly, there is no apparent correlation between the seismicity rates in the Fagradalsfjall and Krísuvík areas during 1997–2006. The background rate in the Fagradalsfjall area is consistently low during the entire period, and does not reflect the high seismicity rate observed in the Krísuvík area during 1997–2000. The June 2000 events seem to have released stresses in the Krísuvík area and brought the rate down so that it resembles that observed in the Fagradalsfjall area, with episodic bursts of activity superimposed on a relatively low background rate. This difference in the seismicity rates in the two areas suggests that they may be affected by different, local triggering mechanisms.

3.3. Moment Accumulation and Release

[19] An estimate of the moment rate that is accumulating along the Reykjanes Peninsula due to plate motion, hereafter referred to as the geometric moment, can be obtained from a simple approximation of the plate boundary, using the relationship $M_0 = \mu s A$, where μ is the shear modulus, s is the deep slip rate, and A is the slip area. The value of the shear modulus is not well know, but it probably is in the range 10–40 GPa for basaltic rock [e.g., *Schultz*, 1995], and a value of $\mu = 30$ GPa is adopted here. Some constraints on the slip rate and locking depth on the RP is provided by a kinematic model from *Keiding et al.* [2008], in which the plate boundary is approximated using vertical dislocations with both left-lateral motion and opening in elastic half-space [*Okada*, 1985]. The central and eastern RP plate boundary is modelled as a single N79°E trending dislocation, with 18 ± 2 mm/a left-lateral motion and 7 ± 1 mm/a opening below a locking depth of 7 ± 1 km (1σ uncertainties). This corresponds to a total slip rate of 20 ± 2 mm/a in the direction of $N(100^{+4}_{-3})°E$, in good agreement with the plate models [*DeMets et al.*, 1994; *Sella et al.*, 2002]. For the central and eastern RP we use the slip rate and locking depth constrained by our kinematic model. However, the locking depth and slip rate on the western RP are not well resolved by the model due to the change in the trend of the plate boundary, local subsidence around the Svartsengi geothermal power plant and the trade-off between the locking depth and slip rate, as discussed by *Keiding et al.* [2008]. We therefore compute the geometric moment on the western RP by assuming the same slip rate as for the central and eastern RP and a slightly shallower locking depth of 5 ± 2 km. Table 1 lists the geometric moments for three segments of the plate boundary: the western, central, and eastern RP (see Figure 3), with 1σ uncertainties propagated from the kinematic model uncertainties on slip rates and locking depths. The estimated total annual geometric moment accumulation due to plate motion across the RP is then equivalent to $M_0 = (23 \pm 3) \times 10^{16}$ N m/a.

[20] Is all the moment accumulated by plate motion released in earthquakes? An estimate of the long-term seismic moment release can be obtained from the compilation of $M_L \geq 4$ earthquakes recorded during 1926–2006. The Icelandic M_L is scaled to the m_b of the international NEIC catalogue (R. Stefánsson, personal communication,

Table 1. Estimated Moment Accumulation From Plate Motion and Moment Release From Earthquakes With 1σ Uncertainties[a]

	s (mm/a)	L (km)	D (km)	Geometric M_0 10^{16} (N m/a)	Seismic M_0 10^{16} (N m/a)
Western RP	20 ± 2[b]	20	5 ± 2	6 ± 2	2 ± 1
Central RP	20 ± 2[b]	24	7 ± 1[b]	9 ± 1	8 ± 2
Eastern RP	20 ± 2[b]	20	7 ± 1[b]	8 ± 1	6 ± 3
Total				23 ± 3	15 ± 4

[a]The geometric moments are computed using the formula $M_0 = \mu s L D$, where μ is the shear modulus (here we use $\mu = 30$ GPa), s is the slip rate, L is the length of the dislocation, and D is the locking depth. The seismic moments are computed from a compilation of $M_L \geq 4$ earthquakes recorded during 1926–2006 (available in auxiliary material), using global earthquake relations [*Scordilis*, 2006; *Kanamori*, 1977] and assuming minimum uncertainties of 0.25 and 0.1 magnitude units for earthquakes before and after 1951, respectively. See Figure 3 for the subdivision into the western, central, and eastern RP.

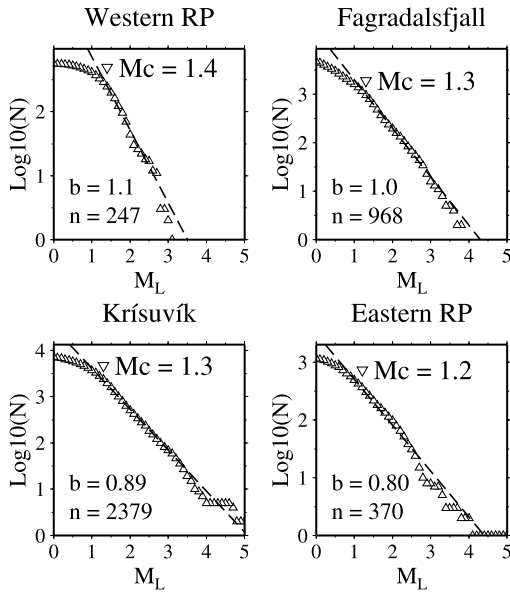[b]Parameters from *Keiding et al.* [2008].

Figure 5. Frequency-magnitude distributions for the western Reykjanes Peninsula, Fagradalsfjall, Krísuvík, and the eastern Reykjanes Peninsula (see Figure 3). The bin size is 0.1 magnitude unit, and M_c is the magnitude of completeness; b is the slope of the stippled line, and n is the number of events with magnitude above M_c.

2008); hence, we examine the $M_L - m_b$ relations in two data sets of 122 events from the Seismological Bulletin of the Icelandic Meteorological Office and 14 events from the SIL catalogue, for which there are NEIC m_b estimates. Regression parameters are computed by assuming equal uncertainties on M_L and m_b and minimizing the Euclidean distance to the line $m_b = \alpha + \beta M_L$ [*Castellaro et al.*, 2006]. We find that β equals 1.0 for both data sets and α equals 0.2 and 0.0 for the Seismological Bulletin and SIL data, respectively. The M_L estimates from the Seismological Bulletin thus appear to be slightly underestimated for $M_L \geq 4$, so we compute the equivalent m_b by adding 0.2 to M_L. For the SIL data we assume $m_b = M_L$. We then compute the equivalent moment using the empirical global relation $M_W = 0.85 m_b + 1.03$ [*Scordilis*, 2006] and the relation $\log_{10} M_0 = 1.5 M_W + 9.1$, where M_0 is in N m [*Kanamori*, 1977]. The seismic moments for each of the three segments of the plate boundary, the western, central and eastern RP, are listed in Table 1. There are no reported uncertainties for the earthquake magnitudes; hence, we assume minimum 1σ uncertainties of 0.25 and 0.1 magnitude units for earthquake data before and after 1951, respectively. Doing so, we estimate a total mean annual seismic moment release of $(15 \pm 4) \times 10^{16}$ N m/a.

[21] We find a reasonable agreement between the estimated moment accumulation from plate motion and the moment released in earthquakes. The seismic moment is smaller than the geometric moment from plate motion for all

three segments of the plate boundary, but the differences are on the order of the uncertainty of the moment estimates. A deficit in the seismic moment could indicate moment accumulation that may be released in future earthquakes or aseismic deformation in the area. The largest difference is observed on the western RP, where the seismic moment is approximately a third of the geometric moment. This apparent discrepancy is more likely due to aseismic moment release on the western RP, rather than significant moment accumulation.

3.4. Magnitude of Completeness and *b* Values

[22] We investigate the earthquake frequency-magnitude distribution along the peninsula to estimate the magnitude of completeness (M_c) and b values for the 1997–2006 catalogue. The Gutenberg-Richter law states that the number of earthquakes is related to their magnitudes by the power law relationship $\log_{10} N(M) = a - bM$, where $N(M)$ is the cumulative number of earthquakes with a magnitude equal to or greater than M. The power law relationship breaks down at the M_c, below which the number of detected earthquakes is usually considered incomplete. Figure 5 shows frequency-magnitude distributions for each of the four areas: the western RP, Fagradalsfjall, Krísuvík, and the eastern RP (see Figure 3). We estimate the magnitude of completeness for each area by manual inspection of the distributions, and find that the M_c decreases from around 1.4 in the western RP to 1.3 on the central RP and approximately 1.2 on the eastern RP. We note that on average, 70% of the recorded events are below M_c.

[23] The b value in the Gutenberg-Richter power law is a measure of the ratio of the number of small earthquakes to the number of large earthquakes and is typically in the range 0.6–1.4 with a global mean of about 1.0. The b value depends on factors such as material heterogeneity [*Mogi*, 1962] or applied shear stress [*Scholz*, 1968]. Low b values, that is, a large proportion of large earthquakes, are inferred to indicate areas of crustal homogeneity and high stress, whereas high b values indicate crustal heterogeneity and low stress. High b values are often observed in volcanic and geothermal areas, where the presence of fluids increase the pore pressure and thus decrease the effective stress [*Wyss*, 1973; *Wiemer and McNutt*, 1997]. However, studies of the seismicity in geothermal fields in the Iceland region have not revealed high b values. On the contrary, a low b value of 0.77 ± 0.10 is estimated for geothermal earthquakes in the Krafla volcanic system in north Iceland [*Arnott and Foulger*, 1994], while intermediate b values ranging 0.9–1.1 are determined for two geothermal systems along the Tjörnes Fracture Zone north of Iceland [*Riedel et al.*, 2003].

[24] In order to map the spatial variations in b values along the RP we divide the earthquake catalogue into smaller subsets, using a nonhierarchical k means clustering algorithm [e.g., *Hartigan*, 1975]. We compute the b values using the maximum likelihood formulation

$$b = \frac{1}{\ln(10)\left(\overline{M} - M_c + \Delta M/2\right)}$$

where $\overline{M}$ is the sample average of the magnitudes, M_c is the magnitude of completeness and ΔM is the bin size [*Utsu*, 1966; *Marzocchi and Sandri*, 2003]. This approximation is
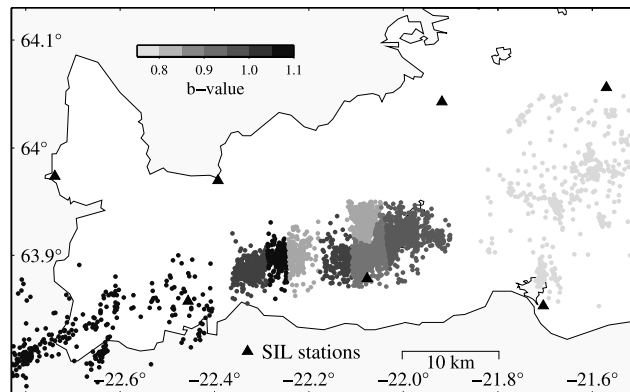
Figure 6. Estimated b values for 11 spatial subsets of 200−500 events larger than the magnitude of completeness. There is one subset on the western RP, three in Fagradalsfjall, six in Krísuvík, and one on the eastern RP. Note that some of the subsets in the Krísuvík area cannot be distinguished by the color scale because of their similar b values.

only strictly valid for a magnitude range of at least 3; hence, we form larger data subsets than other studies typically do [e.g., *Wiemer and McNutt*, 1997]. We choose to form subsets of 200−500 events with magnitudes larger than the magnitude of completeness. This yields 11 subsets, distributed as one subset on the western RP, three in Fagradalsfjall, six in Krísuvík, and one on the eastern RP.

[25] The estimated b values on the RP are in the range 0.77−1.07, determined with 1σ uncertainties of 0.04−0.06 (Figure 6). The highest b value (1.07 ± 0.06) is observed on the western RP, while the lowest (0.77 ± 0.04) is observed on the eastern RP. The western Fagradalsfjall area has relatively high b values (0.97 to 1.05), while the eastern Fagradalsfjall and the Krísuvík area has consistently lower b values (0.84 to 0.95). In summary, we find low to intermediate b values on the Reykjanes Peninsula, indicating relatively high stress. We note that the seismicity we observe in the areas of low Vp/Vs ratios as mapped by *Geoffroy and Dorbath* [2008] are not associated with high b values. Furthermore, relatively high b values are observed in the Fagradalsfjall area where no geothermal activity is manifested at the surface.

4. Focal Mechanisms

[26] The routine SIL analysis estimates focal mechanisms for all events, assuming a double-couple source, using both spectral amplitudes for P, SV, and SH waves and P wave polarities [*Rögnvaldsson and Slunga*, 1993]. In addition to the optimal solution, the SIL algorithm provides a range of acceptable focal mechanisms, within some confidence level of the optimal mechanism. The quality of the focal mechanisms varies with the number of observations and the geometry of the seismic network in the area of the epicenter. We therefore only consider focal mechanisms of events that were registered on at least five stations with a minimum of 23 amplitudes and one polarity determined. We find that the focal mechanisms for offshore events are subject to large uncertainties as they are located outside of the seismic

network; hence, we do not include these mechanisms in our analyses.

[27] For the analysis in this and section 5.2, we choose to divide the earthquake catalogue into seven spatial subsets: one subset on the western RP, two in Fagradalsfjall, three in Krísuvík, and one on the eastern RP, as defined in Figure 3. We illustrate the focal mechanisms within each of the seven subsets using the focal mechanism square after *Slunga* [1991]. This projection is based on the relative magnitudes of the horizontal components of the P and T axes instead of the magnitude of the vertical component as from, e.g., *Frohlich* [2001].

[28] The focal mechanism squares for the seven spatial subsets reveal a mixture of strike-slip, normal as well as reverse mechanisms (Figure 7a). Here, we classify the mechanisms as normal, strike-slip, or reverse depending on which of the P, B, or T axes are closest to vertical. The western RP (subset 1) show large variation with mostly strike slip (53%) but also large amounts of normal and reverse mechanisms. The mechanisms in the Fagradalsfjall area (subsets 2−3) are strike slip or normal, with very few reverse mechanisms (5−6%). The western Fagradalsfjall area (subset 2) has the largest proportion of normal mechanisms of all seven subsets (38%). In the Krísuvík area (subsets 4−6) the mechanisms are mainly strike slip (50−65%), with some normal and reverse mechanisms. The western and central Krísuvík area (subsets 4 and 5) have the largest proportions of reverse mechanisms of all subsets (21−26%). The mechanisms on the eastern RP (subset 7) show large variation but are mostly strike slip (64%). We note that 50−60% of the mechanisms in all seven subsets are intermediate in the sense that none of the P, B, or T axis are within 30° of vertical.

[29] Reverse mechanisms are present in considerable amounts in all areas except in the Fagradalsfjall area, although most of these do not have the T axis within 30° of vertical. Nevertheless, this is surprising given the transtensional nature of the plate boundary. Block faulting may generate reverse mechanisms in some areas, but it is also
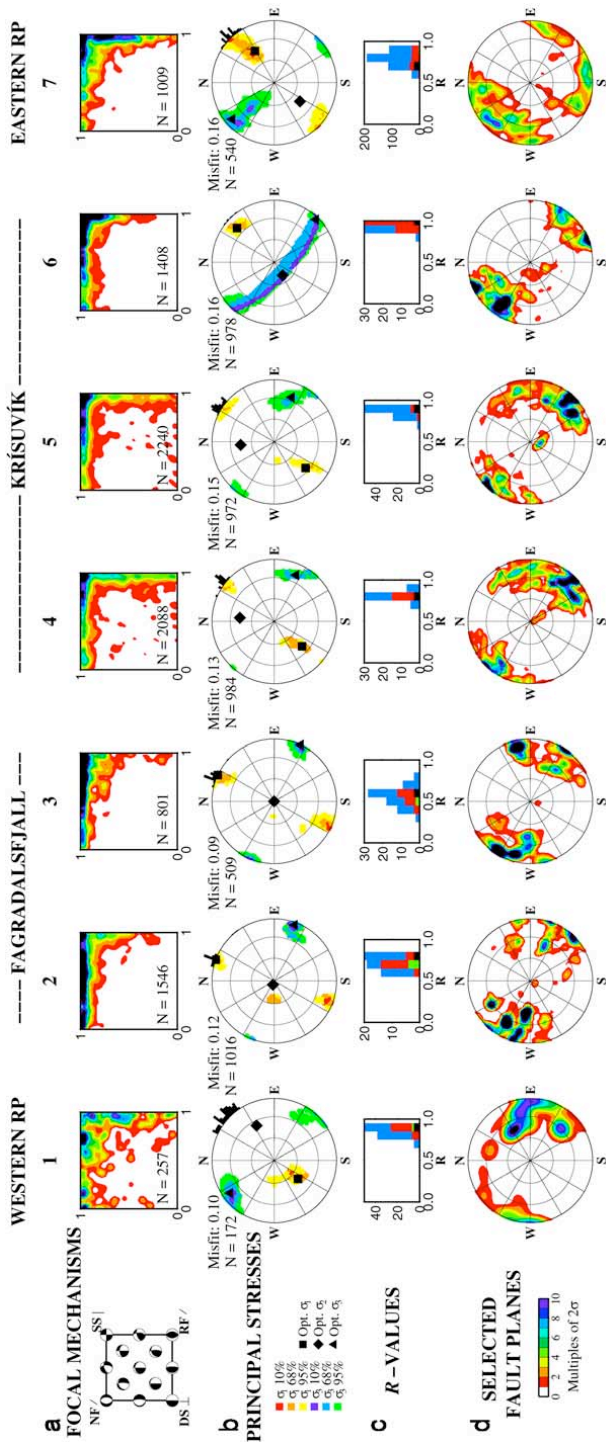
Figure 7. Focal mechanisms and results of stress tensor inversions for seven spatial subsets defined in Figure 3. (a) Contour plots of the focal mechanisms for the seven spatial subsets, the darker colors represent higher density of mechanisms. The top left corner shows a legend for the focal mechanism square after *Slunga* [1991]. The focal mechanism square shows the horizontal components of the moment tensor, which gives normal faulting on 45° faults at (0,1), strike slip on vertical faults at (1,1), reverse faulting on 45° faults at (1,0), and dip slip on vertical faults at (0,0). (b) Principal stress directions on lower hemisphere plots, with confidence regions of σ_1 (warm colors) and σ_3 (cold colors), and the optimal solution (symbols). The directions of greatest compressive horizontal stress, S_{Hmax}, are shown with the histograms on the periphery of the stress tensors. (c) Histograms of the estimated values of $R = (\sigma_1 - \sigma_2)/(\sigma_1 - \sigma_3)$. (d) Fault planes that were selected during the inversions, on lower hemisphere plots of the fault plane normals (Kamb contours).

possible that some events occur on faults that are not oriented optimally with respect to the causative stress state. Most of the events we include have very small magnitudes, and such small events are more likely to occur on nonoptimally oriented faults than larger events. Furthermore, nonoptimal faulting on the RP may be enhanced by weak faults or high pore pressures in the geothermal fields, such as in the Krísuvík geothermal field where we observe the highest proportion of reverse mechanisms. In general, however, it seems like the largest events always occur on N-S oriented near-vertical strike-slip faults. During 1997–2006 almost all the seismic moment on the RP was released in strike-slip events (99%), while very little moment was released in normal faulting (1%) and reverse faulting events (<1%).

5. State of Stress

5.1. Stress Tensor Inversion of Earthquake Focal Mechanisms

[30] We obtain an estimate of the state of stress on the Reykjanes Peninsula by inversion of earthquake focal mechanisms from the SIL catalogue. Most methods of stress tensor inversion [e.g., *Angelier*, 1979; *Gephart and Forsyth*, 1984; *Lund and Slunga*, 1999] are based on two fundamental assumptions: that faults slip in the direction of maximum shear traction on the fault plane [*Bott*, 1959], and that the state of stress is homogeneous within the time and space of the inverted events. The inversion estimates four of the six independent components of the stress tensor, namely the directions of the three principal stresses, $\sigma_1 > \sigma_2 > \sigma_3$, and the relative size of the intermediate principal stress, $R = (\sigma_1 - \sigma_2)/(\sigma_1 - \sigma_3)$.

[31] Prior to the stress tensor inversion, we identify closely located events with similar focal mechanisms, using the amplitude correlation method of *Lund and Bödvarsson* [2002]. A group of similar events does not contribute more than one data point to the inversion; hence, all but the most well determined event are excluded. Not including these redundant events aids a more reliable estimation of the confidence limits of the optimal stress tensor and significantly reduces the computing time.

[32] We use the stress tensor inversion scheme for microearthquake focal mechanisms of *Lund and Slunga* [1999]. The inversion scheme minimizes the absolute angle, within the fault plane, between the directions of computed shear stress τ and observed slip s, $\alpha = \arccos(\tau \cdot s)$. The algorithm performs a grid search through the principal stress directions and R values. The uncertainty in the focal mechanism estimates is accounted for by including a given fraction of the acceptable focal mechanism; hence, for each stress tensor a range of acceptable focal mechanisms for all events is considered. For each of the considered focal mechanisms the fault plane is selected from the two nodal planes as the plane with the lowest stability, based on a Mohr-Coulomb criterion, and the misfit α is computed for the selected fault plane. Then the focal mechanism that best fits the tested stress tensor is chosen for each event, and the misfits for all events are added into a final misfit for the tested stress tensor. When the entire grid has been searched, the confidence limits of the best fitting stress tensor are computed, using statistics for one-norm misfits [*Parker and McNutt*, 1980]. Finally, the directions of greatest and least compressive horizontal stress are computed from the optimal stress tensor [*Lund and Townend*, 2007]. We refer to the stress state leading to strike-slip faulting as strike-slip stress and similarly for the other stress states.

5.2. Large-Scale Stress Inversions

[33] As a first approach we estimate the stress tensors for the seven spatial subsets defined in Figure 3. The amplitude correlation reduces the number of earthquakes in the catalogue by 30–50%, indicating many closely spaced events with similar focal mechanisms. The largest reductions are in subsets 4 and 5 in the Krísuvík area, where the summer 1999 swarm and the 2003 main shock–aftershock sequence make up a large fraction of the events in the catalogue. Note that the subsets include all events in each area during the time of 1997–2006, that is, both background seismicity and earthquake sequences are included in these inversions.

[34] The stress tensor inversion for the seven spatial subsets yields well-constrained principal stress directions and R values, with small confidence regions (Figures 7b and 7c). The most remarkable feature of the stress inversions is the stable directions of σ_3, and thus stable directions of greatest compressive horizontal stress (S_{Hmax}), as shown with the histograms at the periphery of each stress tensor. The σ_3 are close to horizontal trending ESE-WNW for all the subsets, with a tendency for a small clockwise rotation as we move from west to east. The western RP (subset 1) has a normal stress state, with some obliquity toward strike slip. The western Fagradalsfjall area (subset 2) has a stress state that appears to be both strike slip and normal, indicating that the range of strike-slip and normal mechanisms do not uniquely identify the causative state of stress, or that the events are generated in two different stress fields, in different areas. The eastern Fagradalsfjall area (subset 3) has a stress state that is mostly strike slip. The Krísuvík area (subsets 4–6) has oblique strike-slip stress states, with the optimal σ_1 plunging around 30° toward SW. The R values in Krísuvík are higher than in Fagradalsfjall, showing that the magnitudes of σ_2 and σ_3 are more similar, which is also reflected in the large uncertainty as to the plunge of σ_3 in the eastern Krísuvík subset (subset 6). The eastern RP (subset 7) has an oblique strike-slip stress state, with relatively large confidence regions. The subset covers a much larger area with less frequent seismicity than in Fagradalsfjall and Krísuvík, and the actual stress state may not be homogeneous.

[35] The estimated R values are generally high (i.e., $\sigma_2 \approx \sigma_3$), indicating a tendency toward reverse stress in the primarily strike-slip stress state. This tendency is most pronounced in the Krísuvík area. The R value estimated from stress tensor inversion is often poorly constrained [*Gephart*, 1990], but our results may reflect the fact that some of the events we include have reverse mechanisms, as discussed in section 4. However, the estimated stress tensors show a consistent regional trend with generally very stable subhorizontal σ_3, indicating a strike-slip to normal faulting stress state.

[36] The fault planes that were selected from the nodal planes of the focal mechanisms during the stress inversion show some variation but are mainly steep NE-SW to N-S planes (Figure 7d), in general agreement with the mapped

surface fractures on the RP [*Clifton and Kattenhorn*, 2006]. The western RP (subset 1) and the western Fagradalsfjall (subset 2) have N-S to NE-SW fault planes, dipping 50–90° to either side. The relatively shallow fault planes in these areas are consistent with a larger proportion of normal faulting mechanisms. The eastern Fagradalsfjall (subset 3) has similar fault orientations, but generally steeper planes. The Krísuvík area (subsets 4–6) mainly has steep NE-SW faults, with fewer N-S faults than in Fagradalsfjall. The eastern RP (subset 7) has a large variation in selected fault plane orientations, and includes a considerable amount of E-W fault planes in addition to NE-SW and N-S faults. Hence, we see a small clockwise rotation of the selected fault planes from west to east, consistent with the rotation of the $S_{H\max}$ directions from the estimated stress tensors. We note that the instability criterion in the stress inversion scheme by *Lund and Slunga* [1999] tends to select the fault planes that agree best with the geological structures.

[37] In addition to the stress inversions described above, we estimate the stress states for different subsets in time to examine if we can detect any temporal variations in the stress field. We separate out the 1998 and 2004 swarms in Fagradalsfjall and the 1999 swarm and 2003 main shock–aftershock sequence in Krísuvík and compare their causative stress states to the stress of the background seismicity. We find that the episodic swarms and sequences in both areas have quite similar stress states as that established by the background seismicity. Finally, we perform some stress tensor inversions in order to examine if we can detect any changes in the stress state following the $M_W \geq 5$ earthquakes in the Krísuvík area on 17 June 2000 and 23 August 2003, but the estimated stress tensors show no temporal variations that are significant above the uncertainty levels.

5.3. Mapping the Direction of Least Compressive Horizontal Stress

[38] We perform stress tensor inversions on smaller spatial subsets in order to investigate the spatial variations in the direction of stress along the Reykjanes Peninsula. We choose to show the direction of least compressive horizontal stress, $S_{h\min}$, as we have shown that the direction of σ_3 is stable and as this parameter is appropriate to use when describing the state of stress at a divergent plate boundary. The directions of least compressive horizontal stress are used in section 6 for a comparison with geodetic strain rates derived from GPS velocities estimated from data spanning July 2000 to April 2006; hence, we only use earthquake data from the same period in these stress inversions. We use the k means clustering algorithm to divide the earthquake catalogue into clusters of at least 30 events after the amplitude correlation. This yields 32 clusters, with an average of 80 events per cluster on the central RP and 40 events per cluster on the western and eastern RP.

[39] The estimated $S_{h\min}$ directions are shown in Figure 8a. The confidence intervals for these inversions are larger than for our large-scale inversions in section 5.2, since we have fewer events in the groups and thus less averaging. We estimate that the individual $S_{h\min}$ directions have an associated 1σ uncertainty of 10–15°, although there are inherent problems in quantifying the uncertainty (see discussions of *Lund and Slunga* [1999] and *Hardebeck and Hauksson*

[2001]). Despite the larger uncertainty on individual inversions, the estimated $S_{h\min}$ directions trend very consistently ESE along the peninsula, with an average of N(120 ± 6)°E. The uncertainty we state here is the 1σ standard deviation of the circular mean of the estimated directions; hence, it only reflects the dispersion of the estimated $S_{h\min}$ directions, not the uncertainties on individual direction estimates. The obtained stress states are mostly strike slip, with some normal stress states. Many of the inversions result in tensors that do not have a vertical principal stress axis. However, all but very few of the estimated stress tensors have σ_3 close to horizontal. This, together with the consistent directions of $S_{h\min}$ supports the notion that σ_3 is stable, and that the estimated stress tensors are robust despite the large variation of the included focal mechanisms.

6. Stress, Strain, and Plate Spreading

6.1. Comparison of Stress and Strain Rate Directions

[40] We compare the $S_{h\min}$ directions from the stress tensor inversions in section 5 with geodetic strain rate directions, derived from GPS velocities. The GPS velocities are based on annual surveys of a dense campaign network on the Reykjanes Peninsula during 2000–2006 [*Keiding et al.*, 2008]. The strain rates are computed by interpolating the velocities onto a rectangular grid and taking the derivatives at the center of each grid cell, using the method of *Haines et al.* [1998] and *Beavan and Haines* [2001]. The 23 August 2003 M_W5.0 earthquake in the Krísuvík area caused horizontal coseismic offsets of up to 1 cm on nearby GPS stations. A discontinuity of the velocity field prevents a reliable estimation of its derivative; hence, we correct the velocities for the estimated coseismic offsets, before computing the strain rates [see *Keiding et al.*, 2008].

[41] The horizontal strain rates derived from the GPS velocities are shown in Figure 8b. The arrows show the greatest extensional ($\dot{\epsilon}_{H\max}$) and contractional ($\dot{\epsilon}_{h\min}$) horizontal strain rates, and the contours in the background show the magnitude of the maximum shear strain rate, $\frac{1}{2}(\dot{\epsilon}_{H\max} - \dot{\epsilon}_{h\min})$. High shear strain rates are observed on the central RP, corresponding closely to the areas of high seismicity. The western RP also has high shear strain rates, in addition to considerable variation in both magnitudes and directions of the principal strain rates. These variations are at least partly due to the subsidence around the Svartsengi geothermal power plant, which causes both areal contraction and shear in the horizontal strain rate field [*Keiding et al.*, 2008].

[42] We compare the directions of $S_{h\min}$ from the stress inversions with the directions of $\dot{\epsilon}_{H\max}$ from the interpolated strain rate field (Figure 8c). For each $S_{h\min}$ direction we compute the equivalent $\dot{\epsilon}_{H\max}$ direction as the average of the four nearest grid points, weighted by distance. The differences between individual stress and strain rate directions are generally small and varying in an unsystematic manner. A comparison of the average $S_{h\min}$ and $\dot{\epsilon}_{H\max}$ directions shows an excellent agreement. The $\dot{\epsilon}_{H\max}$ directions used in the comparison average N(121 ± 3)°E (1σ standard deviation of the circular mean), very close to the average $S_{h\min}$ directions of N(120 ± 6)°E.
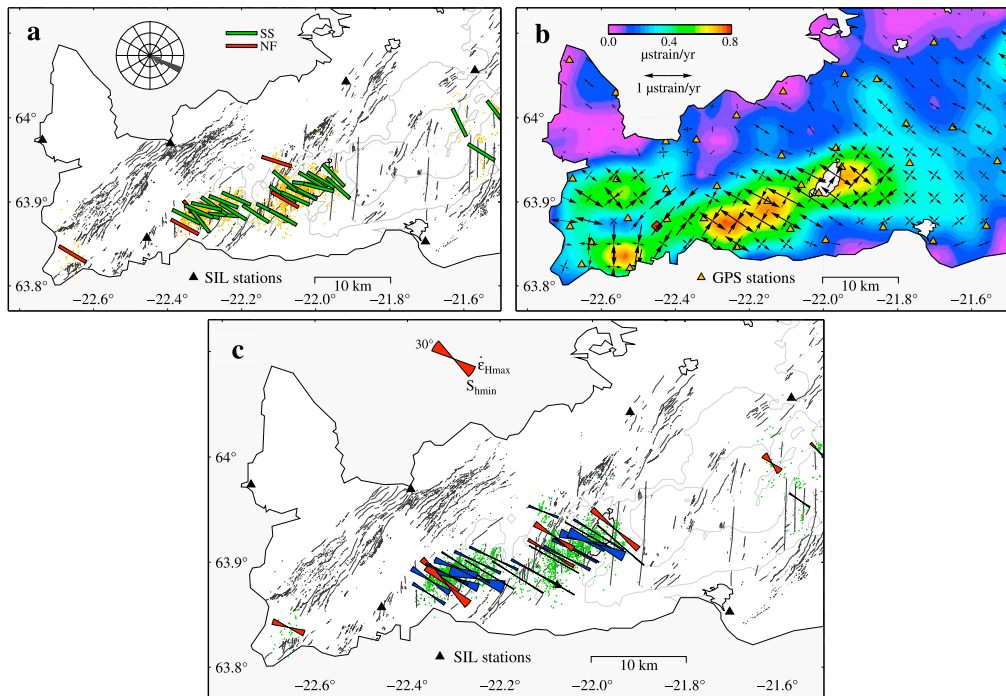
Figure 8. (a) Estimated directions of S_{hmin} from stress inversions of earthquake focal mechanisms from July 2000 to April 2006, in 32 clusters with at least 30 events after amplitude correlation. The bars are colored according to stress state: strike slip (green) and normal (red). Yellow dots show the earthquakes that were included in the inversions. The inset rose diagram shows the directions of S_{hmin} in $10°$ bins. (b) Geodetic strain rates computed from 2000–2006 GPS velocities. The greatest extensional ($\dot{\epsilon}_{Hmax}$) and contractional ($\dot{\epsilon}_{hmin}$) horizontal strain rates are shown with the arrows, while the magnitude of the maximum horizontal shear strain rate, $\frac{1}{2}(\dot{\epsilon}_{Hmax} - \dot{\epsilon}_{hmin})$, is shown by the contours. The locations of GPS stations are shown as the orange triangles, and the location of the Svartsengi geothermal power plant is shown by the red diamond. (c) Comparison of the S_{hmin} directions in Figure 8a and the $\dot{\epsilon}_{Hmax}$ directions in Figure 8b. The bow ties show the differences between the orientations of S_{hmin} and $\dot{\epsilon}_{Hmax}$, with the radii scaled to the magnitudes of the maximum shear strain rate and fill colors indicating whether S_{hmin} is oriented clockwise (red) or counterclockwise (blue) to $\dot{\epsilon}_{Hmax}$. Green dots are earthquakes.

6.2. Stress due to Plate Spreading

[43] We evaluate the stress directions predicted by the kinematic plate boundary model that *Keiding et al.* [2008] derived from the 2000–2006 GPS velocity field on the Reykjanes Peninsula. The plate boundary is approximated using vertical dislocations with both left-lateral motion and opening, as described in section 3.3. Two segments are defined, one for the main part of the peninsula and one for the westernmost part, due to the apparent bend of the plate boundary on the western RP. *Keiding et al.* [2008] modelled the subsidence around the Svartsengi geothermal power plant using a contracting pressure source [*Mogi*, 1958] at 5 km depth. Although the Mogi source model has been applied to explain subsidence due to fluid extraction in geothermal areas [e.g., *Mossop and Segall*, 1997; *Vadon and Sigmundsson*, 1997], a pressure source in an elastic half-space may not be an appropriate description of the

physical processes occurring at depth due to the fluid extraction. In addition, the stress changes predicted by a contracting pressure source are very large when evaluated close to the source, and the stresses become infinite at the source location. We therefore do not include the Mogi point source in our stress calculations. Solving the more appropriate poroelastic problem to evaluate stress changes due to the contraction and subsidence at Svartsengi is outside the scope of the present study. Very few earthquakes occurred in the geothermal field, and the nearest stress data are from the relatively deep earthquakes in the Fagradalsfjall area; hence, they are most likely not affected by the shallow pressure changes in Svartsengi.

[44] From the plate boundary model we estimate the stress field on a rectangular grid at 4 km depth, and compute the direction of least compressive horizontal stress, S_{hmin}, from the stress tensor at each grid point. Figure 9a shows
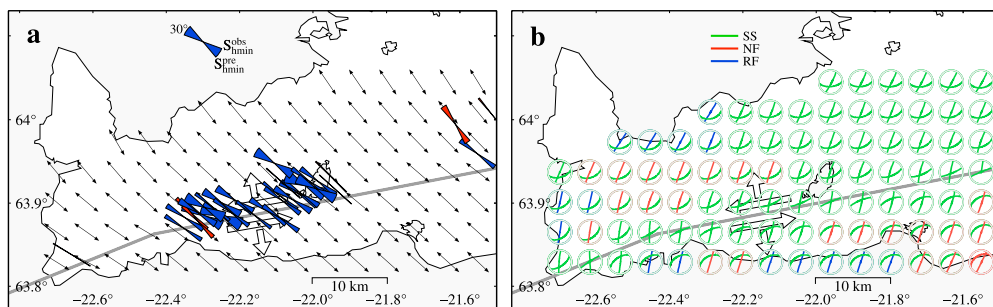
Figure 9. Predicted stresses and fault orientations from a kinematic plate boundary model derived from GPS velocities from 2000 to 2006 [*Keiding et al.*, 2008]. The grey lines show the model dislocations, and the white arrows in the background indicate the 18 ± 2 mm/a left-lateral motion and 7 ± 1 mm/a opening along the main RP dislocation. (a) Predicted directions of least compressive horizontal stress at 4 km depth (thin black arrows). The bow ties show a comparison with the observed directions of S_{hmin} estimated from earthquake data (see Figure 8a), with fill colors indicating whether the observed S_{hmin} is oriented clockwise (red) or counterclockwise (blue) to the predicted direction. (b) Optimal fault plane orientations at 4 km depth. The two conjugate fault planes are shown in lower hemisphere projections and colored according to faulting type: strike-slip faulting (green), normal faulting (red), and reverse faulting (blue).

the predicted S_{hmin} directions and a comparison with the stress directions inferred from the inversions of microearthquake focal mechanisms. The differences between the observed and predicted S_{hmin} directions are generally small and within the uncertainties of the estimated stress directions. However, most of the observed stresses are oriented at a small angle counterclockwise to the spreading directions (the blue bow ties in Figure 9a), and the systematic discrepancy indicates that our kinematic model does not quite capture the observed deformation. The predicted S_{hmin} directions used in the comparison average $N(132 \pm 1)°E$.

[45] We also examine which fault orientations are most likely to fail given the tectonic loading in the kinematic plate boundary model (Figure 9b). We use the predicted stress field at 4 km depth to compute the optimally oriented conjugate fault planes, using simple Coulomb failure theory and assuming a friction coefficient of $\mu = 0.6$ which orients the two conjugate fault planes at $30°$ from σ_1. Near the dislocations, the fault planes are mainly N-S right lateral and NE-SW left lateral, while normal or reverse faulting on NNE-SSW faults typically is predicted at some distance from the dislocations.

7. Discussion

7.1. Seismicity Pattern

[46] Our review of the seismicity during 1926–2006 shows a systematic change in the pattern of seismicity along the Reykjanes Peninsula, from a predominance of earthquake swarms in the west to main shock–aftershock sequences in the east, in agreement with the conclusions of previous studies [*Tryggvason*, 1973; *Einarsson*, 1991]. The change in seismicity pattern follows the change from primarily normal stress state in the west to oblique strike-slip stress in the east, revealed by our stress inversions, as well as the decrease of the observed b values from west to

east. A change in the structural style is apparent from the distribution of fissure swarms along the RP, as the eruptive fissures become focused into narrower zones moving eastward along the peninsula (A. Clifton, personal communication, 2008). These changes in the seismicity, stress, and structural style most likely reflect the transition from the seafloor spreading along the Reykjanes Ridge to transform motion in the South Iceland Seismic Zone.

[47] On the basis of five months of microearthquake data from the Krísuvík and Fagradalsfjall areas, *Geoffroy and Dorbath* [2008] proposed that the plate boundary in the area resembles a transtensional segmented transform, consisting of N60°E trending fracture zones in the Fagradalsfjall and Krísuvík areas, connected by an E-W trending transform. We find that our 10 years of microearthquake data, albeit not relatively relocated, as well as the relocations of *Hjaltadóttir and Vogfjörd* [2005, 2006], show that although the Fagradalsfjall activity is elongated in a general ENE trend toward Krísuvík, it does neither seem to occur on a well defined N60°E segment nor define a separate E-W segment. The Krísuvík seismicity is widely distributed and contains large magnitude earthquakes on N-S trending faults.

[48] We do not find a correlation between areas of low V_p/V_s ratios, interpreted as zones of increased fluid temperature and pressure [*Geoffroy and Dorbath*, 2008] and high b values. On the contrary, the b values in Krísuvík and westernmost Fagradalsfjall are all less than 1. This is an intriguing observation as high fluid pressures and temperatures often are considered to be associated with higher b values than the normal "tectonic" b value close to 1 [e.g., *Wyss*, 1973].

[49] Another point of interest is the current seismic quiescence in the Svartsengi geothermal field. A drawdown of more than 2 MPa in the Svartsengi field since the start of the geothermal fluid extraction in 1976 may have raised the

fracture limit and thus reduced the microearthquake activity temporarily [*Brandsdóttir et al.*, 2002]. Only few and small earthquakes have been reported in the area since the 1970s (see Figure 2). Unless there is significant aseismic movement in the area, the current tectonic loading and low seismicity could have implications for the seismic hazard of the area.

7.2. Directions of Stress and Strain Rates

[50] Our comparison of the directions of stress and strain rate show that the crust on the Reykjanes Peninsula is extending in the direction of least compression. This is the expected result for the perfectly elastic case, if the deformation processes causing the earthquakes and the geodetically determined surface deformation are the same. It is important to note that we compare stresses at depth with strain rates observed at the surface; hence, we may expect some differences if there is a depth dependence of the processes causing the stress and strain rate fields. However, the excellent agreement between the observed stress and strain rate directions, as well as the close agreement between the observed stress directions and the stress directions predicted by the kinematic plate boundary model, indicate that the stresses that drive the earthquakes are controlled by plate motion. The normal to low *b* values we observe on the RP support the notion that the geothermal fields do not control the earthquake activity. They also indicate that the stress in the crust is relatively high.

[51] We noted in section 3.2 that the seismicity rates in Krísuvík and Fagradalsfjall during 1997–2006 are very different. The close spatial relationship between the area of high seismicity, the geothermal field and a low Vp/Vs ratio anomaly in Krísuvík, suggests that the geothermal activity probably influences the seismicity in this area. However, the results of this study indicate that the role of the geothermal fluids is probably more as a trigger of the seismicity than as the driving mechanism. There is no geothermal alteration manifest at the surface in the Fagradalsfjall area, and it is not known if there are particular triggering mechanisms behind the pronounced swarm activity in this area. Earthquake swarms are often related to magmatic injections [e.g., *Hill*, 1977], but there are no indications of current magmatic activity in the Fagradalsfjall area or elsewhere on the peninsula. We therefore conclude that both main shock–aftershock sequences and earthquake swarms on the Reykjanes Peninsula occur as a result of the tectonic loading, probably with geothermal fluid triggering effects in the Krísuvík area.

[52] The results of our study differ from the results of *Townend and Zoback* [2006], who found that the geodetic strain rates in central Japan are caused by both subduction thrusts and mountain-building processes, while the stresses obtained from intraplate earthquakes reflect only the latter. In the case of the Reykjanes Peninsula, on the other hand, the spreading between North America and Eurasia appears to control both the stresses at depth and the strain rates observed at the surface.

[53] There are some indications of a small rotation of the strain rate directions within the most active part of the plate boundary zone, that is, in the areas of high shear strain rates and high seismicity around Fagradalsfjall and Krísuvík. The strain rates in Figure 8b have an average regional $\dot{\epsilon}_{H\max}$

direction of N(130 ± 8)°E for all data points east of 22.4°W where the strain rate field gets perturbed due to the subsidence around the Svartsengi power plant. However, the strain rates in the areas of high shear strain rates on the central RP show a slightly different orientation closer to N120°E, thus yielding a very close agreement with the estimated $S_{h\min}$ directions. The kinematic model of *Keiding et al.* [2008], which is derived from the regional GPS velocity field, predicts consistent directions of greatest extensional strain rates around N130°E. Hence, the model provides a good fit to the regional strain rate directions, but fails to reproduce the ∼10° counterclockwise rotation within the areas of high shear strain rates. The stress observations are primarily available from the central part of the peninsula, and it is therefore not possible to evaluate if there is a similar difference between the regional $S_{h\min}$ direction and the directions estimated within the areas of high seismicity. However, such rotation of the stress directions within the most active part of the plate boundary zone would explain the systematic discrepancy we observe between the estimated $S_{h\min}$ directions and the model predictions (see Figure 9a). A regional $\dot{\epsilon}_{H\max}$ direction of N130°E is confirmed by analogue clay models of oblique rifting [*Withjack and Jamison*, 1986; *Clifton and Schlische*, 2001]. Detailed structural analysis of the fractures on the RP has shown a difference in fracture strike along the margins and the center of the plate boundary zone [*Clifton and Schlische*, 2003; *Clifton and Kattenhorn*, 2006], consistent with the small rotation observed in our geodetic strain rate directions. Numerical modeling of oblique rifting [e.g., *Tuckwell et al.*, 1998] indicates that this change in direction is caused by a transition from stronger crust on the margins of the plate boundary zone to weaker crust in its central part. These observations suggest additional complexity in the spatial strain rate distribution that is not captured by the simple plate boundary model from *Keiding et al.* [2008].

7.3. Inferred Fault Plane Orientations

[54] We compare the selected fault planes from the stress inversions with fractures that have been mapped at the surface and by relative earthquake relocation, as well as model predictions. The selected NE-SW to N-S trending fault planes are in general agreement with the mapped surface fractures on the RP [*Clifton and Kattenhorn*, 2006] (see Figure 1). However, a large proportion of the mapped fractures are NE-SW trending normal faults that are located within the volcanic fissure swarms and were probably formed under the influence of a different stress field during periods of magmatic activity. Detailed constraints on the faults that were seismically active during 1997–2006 in the Fagradalsfjall area are provided by a relative earthquake relocation study by *Hjaltadóttir and Vogfjörd* [2006]. They mapped 29 faults of which most were N-S right-lateral faults (18 faults), and the rest were NE-SW left-lateral faults (6 faults), or NNE-SSW normal faults (5 faults). The most prominent of the faults mapped by *Hjaltadóttir and Vogfjörd* [2006] is a 4 km long N42°E left-lateral fault that was activated during both the 1998 and the 2004 swarms. Results of our kinematic plate boundary model and clay model experiments of oblique rifting [*Withjack and Jamison*, 1986; *Clifton and Schlische*, 2001] are in general agreement with the faults mapped by relative relocation.

[55] The Fagradalsfjall area has a relatively large proportion of N-S trending selected fault planes, in good agreement with the faults mapped by relative earthquake relocation [*Hjaltadóttir and Vogfjörd*, 2006]. The Krísuvík area, on the other hand, has fewer N-S planes among the selected fault planes. This may reflect the fact that the Krísuvík area is located in the center of a large fissure swarm with many NE-SW trending normal faults, and that the geothermal activity in the area trigger some slip on the preexisting normal faults rather than producing a set of optimally oriented faults.

8. Conclusions

[56] We have examined the seismicity and the state of stress along the obliquely divergent Reykjanes Peninsula plate boundary and compared the directions of stress from earthquake focal mechanisms to the directions of strain rates observed at the surface by GPS.

[57] The seismicity on the peninsula since early instrumental earthquake recordings in 1926 shows a systematic change from a predominance of earthquake swarms in the west to main shock–aftershock sequences in the east, reflecting the transition from the seafloor spreading along the Reykjanes Ridge to transform motion in the South Iceland Seismic Zone. We find a reasonable agreement between the seismic moment released by $M_L \geq 4$ earthquakes during 1926–2006 and the estimated moment accumulation from plate motion. During 1997–2006 most earthquakes on the Reykjanes Peninsula were located in two areas, Fagradalsfjall and Krísuvík on the central RP. Pronounced swarm activity was observed in both areas, as well as moderate main shocks in the Krísuvík area.

[58] We investigate the state of stress inferred from inversion of microearthquake focal mechanisms from the SIL seismic catalogue, from 1997–2006. The state of stress is mostly strike slip, with a predominance of normal stress state on the western part of the peninsula. The selected fault planes from the stress inversions are mainly steep NE-SW and N-S striking planes, in general agreement with mapped faults and model predictions. The directions of least compressive horizontal stress ($S_{h\mathrm{min}}$) were mapped in detail and compared to the directions of greatest extensional strain rate ($\dot{\epsilon}_{H\mathrm{max}}$), derived from GPS velocities spanning 2000–2006. The $S_{h\mathrm{min}}$ directions trend consistently ESE with an average of N(120 $\pm$ 6)°E, in excellent agreement with the $\dot{\epsilon}_{H\mathrm{max}}$ directions, which average N(121 $\pm$ 3)°E in the areas with earthquakes and stress data. The excellent agreement between the observed stress and strain rate directions indicate that the stresses driving the seismicity are controlled by the plate motion. Geothermal fluids may, however, act as a secondary triggering mechanism of the seismicity in the Krísuvík area, but this is less likely in the Fagradalsfjall area where no geothermal activity is observed at the surface.

References

Angelier, J. (1979), Determination of the mean principal directions of stresses for a given fault population, *Tectonophysics*, *56*, T17–T26, doi:10.1016/0040-1951(79)90081-7.

Antonioli, A., M. E. Belardinelli, A. Bizzarri, and K. S. Vogfjörd (2006), Evidence of instantaneous dynamic triggering during the seismic sequence of year 2000 in south Iceland, *J. Geophys. Res.*, *111*, B03302, doi:10.1029/2005JB003935.

Árnadóttir, T., H. Geirsson, and P. Einarsson (2004), Coseismic stress changes and crustal deformation on the Reykjanes Peninsula due to triggered earthquakes on 17 June 2000, *J. Geophys. Res.*, *109*, B09307, doi:10.1029/2004JB003130.

Árnadóttir, T., W. Jiang, K. L. Feigl, H. Geirsson, and E. Sturkell (2006), Kinematic models of plate boundary deformation in southwest Iceland derived from GPS observations, *J. Geophys. Res.*, *111*, B07402, doi:10.1029/2005JB003907.

Arnott, S. K., and G. R. Foulger (1994), The Krafla spreading segment, Iceland: 1. Three-dimensional crustal structure and the spatial and temporal distribution of local earthquakes, *J. Geophys. Res.*, *99*(B12), 23,801–23,825, doi:10.1029/94JB01465.

Båth, M. (1973), *Introduction to Seismology*, Birkhauser, Basel, Switzerland.

Beavan, J., and J. Haines (2001), Contemporary horizontal velocity and strain rate fields of the Pacific-Australian plate boundary zone through New Zealand, *J. Geophys. Res.*, *106*(B1), 741–770, doi:10.1029/2000JB900302.

Becker, T. W., J. L. Hardebeck, and G. Anderson (2005), Constraints on fault slip rates of the southern California plate boundary from GPS velocity and stress inversions, *Geophys. J. Int.*, *160*, 634–650, doi:10.1111/j.1365-246X.2004.02528.x.

Bödvarsson, R., S. T. Rögnvaldsson, R. Slunga, and E. Kjartansson (1999), The SIL data acquisition system-At present and beyond year 2000, *Phys. Earth Planet. Inter.*, *113*, 89–101, doi:10.1016/S0031-9201(99)00032-1.

Bohnhoff, M., H. Grosser, and G. Dresen (2006), Strain partitioning and stress rotation at the North Anatolian fault zone from aftershock focal mechanisms of the 1999 Izmit M_W = 7.4 earthquake, *Geophys. J. Int.*, *166*, 373–385, doi:10.1111/j.1365-246X.2006.03027.x.

Bott, M. H. P. (1959), The mechanics of oblique slip faulting, *Geol. Mag.*, *96*(2), 109–117, doi:10.1017/S0016756800059987.

Brander, J. L., R. G. Mason, and R. W. Calvert (1976), Precise distance measurements in Iceland, *Tectonophysics*, *31*, 193–206, doi:10.1016/0040-1951(76)90119-0.

Brandsdóttir, B., H. Franzson, P. Einarsson, K. Árnason, and H. Kristmannsdóttir (2002), Seismic monitoring during an injection experiment in the Svartsengi geothermal field, Iceland, *Joekull*, *51*, 43–52.

Castellaro, S., F. Mulargia, and Y. Y. Kagan (2006), Regression problems for magnitudes, *Geophys. J. Int.*, *165*, 913–930, doi:10.1111/j.1365-246X.2006.02955.x.

Clifton, A. E., and S. A. Kattenhorn (2006), Structural architecture of a highly oblique divergent plate boundary segment, *Tectonophysics*, *419*, 27–40, doi:10.1016/j.tecto.2006.03.016.

Clifton, A. E., and R. W. Schlische (2001), Nucleation, growth, and linkage of faults in oblique rift zones: Results from experimental clay models and implications for maximum fault size, *Geology*, *29*(5), 455–458, doi:10.1130/0091-7613(2001)029<0455:NGALOF>2.0.CO;2.

Clifton, A. E., and R. W. Schlische (2003), Fracture populations on the Reykjanes Peninsula, Iceland: Comparison with experimental clay models of oblique rifting, *J. Geophys. Res.*, *108*(B2), 2074, doi:10.1029/2001JB000635.

Delescluse, M., and N. Chamot-Rooke (2007), Instantaneous deformation and kinematics of the India-Australia Plate, *Geophys. J. Int.*, *168*, 818–842, doi:10.1111/j.1365-246X.2006.03181.x.

DeMets, C., R. G. Gordon, D. F. Argus, and S. Stein (1994), Effect of recent revisions to the geomagnetic reversal time scale on estimates of current plate motions, *Geophys. Res. Lett.*, *21*(20), 2191–2194, doi:10.1029/94GL02118.

Einarsson, P. (1991), Earthquakes and present-day tectonism in Iceland, *Tectonophysics*, *189*, 261–279, doi:10.1016/0040-1951(91)90501-I.

Erlendsson, P., and P. Einarsson (1996), The Hvalhnúkur fault, a strike-slip fault mapped within the Reykjanes Peninsula oblique rift, Iceland, in *Seismology in Europe, Papers Presented at the XXV ESC General Assembly, September 9–14, 1996*, edited by B. Thorkelsson, pp. 498–505, Icelandic Meteorol. Off., Reykjavík.

Frohlich, C. (2001), Display and quantitative assessment of distributions of earthquake focal mechanisms, *Geophys. J. Int.*, *144*, 300–308, doi:10.1046/j.1365-246x.2001.00341.x.

Geoffroy, L., and C. Dorbath (2008), Deep downward fluid percolation driven by localized crust dilatation in Iceland, *Geophys. Res. Lett.*, *35*, L17302, doi:10.1029/2008GL034514.

Gephart, J. W. (1990), Stress and the direction of slip on fault planes, *Tectonics*, *9*(4), 845–858, doi:10.1029/TC009i004p00845.

Gephart, J. W., and D. W. Forsyth (1984), An improved method for determining the regional stress tensor using earthquake focal mechanism data: Application to the San Fernando earthquake sequence, *J. Geophys. Res.*, *89*(B11), 9305–9320, doi:10.1029/JB089iB11p09305.

Haines, A. J., and W. E. Holt (1993), A procedure for obtaining the complete horizontal motions within zones of distributed deformation from the inversion of strain rate data, *J. Geophys. Res.*, *98*(B7), 12,057–12,082, doi:10.1029/93JB00892.

Haines, A. J., J. A. Jackson, W. E. Holt, and D. C. Agnew (1998), Representing distributed deformation by continuous velocity fields, *Rep. 98/5*, Inst. of Geol. and Nucl. Sci., Lower Hutt, New Zealand.

Hainzl, S. (2004), Seismicity patterns of earthquake swarms due to fluid intrusion and stress triggering, *Geophys. J. Int.*, *159*, 1090–1096, doi:10.1111/j.1365-246X.2004.02463.x.

Hardebeck, J. L., and E. Hauksson (2001), Crustal stress field in southern California and its implications for fault mechanics, *J. Geophys. Res.*, *106*(B10), 21,859–21,882, doi:10.1029/2001JB000292.

Hardebeck, J. L., and A. J. Michael (2004), Stress orientations at intermediate angles to the San Andreas Fault, California, *J. Geophys. Res.*, *109*, B11303, doi:10.1029/2004JB003239.

Hartigan, J. A. (1975), *Clustering Algorithms*, 351 pp., John Wiley, New York.

Hill, D. P. (1977), A model for earthquake swarms, *J. Geophys. Res.*, *82*(8), 1347–1352, doi:10.1029/JB082i008p01347.

Hjaltadóttir, S., and K. S. Vogfjörd (2005), Subsurface fault mapping in Southwest Iceland by relative location of the June 2000 earthquakes, *Rep. 21*, Icelandic Meteor. Off., Reykjavík.

Hjaltadóttir, S., and K. S. Vogfjörd (2006), Mapping fractures in Fagradalsfjall on the Reykjanes Peninsula with micro-earthquakes (in Icelandic), *Rep. 06001*, Icelandic Meteorol. Off., Reykjavík.

Hreinsdóttir, S., P. Einarsson, and F. Sigmundsson (2001), Crustal deformation at the oblique spreading Reykjanes Peninsula, SW Iceland: GPS measurements from 1993 to 1998, *J. Geophys. Res.*, *106*(B7), 13,803–13,816, doi:10.1029/2001JB000428.

Jakobsdóttir, S. S. (2008), Seismicity in Iceland: 1994–2007, *Joekull*, *58*, 75–100.

Kanamori, H. (1977), The energy release in great earthquakes, *J. Geophys. Res.*, *82*(20), 2981–2987, doi:10.1029/JB082i020p02981.

Keiding, M., T. Árnadottir, E. Sturkell, H. Geirsson, and B. Lund (2008), Strain accumulation along an oblique plate boundary: The Reykjanes Peninsula, southwest Iceland, *Geophys. J. Int.*, *172*, 861–872, doi:10.1111/j.1365-246X.2007.03655.x.

Klein, F. W., P. Einarsson, and M. Wyss (1973), Microearthquakes on the Mid-Atlantic plate boundary on the Reykjanes Peninsula in Iceland, *J. Geophys. Res.*, *78*(23), 5084–5099, doi:10.1029/JB078i023p05084.

Klein, F. W., P. Einarsson, and M. Wyss (1977), The Reykjanes Peninsula, Iceland, earthquake swarm of September 1972 and its tectonic significance, *J. Geophys. Res.*, *82*(5), 865–888, doi:10.1029/JB082i005p00865.

Kreemer, C., W. E. Holt, and A. J. Haines (2003), An integrated global model of present-day plate motions and plate boundary deformation, *Geophys. J. Int.*, *154*, 8–34, doi:10.1046/j.1365-246X.2003.01917.x.

Lund, B., and R. Bödvarsson (2002), Correlation of microearthquake body-wave spectral amplitudes, *Bull. Seismol. Soc. Am.*, *92*(6), 2419–2433, doi:10.1785/0119990156.

Lund, B., and R. Slunga (1999), Stress tensor inversion using detailed microearthquake information and stability constraints: Application to Ölfus in southwest Iceland, *J. Geophys. Res.*, *104*(B7), 14,947–14,964, doi:10.1029/1999JB900111.

Lund, B., and J. Townend (2007), Calculating horizontal stress orientations with full or partial knowledge of the tectonic stress tensor, *Geophys. J. Int.*, *170*, 1328–1335, doi:10.1111/j.1365-246X.2007.03468.x.

Marzocchi, W., and L. Sandri (2003), A review and new insights on the estimation of the b-value and its uncertainty, *Ann. Geophys.*, *46*(6), 1271–1282.

Mogi, K. (1958), Relations between the eruptions of various volcanoes and the deformations of the ground surfaces around them, *Bull. Earthquake Res. Inst. Univ. Tokyo*, *36*, 99–134.

Mogi, K. (1962), Magnitude-frequency relation for elastic shocks accompanying fractures of various materials and some related problems in earthquakes, *Bull. Earthquake Res. Inst. Univ. Tokyo*, *40*, 831–853.

Mossop, A., and P. Segall (1997), Subsidence at The Geysers geothermal field, N. California from a comparison of GPS and leveling surveys, *Geophys. Res. Lett.*, *24*(14), 1839–1842, doi:10.1029/97GL51792.

Okada, Y. (1985), Surface deformation due to shear and tensile faults in a half-space, *Bull. Seismol. Soc. Am.*, *75*(4), 1135–1154.

Ottósson, K. (1980), Earthquakes in Iceland 1900–1929 (in Icelandic), *Sci. Rep. RH-80-05*, Sci. Inst., Univ. of Iceland, Reykjavík.

Pagli, C., R. Pedersen, F. Sigmundsson, and K. L. Feigl (2003), Triggered fault slip on June 17, 2000 on the Reykjanes Peninsula, SW-Iceland captured by radar interferometry, *Geophys. Res. Lett.*, *30*(6), 1273, doi:10.1029/2002GL015310.

Parker, R. L., and M. K. McNutt (1980), Statistics for the one-norm misfit measure, *J. Geophys. Res.*, *85*(B8), 4429–4430, doi:10.1029/JB085iB08p04429.

Riedel, C., T. Petersen, F. Theilen, and S. Neben (2003), High b-values in the leaky segment of the Tjörnes Fracture Zone north of Iceland: Are they evidence for shallow magmatic heat sources?, *J. Volcanol. Geotherm. Res.*, *128*, 15–29, doi:10.1016/S0377-0273(03)00244-0.

Rögnvaldsson, S. T., and R. Slunga (1993), Routine fault plane solutions for local networks: A test with synthetic data, *Bull. Seismol. Soc. Am.*, *83*(4), 1232–1247.

Roman, D. C., S. C. Moran, J. A. Power, and K. V. Cashman (2004), Temporal and spatial variation of local stress fields before and after the 1992 eruptions of Crater Peak vent, Mount Spurr volcano, Alaska, *Bull. Seismol. Soc. Am.*, *94*(6), 2366–2379, doi:10.1785/0120030259.

Sæmundsson, K. (1978), Fissure swarms and central volcanoes of the neovolcanic zones of Iceland, *Geol. J.*, *10*, special issue, 415–432.

Scholz, C. H. (1968), The frequency-magnitude relation of microfracturing in rock and its relation to earthquakes, *Bull. Seismol. Soc. Am.*, *58*(1), 399–415.

Schultz, R. A. (1995), Limits on strength and deformation properties of jointed basaltic rock masses, *Rock Mech. Rock Eng.*, *28*(1), 1–15, doi:10.1007/BF01024770.

Scordilis, E. M. (2006), Empirical global relations converting M_S and m_b to moment magnitude, *J. Seismol.*, *10*, 225–236, doi:10.1007/s10950-006-9012-4.

Sella, G. F., T. H. Dixon, and A. Mao (2002), REVEL: A model for Recent plate velocities from space geodesy, *J. Geophys. Res.*, *107*(B4), 2081, doi:10.1029/2000JB000033.

Slunga, R. (1991), The Baltic shield earthquakes, *Tectonophysics*, *189*(1–4), 323–331, doi:10.1016/0040-1951(91)90505-M.

Sudhaus, H., and S. Jónsson (2009), Improved source modeling through combined use of InSAR and GPS under consideration of correlated data errors: Application to the June 2000 Kleifarvatn earthquake, Iceland, *Geophys. J. Int.*, *176*, 389–404, doi:10.1111/j.1365-246X.2008.03989.x.

Townend, J., and M. D. Zoback (2004), Regional tectonic stress near the San Andreas fault in central and southern California, *Geophys. Res. Lett.*, *31*, L15S11, doi:10.1029/2003GL018918.

Townend, J., and M. D. Zoback (2006), Stress, strain, and mountain building in central Japan, *J. Geophys. Res.*, *111*, B03411, doi:10.1029/2005JB003759.

Tryggvason, A., S. T. Rögnvaldsson, and Ó. G. Flóvenz (2002), Three-dimensional imaging of the P- and S-wave velocity structure and earthquake locations beneath Southwest Iceland, *Geophys. J. Int.*, *151*, 848–866, doi:10.1046/j.1365-246X.2002.01812.x.

Tryggvason, E. (1973), Seismicity, earthquake swarms, and plate boundaries in the Iceland region, *Bull. Seismol. Soc. Am.*, *63*(4), 1327–1348.

Tryggvason, E. (1978a), Earthquakes in Iceland 1930-1939 (in Icelandic), *Rep. RH-78-21*, Sci. Inst., Univ. of Iceland, Reykjavík.

Tryggvason, E. (1978b), Earthquakes in Iceland 1940-1949 (in Icelandic), *Rep. RH-78-22*, Sci. Inst., Univ. of Iceland, Reykjavík.

Tryggvason, E. (1979), Earthquakes in Iceland 1950–1959 (in Icelandic), *Rep. RH-79-06*, Sci. Inst., Univ. of Iceland, Reykjavík.

Tuckwell, G. W., J. M. Bull, and D. J. Sanderson (1998), Numerical models of faulting at oblique spreading centers, *J. Geophys. Res.*, *103*(B7), 15,473–15,482, doi:10.1029/97JB03673.

Utsu, T. (1966), A statistical significance test of the difference in b-value between two earthquake groups, *J. Phys. Earth*, *14*, 37–40.

Vadon, H., and F. Sigmundsson (1997), Crustal deformation from 1992 to 1995 at the Mid-Atlantic Ridge, southwest Iceland, mapped by satellite radar interferometry, *Science*, *275*, 194–197, doi:10.1126/science.275.5297.194.

Vogfjörd, K. S., H. Geirsson, and E. Sturkell (2004), The August 2003 earthquake swarm near Krísuvík: Fault map from aftershocks and GPS measurements, paper presented at Spring Meeting, Geosci. Soc. of Iceland, Reykjavík.

Weir, N. R. W., R. S. White, B. Brandsdóttir, P. Einarsson, H. Shimamura, H. Shiobara, and the RISE Fieldwork Team (2001), Crustal structure of the

northern Reykjanes Ridge and Reykjanes Peninsula, southwest Iceland, *J. Geophys. Res.*, *106*(B4), 6347–6368, doi:10.1029/2000JB900358.

Wessel, P., and W. H. F. Smith (1998), New, improved version of the Generic Mapping Tools released, *Eos Trans. AGU*, *79*, 579, doi:10.1029/98EO00426.

Wiemer, S., and S. R. McNutt (1997), Variations in the frequency-magnitude distribution with depth in two volcanic areas: Mount St. Helens, Washington, and Mt. Spurr, Alaska, *Geophys. Res. Lett.*, *24*(2), 189–192, doi:10.1029/96GL03779.

Withjack, M. O., and W. R. Jamison (1986), Deformation produced by oblique rifting, *Tectonophysics*, *126*, 99–124, doi:10.1016/0040-1951(86)90222-2.

Wyss, M. (1973), Towards a physical understanding of the earthquake frequency distribution, *Geophys. J. Int.*, *31*(4), 341–359, doi:10.1111/j.1365-246X.1973.tb06506.x.

————————

T. Árnadóttir and M. Keiding, Nordic Volcanological Centre, Institute of Earth Sciences, University of Iceland, Sturlugata 7, IS-101 Reykjavík, Iceland. (marie@hi.is)

B. Lund, Department of Earth Sciences, Uppsala University, Villavägen 16, SE-75236 Uppsala, Sweden.

Paper III

Keiding, M., T. Árnadóttir, S. Jónsson, J. Decriem, and A. Hooper, 2009. Plate boundary deformation and man-made subsidence around geothermal fields on the Reykjanes Peninsula, Iceland, *to be submitted to J. Volcanol. Geoth. Res.*

Plate boundary deformation and man-made subsidence around geothermal fields on the Reykjanes Peninsula, Iceland.

M. Keiding[1], T. Árnadóttir[1], S. Jónsson[2], J. Decriem[1], A. Hooper[3]

[1] Nordic Volcanological Centre, University of Iceland, marie@hi.is

[2] Division of Physical Sciences and Engineering, King Abdullah University of Science and Technology (KAUST), Saudi Arabia

[3] Delft Institute of Earth Observation and Space Systems, Delft University of Technology, The Netherlands

1 Abstract

We present Interferometric Synthetic Aperture Radar (InSAR) data from 1992–1999 and 2003–2008 as well as GPS data from 2000–2009 for the active plate boundary on the Reykjanes Peninsula, southwest Iceland. The geodetic data reveal deformation mainly due to plate spreading, anthropogenic subsidence caused by geothermal fluid extraction and, possibly, increasing pressure in a geothermal system. The installation of the Reykjanes geothermal power plant in May 2006 results in subsidence of around 10 cm during the first two years of production. We model the surface subsidence around the new power plant using point and ellipsoidal pressure sources in an elastic halfspace. Short-lived swarms of microearthquakes as well as aseismic fault movement are observed following the installation of the Reykjanes power plant, probably triggered by the stresses induced by geothermal fluid extraction.

2 Introduction

Many different natural and man-made processes associated with fluid migration at depth cause measurable deformation at the surface. The fluid-related processes are often so large that they obscure the deformation due to tectonic processes such as plate boundary deformation. Examples of processes involving fluid migration are ground-water extraction (e.g. Amelung et al., 1999; Hoffmann et al., 2001), mining (e.g. Donnelly, 2009), geothermal or hydrocarbon production (Grasso and

1

Wittlinger, 1990; Mossop and Segall, 1997; Fialko and Simons, 2000), naturally occurring fluctuations in geothermal and magmatic systems (Wicks et al., 1998; Peltier et al., 2009), or transient post-seismic processes (e.g. Jónsson et al., 2003).

Probably the most prominent example of man-maded subsidence around a geothermal reservoir is the Wairakei geothermal field in New Zealand, where 50 years of geothermal fluid extraction has resulted in a total of 15 m subsidence (Allis et al., 2009). The host rock deformation associated with geothermal fluid extraction can provide important insight in the extent, morphology and dynamics of the subsurface fluid reservoirs (e.g. Glowacka et al., 1999; Fialko and Simons, 2000; Vasco et al., 2002). The fluid flow in reservoirs is often highly anisotropic due to variations in permeability related to geological structures such as faults or sediment composition (Amelung et al., 1999), hence spatially dense observations are needed in order to fully map the resulting ground deformation. InSAR offers excellent possibilities for this. Whereas ground-based observations, such as levelling and GPS data, are usually sparse, the radar technique can provide very dense spatial sampling of the ground deformation. In one example, Fialko and Simons (2000) examined InSAR data showing the subsidence around the Coso geothermal field in California, and modelled the subsidence using multiple ellipsoidal sources in an elastic halfspace. They also showed that clusters of micro-earthquakes associated with the geothermal fluid extraction may result from perturbations in the pore fluid pressure, as well as normal and shear stresses caused by the contraction of the geothermal reservoir.

In this paper we examine the ground deformation on the Reykjanes Peninsula in southwest Iceland, using a combination of descending and ascending InSAR, as well as GPS data. The Mid-Atlantic plate boundary comes onshore on the Reykjanes Peninsula, where it forms a diffuse transtensional plate boundary zone characterised by high seismicity and recent volcanism (Figure 1). The main tectonic features on the peninsula are a large number of NE-trending eruptive fissures and fractures, grouped into four volcanic fissure swarms (Sæmundsson, 1978; Clifton and Kattenhorn, 2006). The volcanic fissure swarms are intersected by a series of N–S oriented right-lateral strike-slip faults, which are the surface expressions of the E–W shear at depth. Several high-temperature geothermal fields are present on the peninsula, located primarily at the intersections of the eruptive fissures and the strike-slip faults (Amy Clifton, personal communication, 2009). Following

the installation of a new geothermal power plant on the tip of the peninsula in 2006, a marked zone of subsidence of several cm/yr has evolved around the power plant. We examine the observed subsidence in some detail, to gain insight into the reservoir dynamics and the effect of the reservoir contraction on the surrounding crust.

3 Utilisation of geothermal energy on the Reykjanes Peninsula

The utilisation of geothermal waters has been an integral part of people's life since the settlement of Iceland in the 9'th century. The capital Reykjavík bears in its name a clear reference to geothermal springs (Reykjavík literally means "Smoky Bay"), and historical records describe how the springs were used for washing and bathing in past centuries. As of 2009, geothermal energy accounts for around 25% of the electricity production and almost all domestic heating in Iceland. Four geothermal power plants are in operation on the Reykjanes Peninsula and in the Hengill area. In 1976, the Svartsengi geothermal power plant was installed on the Reykjanes Peninsula, and since then it has been progressively expanded. The most recent expansion of Svartsengi took place in early 2008, resulting in a production capacity of 75 MW electricity and 150 MW heat. The Nesjavellir power plant was put into operation in the Hengill area in 1990, and is today the largest geothermal power plant in Iceland with a capacity of 120 MW electricity and 300 MW heat. In May 2006, the Reykjanes power plant was installed on the tip of the Reykjanes Peninsula with a capacity of 100 MW electricity. Later that year, the Hellisheidi power plant was installed in the southern Hengill area. The Hellisheidi power plant holds a production capacity of 210 MW electricity, as of February 2009, but there are plans to expand its capacity to a total of 300 MW electricity and 400 MW heat.

As the pressure drawdown may diminish the well field productivity, waste fluids are typically reinjected into the geothermal reservoirs. In Svartsengi, reinjection has been carried out at intermittent rates since 1984, but injection was increased progressively during 2002–2008 so that around 50% of the volume of extracted water was reinjected in 2008 (Vatnaskil, 2009). Systematic reinjection in the Reykjanes field has not started, as of summer 2009. In Hellisheidi, all waste

fluids from the production are reinjected into the reservoir.

The extraction of geothermal fluids results in pressure decrease and contraction of the rock matrix within the reservoir, which in turn causes subsidence above the reservoir. Subsidence in the Svartsengi field was first documented by a levelling and gravity study based on repeated measurements during 1975–1999 (Eysteinsson, 2000). The results of the levelling showed subsidence rates between 7–14 mm/yr, with the highest rates during the first years of production. The study also demonstrated that the subsidence at Svartsengi varies linearly with the pressure decrease observed at 900 meter depth in boreholes. The subsidence around Svartsengi was later confirmed by an InSAR study (Vadon and Sigmundsson, 1997), as well as GPS studies (Hreinsdóttir et al., 2001; Magnússon and Thorbergsson, 2004; Árnadóttir et al., 2006; Keiding et al., 2008).

4 Data and Methods

4.1 GPS data

We report GPS data from a network of around 60 campaign stations and 8 continuous stations on the Reykjanes Peninsula and the Hengill area. Annual surveys of selected campaign stations have been carried out since 2000. Each campaign measurement lasted at least two days during 2000–2006 and three days during 2007–2009. For this study, we processed all GPS data with the Bernese Software V5.0 (Dach et al., 2007), with orbit information from the Center for Orbit Determination in Europe. Six international IGS stations were included in the processing to aid the stabilisation in a global reference frame (Dow et al., 2005). The campaign solutions were combined and stabilised in the International Terrestrial Reference Frame (ITRF) 2005 (Altamimi et al., 2007), using the GLOBK software (Herring et al., 2006) and daily solutions for all continuous GPS stations in Iceland as well as the IGS stations. Finally, we form time series and compute station velocities in ITRF2005. We scale the formal uncertainties so that they equal the coordinate repeatabilities, which gives typical uncertainties of 1–2 mm on the north and east positions and 5–10 mm on the vertical position.

Discontinuities in the velocity field are caused by earthquakes in 2003 and 2008. On 23 August 2003 a $M_W 5.0$ earthquake occurred on the central Reykjanes Peninsula, causing horizontal offsets of up to 1 cm at eight stations (Keiding et al.,

2008). The velocities at these stations are computed using only the GPS data after the 2003 earthquake. Two main shocks with a composite magnitude of $M_W 6.2$ occurred immediately east of the study area on 29 May 2008, causing coseismic offsets of up to several cm on the eastern part of the peninsula (Hreinsdóttir et al., 2009). Hence the velocities at all stations east of 22°W are estimated using data before the 2008 earthquake sequence. Furthermore, the start of production in the Reykjanes and Hellisheidi geothermal fields in 2006 affected the velocities at nearby stations, as seen in the time series of the campaign stations RNES and HH04 in Figure 2. We therefore divide the time series at affected stations into two time periods before and after 2006, using the GPS campaign measurements in March–April 2006 as respectively the last and the first observation of each period. On average, five observations are used for the regression of constant velocities at the campaign stations. For the continuous stations we compute the velocities using observations at the time of each campaign.

4.2 InSAR data

The Reykjanes Peninsula is well suited for a radar based study because its surface mainly consists of young and sparsely vegetated lava fields, hence the surface reflectivity is sufficiently high and changes little with time. We form InSAR images from data collected by the ERS and Envisat satellites, operated by the European Space Agency. The ERS and Envisat data sets are from the descending track 138, and comprise 18 images spanning 11 May 1992–16 Sep 1999 and 22 images spanning 25 Sep 2003–18 Sep 2008, respectively. All images were acquired during May–October to avoid decorrelation due to snow. The SAR system operates with a side-looking geometry, illuminating a 100 km wide swath of the ground. The incidence angle at ground is 20–26°, and the descending line-of-sight (LOS) unit vector from ground to satellite is approximately [east north up] = [0.4 -0.1 0.9], hence the observations are most sensitive to vertical ground motion, less sensitive to east-west motion and least sensitive to north-south motion. The SAR image has ground resolution elements, or pixels, of approximately 5×20 meter.

The data are processed with the StaMPS/MTI software (Hooper et al., 2007; Hooper, 2008), which applies both a Persistent Scatterer (PS) and a Small Baseline (SB) approach. This multi-temporal InSAR method involves the processing of multiple acquisitions and addresses the problems of decorrelation caused by dif-

ferences in position and orientation of the master and slave sensor or by physical changes at the surface (e.g. Zebker and Villasenor, 1992). The PS method identifies pixels that are dominated by the echo from a single bright scatterer and therefore have little decorrelation due to changes in satellite geometry or relative movement of scatteres within the pixel. The SB method, on the other hand, minimises the decorrelation by computing interferograms with short temporal and spatial baselines. The combination of the two data sets has the potential for improving the spatial sampling considerably, and thereby increase the resolution of deformation signals and aid a more reliable phase unwrapping.

For the PS processing a master is chosen that minimises the sum of decorrelation due to the time interval, the perpendicular baseline and the difference in Doppler frequency. For the SB processing we form 42 ERS and 63 Envisat multiple-master interferograms. The Doris software (Kampes et al., 2003) is used for the interferometric processing. Each slave image is resampled to the master geometry and corrected for the difference in position of the master and slave sensor, using the WGS84 reference ellipsoid and a 25 m digital elevation model from the National Land Survey of Iceland. The pixels selected by the two methods are then combined and the phase unwrapped using a statistical cost flow algorithm applicable to single- or multiple-master time series (Hooper et al., 2009). Finally, the unwrapped phase is corrected for atmospheric delay plus errors in orbits and the elevation model, using a combination of temporal and spatial filtering (Hooper et al., 2007).

5   Results

5.1   GPS data

Figure 3 shows the GPS velocities relative to stable North America, computed using the ITRF2005 absolute rotation pole for the North American plate (Altamimi et al., 2007). The GPS velocities on the Reykjanes Peninsula mainly reflect the plate motion, that is, left-lateral shear in the E–W direction as well as some N–S opening. The station velocities are close to zero on the northern part of the peninsula, and gradually increase in magnitude moving south across the plate boundary zone. The stations along the southern shore of the peninsula are moving toward ESE with horizontal rates of 18–19 mm/yr relative to North America, or

almost the full spreading rate. The vertical GPS velocities are close to zero on the central part of the peninsula, but uplift is observed along the SE part of the peninsula. During 2001–2006 local subsidence is observed in the Svartsengi field, with a subsidence rate of 5–10 mm/yr, while no clear signal of subsidence is observed around the Nesjavellir power plant in the northern Hengill area.

During 2006–2009, marked signals of subsidence appear around the Reykjanes and Hellisheidi fields. The Reykjanes subsidence is confined to a small area on the tip of the peninsula, with a maximum subsidence rate of around 40 mm/yr at the nearest campaign GPS stations RNES (see Figure 2). The Hellisheidi subsidence bowl covers a larger area, in accordance with the larger extent of the well field. The maximum subsidence rates are smaller than in the Reykjanes field, however, the rates are not well-constrained due to the short time span of these station velocities from 2006 to 2008 (until the May 2008 earthquake). Interestingly, the station DRAU which is located less than one km from the Hellisheidi power plant (see Figure 3), has close to zero vertical rate, probably because it is located near one of the areas where waste fluids are being reinjected.

5.2   InSAR

The resulting ERS and Envisat time series each comprises around 2 million pixels, providing an exceptionally good spatial sampling of the ground deformation on the Reykjanes Peninsula. Small areas of decorrelation are observed at steep slopes and in areas with lakes or relatively dense vegetation. We compute the mean LOS velocity fields for the time periods 11 May 1992–16 Sep 1999, 25 Sep 2003–29 Sep 2005 and 6 Jul 2006–1 May 2008. Several of the ERS and Envisat interferograms have a bilinear phase ramp, showing increasing range change from east to west. The ramps may be partly due to orbital errors, but they may also reflect a regional subsidence of the western part of the peninsula, relative to its eastern part, as has been documented by a countrywide GPS study (Árnadóttir et al., 2009). In order to better display the local signals of deformation along the Reykjanes Peninsula, we remove the ramps before computing the mean LOS velocities. The 2003–2005 and 2006–2008 LOS fields have some noise, seen as areas of patchy LOS rates, reflecting that the mean LOS velocities during these periods are estimated from only nine images. The standard deviation of the mean LOS velocity for individual pixels is around 1 mm/yr for the 1992–1999 rates and 3–7 mm/yr for the 2003–

2005 and 2006–2008 rates. Although the standard deviation on individual pixels is sometimes high, the pattern of deformation is generally smooth and the signal-to-noise ratio is improved by multilooking the radar data.

The LOS velocity fields in Figure 4 reveal both regional and local deformation. All three images show increasing LOS rates moving from north to south across the peninsula, as illustrated with the profiles in the lower panel of Figure 4. This increase in LOS rates must in part reflect the increase in eastward velocities across the plate boundary zone, but it is also possible that they reflect some uplift along the SE part of the peninsula, as indicated by the GPS data. A subtle zone of negative LOS rates are observed along the central part of the peninsula during 2003–2005 and 2006–2008, with negative rates of 0–4 mm/yr relative to Reykjavík. The negative rates most likely reflect subsidence, caused by the extension across the plate boundary. The subsidence may indicate that the extension is not completely balanced by inflow of material from below, as suggested by Vadon and Sigmundsson (1997).

During 1992–1999 a marked zone of positive LOS rates is observed along the eastern margin of the image. A persistent earthquake swarm and uplift of the Hengill area was observed during 1994–1998, culminating in 1998 with two earthquake swarms including moderate sized events on the eastern part of the peninsula (Sigmundsson et al., 1997; Feigl et al., 2000; Clifton et al., 2002). The anomaly of positive LOS rates during 1992–1999 thus reflects uplift and possibly coseismic deformation or some widening of the Hengill fissure swarm, as suggested by a GPS study (Keiding et al., 2008).

The LOS velocity fields also show local deformation around the geothermal fields. Negative LOS rates are observed around the Svartsengi field in all three images. During 1992–1999, the maximum negative rates average 5 mm/yr, relative to Reykjavík, but a considerable higher negative rate of 20 mm/yr was in fact observed during 1992–1993, decreasing to 4 mm/yr after 1993. The varying subsidence rate is most likely due to changes in the reinjection of waste fluids at Svartsengi, as reinjection was taken up again in 1993, after a break during 1991–1992 (Vatnaskil, 2009). The subsidence around Svartsengi is elongated in the NE–SW direction, and includes the Eldvörp geothermal field located 5 km further SW (see Figure 1). The Eldvörp field has not yet been directly utilised, but a pressure connection between the Svartsengi and Eldvörp fields indicates that

8

fluids are also withdrawn from Eldvörp during production in Svartsengi (Eysteins-son, 2000). During 2003–2005 and 2006–2008, negative rates of around 10 mm/yr are observed in the Svartsengi field, but the subsidence signal is less localised than during 1992–1999, and part of the negative rates seems to be related to the regional zone of subsidence along the central plate boundary zone.

After 2006, a marked signal of negative LOS rates appears around the Reyk-janes geothermal field, reflecting the newly formed subsidence bowl due to geother-mal fluid extraction. The subsidence signal in the Reykjanes field shows up almost immediately after the power plant was put into operation in May 2006, and the maximum negative LOS rate during 2006–2008 is more than 30 mm/yr. Negative LOS rates are also observed around the Hellisheidi geothermal field in the east.

Finally, an anomaly of positive LOS rates is observed in the Krísuvík area on the central part of the peninsula. Local anomalies are also observed at some of the GPS stations in this area, which show accelerating uplift and SE motion during 2008–2009. The most likely explanation for this anomaly is that the geothermal system in the Krísuvík area is inflating due to overpressure. Another possibility, however, is that we are seeing the signs of a slow magmatic intrusion.

5.3   The western Reykjanes Peninsula

We examine the subsidence around the Reykjanes geothermal field on the western Reykjanes Peninsula in more detail, using a combination of the GPS and InSAR data. The GPS data show the 3-dimensional deformation but are spatially sparse, while the InSAR data have a very high spatial sampling rate but only provide a 1-dimensional observation of the ground deformation. Ascending radar data can add another 1-dimensional observation, because the ascending LOS unit vector of approximately [east north up] = [-0.4 -0.1 0.9] differs from the descending LOS unit vector. Too few ascending radar data are available to be processed using the multi-temporal StaMPS/MTI method. However, we process ascending ERS data from track 173, using the GAMMA software (Werner et al., 2000), resulting in a some high-quality two-pass interferograms. We include one such interferogram, spanning June 2005 – May 2008, in this study. For comparison with the descending data we compute the descending LOS displacement during same time period, from 13 images. As the deformation during this time period is not steady (for example, it includes a full year before the start of production in the Reykjanes field), we

9

choose to show the total displacements during the considered time period, rather than normalising them to annual rates.

The ascending and descending radar LOS fields are shown in Figures 5a and b, with displacements relative to the mean values in the NW part of the area (as shown with the box in Figure 5a). The ascending and descending displacements show a similar deformation pattern, mainly the subsidence bowls around the Reykjanes and Svartsengi geothermal fields. The Reykjanes subsidence is clearly elongated in the NE–SW direction, thus aligning with the trend of the fractures in the area. The largest subsidence is observed within an ellipse of approximately 3×5 km, but there is a NNE-ward extension to the subsidence bowl, making it slightly curved. The boundary toward NW is particularly sharp, but the boundary toward east is also quite sharp, indicating that there is little pressure connection between the Reykjanes field and the adjacent Eldvörp field. The elongation of the subsidence bowl shows that the permeability in the reservoir is highly anisotropic. The ascending radar data show a larger maximum negative displacement (∼12 cm) than the descending radar data (∼8 cm), but this is probably due to the horizontal shear along the plate boundary rather than a discrepancy in the vertical displacements, as described below.

The linear combinations of ascending and descending radar data can provide useful information on the ground deformation in form of near-vertical and approximately east-west deformation fields. In the area shown in Figure 5 the average LOS unit vectors for the ascending track 173 and descending track 138 are

$$
\begin{aligned}
\mathbf{n}_{asc} &= \begin{bmatrix} -0.32 & -0.10 & 0.94 \end{bmatrix} \\
\mathbf{n}_{des} &= \begin{bmatrix} 0.40 & -0.11 & 0.91 \end{bmatrix}
\end{aligned}
\tag{1}
$$

Addition and subtraction of the mean LOS displacements thus give the following sensitivity vectors

$$
\begin{aligned}
\mathbf{n}_{+} = \mathbf{n}_{asc} + \mathbf{n}_{des} &= \begin{bmatrix} 0.09 & -0.21 & 1.85 \end{bmatrix} \\
\mathbf{n}_{-} = \mathbf{n}_{des} - \mathbf{n}_{asc} &= \begin{bmatrix} 0.72 & -0.01 & -0.04 \end{bmatrix}
\end{aligned}
\tag{2}
$$

Hence the added LOS displacements will show near-vertical deformation and the subtracted LOS displacements will show deformation approximately in the east-west direction. After forming the linear combinations of the ascending and descending data we normalise them to the lengths of the sensitivity vectors to get the displacements in cm.

10

The near-vertical radar displacements in Figure 5c indicate that the total subsidence in the Reykjanes geothermal field is around 10 cm, during June 2005 – May 2008. Comparisons with the ascending and descending LOS data show that the maximum LOS displacements are offset by 1–2 km from the centre of subsidence in the near-vertical deformation field, because the horizontal motion is also mapped onto the LOS directions. The east-west radar displacements in Figure 5d show horizontal motion on the order of several cm toward the centre of subsidence around the Reykjanes field. Furthermore, there is a clear regional pattern showing westward displacements on the northern part of the peninsula and eastward displacements on the southern part, reflecting the left-lateral shear along the plate boundary.

In order to compare the radar and GPS data, we compute the GPS velocities during 2005–2009, scale them to the time period of the radar data to get the displacements, and project the displacements onto the radar unit vectors. The values of the projected GPS displacements are shown with the coloured circles on top of the radar displacements in Figure 5, and generally agree well with the radar data. A quantitative comparison can be obtained if we estimate the values of the radar data as the mean and standard deviation of the pixel values within a small area centred at each GPS station (here we use circular areas with 600 m diameter). Doing so, we find that the differences between the GPS and radar data are usually less than 1 cm and within the 1σ uncertainties of the data.

6   Modelling the subsidence around the Reykjanes field

6.1   Methodology

We estimate source models that may describe the subsidence around the Reykjanes and Svartsengi fields by joint optimisation of GPS and InSAR data. The simplest source model relating ground deformation to volume change at depth is an isotropic point pressure source (Mogi, 1958), defined by four parameters describing its location (latitude, longitude, depth) and volume change. The point source gives a good approximation to roughly equi-dimensional bodies undergoing uniform volume change and has been widely used to model observed deformation of active volcanoes (e.g. Lu et al., 2002; Pagli et al., 2004). The point source has also been applied to model subsidence due to geothermal fluid extraction (Mossop

11

and Segall, 1997; Fialko and Simons, 2000), although more than a single point pressure source is usually required in order to fit the spatial irregularities observed around geothermal fields.

Another common elastic halfspace source model that relates ground deformation to pressure change at depth is the finite prolate spheroidal source derived by Yang et al. (1988). The ellipsoidal source is defined by eight parameters describing its location (latitude, longitude, depth), geometry (length of semimajor and semiminor axes), orientation (strike and plunge of the semimajor axis) and uniform pressure at the ellipsoidal surface. The ellipsoidal source with its slightly more complicated finite geometry, often provides a better fit to the deformation observed around active volcanos (Pagli et al., 2004) or geothermal fields (Fialko and Simons, 2000), than does the simple point source. The pressure change, ΔP, of the ellipsoidal source can be related to its volume change, ΔV, by the expression

$$\Delta V = \frac{\Delta P}{\mu} \pi a b^2, \tag{3}$$

where μ is the shear modulus and a and b are the semimajor and semiminor axis lengths (Tiampo et al., 2000).

The ascending and descending radar LOS displacements and the GPS displacements (in east, north and vertical) are included as three separate data sets in the optimisations. The data reflect both the local deformation due to production in the Reykjanes and Svartsengi fields and the plate motion, as demonstrated in Figure 5d and described above. Thus, in order to model the subsidence around the geothermal fields, we have to estimate and subtract the background deformation due to plate motion for both GPS and radar data. For the GPS data we estimate the background velocities observed during 2001–2006 at each station, and subtract them from the velocities observed during 2005–2009. The four stations located nearest to Svartsengi are affected by the subsidence around the geothermal field during the entire period of the GPS data included in this study, hence we obtain an estimate of the background velocities due to plate motion at these stations as the average of the background velocities at nearby GPS stations. We finally scale the velocities during 2005–2009 to match the time period of the radar data. In the radar fields, the east-west shear along the plate boundary causes linear ramps perpendicular to the plate boundary, hence we estimate such ramps in areas where there is negligible subsidence (here we use data east of 22.35°W

and north of 63.96°N), and subtract them from the LOS displacements. During optimisation, we moreover estimate and subtract a constant offset in the ascending and descending radar data, as to not bias the input due to the choice of reference frame (that is, the area shown with the box in Figure 5a).

We sub-sample the radar data using a quadtree algorithm that reduces the number of data points while maintaining a good spatial representation of the deformation. We start by dividing the radar LOS fields into squares of 2×2 km, which corresponds approximately to the correlation distance within the data. The squares that have a variance larger than a certain threshold are then recursively subdivided into quadrants until the variance within each quadrant does not exceed the threshold. The weights of the sub-sampled radar data are estimated from the full data variance-covariance matrix, as described by Sudhaus and Jónsson (2008). The sample covariogram for a discrete distance class h_c is given by

$$\hat{C}(h_c) = \frac{1}{2N} \sum_{i=1}^{N} d(\mathbf{r}_i) \cdot d(\mathbf{s}_i) \tag{4}$$

where $d(\mathbf{r}_i)$ and $d(\mathbf{s}_i)$ are the radar LOS displacements at the locations $\mathbf{r}_i$ and $\mathbf{s}_i$ separated by distances of approximately h_c, and N is the number of data pairs in the distance class. The sample covariogram is fitted by an exponential decay function, which is then used to compute the covariance matrix for the sub-sampled data set.

After sub-sampling, the ascending and descending data sets include 185 and 274 data points, respectively, while the GPS data set includes 17×3 data points. We apply a non-linear optimisation scheme to find the set of model parameters that minimizes the weighted residual sum of squares, WRSS = $\mathbf{r}^T \sum^{-1} \mathbf{r}$, where $\mathbf{r}$ is the difference between the observed and predicted displacements, and $\sum$ is the data covariance matrix. During optimisation we use a simulated annealing algorithm, followed by a derivative-based algorithm (e.g. Cervelli et al., 2001). The simulated annealing performs a random search through the predefined model parameter space and identifies the region near the absolute model-cost minimum. The algorithm is able to escape local minima due to the randomness of the search, but it does not necessarily find the minimum itself. The result of the simulated annealing is therefore passed to a derivative-based algorithm to improve the model further. The mean and confidence intervals of the model parameters are estimated using a bootstrap algorithm (Efron and Tibshirani, 1986), that performs the optimisations

on a large number of randomly resampled data sets and computes the confidence intervals from the range of the estimated parameters. We report the goodness of fit to the data using the reduced chi-squared, calculated as $\chi^2_\nu = \frac{WRSS}{N-m}$, where N is the number of data and m is the number of unknown model parameters.

6.2 Results of modelling

The simplest model with a single point source for each of the Reykjanes and Svartsengi subsidence bowls has a $\chi^2_\nu=4.2$. The fit is improved if we increase the number of point sources to two ($\chi^2_\nu=3.7$) or three ($\chi^2_\nu=1.8$) to explain the subsidence around the Reykjanes field. In the two- and three-point source models, the sources align along the NE–SW trend of the subsidence signal, at 1.5–2.8 km depth. If we instead use a single ellipsoidal source for the Reykjanes subsidence and a point source for the Svartsengi subsidence, then we obtain a $\chi^2_\nu=2.5$. The estimated ellipsoidal source is clearly elongated in the horizontal NE–SW direction with a semimajor to semiminor axis ratio of 4.5. As with the point source models, the fit is improved if we instead use two ($\chi^2_\nu=2.2$) or three ($\chi^2_\nu=1.5$) ellipsoidal sources. The estimated ellipsoid parameters are listed in Table 1, for the model with one (1a), two (2a, b) and three (3a, b, c) sources for the Reykjanes subsidence, and Figure 6 shows the data that were used as input in the optimisations and the results computed from the three-ellipsoid model. The bootstrap confidence limits seem small and may be underestimated due to the correlations in the InSAR data.

During the optimisations we allow all ellipsoids to vary freely in strike and plunge of the semimajor axis. The sources that have a sub-horizontal plunge show a clear NE–SW orientation. However, both the two- and three-ellipsoid models have a steeply plunging source. In the model with three ellipsoidal sources, the steep source (3b) plunges 68±3° toward NW, and is centred at 4.3±0.1 km depth. Note the similarity of sources 2a and 3a and the sources 2b and 3b in Table 1. The additional source 3c in the three-ellipsoid model is located near the SW part of the subsidence bowl and has a small volume decrease. The best-fit three-ellipsoid model shown in Figure 6 reproduces the GPS and radar observations to the first order. The residuals of the ascending data are generally larger than for the descending data. The GPS residuals are usually within the uncertainties of the observations, however, two data points in the Reykjanes subsidence bowl have larger residuals.

The Svartsengi point source is located at 5 km depth and has a volume decrease of around 2.6×10^{-3} km^3. The depth of the Svartsengi source seems a little too deep, compared to the depth of the production boreholes in Svartsengi of 1–2 km (Jónsson et al., 2009). The large depth may occur because the source tries to fit some regional subsidence along the plate boundary, and not just the local subsidence around the geothermal field. We also test the ellipsoidal source for Svartsengi, but the results are scattered, with a roughly equi-dimensional source without a preferred orientation.

7   Discussion

7.1   Subsidence and pressure changes

In the previous section we found that the observed surface subsidence around the Reykjanes geothermal field can be fitted well using three ellipsoidal sources in an elastic halfspace. Our model assumes a simplified reservoir using finite ellipsoidal pressure sources, and does not consider the poroelastic processes related to the flow of the interstitial fluid and the deformation of the porous rock. However, the pore pressure changes induced by fluid extraction diminishes outside the reservoir, thus the deformation of the crust surrounding the reservoir can be assumed elastic (Segall and Fitzgerald, 1998). Our elastic halfspace model, therefore, provides a reasonable simulation of the deformation of the crust surrounding the reservoir.

In the Reykjanes field, geothermal fluids are mostly extracted from 1–2.5 km depth (Jónsson et al., 2009). The two horizontal ellipsoids from the three-ellipsoid model are located within this depth range, but the steeply plunging ellipsoid is deeper, centred at around 4 km. As the ellipsoid plunges steeply it extends to the shallower depths, corresponding to the production depth in the well field. However the source depth still seems high and it may not be as well constrained as the bootstrap optimisations indicate. The steep ellipsoid has most of the volume change, that is 2/3 out of the total volume change of 3.6×10^{-3}km^3 from the three sources, suggesting that water primarily flows to the well field from below. During 2005–2008, a total of 57.9 Mton fluids were extracted from the Reykjanes field (Vatnaskil, 2009). Assuming a density of 820 kg/m^3 of the geothermal water (Eysteinsson, 2000), this corresponds to a volume withdrawal of 70.6×10^{-3}km^3, that is, 20 times the estimated volume change from the three ellipsoidal sources.

The difference between the volume of the extracted fluids and the volume decrease may seem large, but a similar difference was estimated in the Svartsengi field during 1975–1999 (Eysteinsson, 2000). The extracted fluids are partly replaced by the natural recharge into the system. However, the natural recharge does not completely make up for the extracted fluids, hence the pore pressure within the reservoir decreases and the ground water level drops. The decrease in pore pressure, in turn, results in a small contraction of the rock matrix. The large difference between the volume of the extracted fluids and the estimated volume change of the host rock indicates that the rock matrix is relatively strong and that the fluid extraction does not considerably reduce the permeability in the reservoir. Thus the well field productivity can be maintained in future by increased natural recharge as well as reinjection of waste fluids.

Figure 7 shows a comparison of the vertical GPS displacements at the station RNES, the maximum descending LOS displacements in the Reykjanes field and the pressure observed at 1500 m depth in three boreholes (Jónsson et al., 2009). The boreholes RN12 and RN23 are production holes located within in the main well field, while RN16 is located some hundred meters further NW and is only used for monitoring and research. The geodetic data and the pressure observations show the same pattern: slow subsidence and slowly decreasing pressure during 2003–2006, followed by an abrupt change to higher rates at the time of the start of production in the Reykjanes field in 2006. The pressure observations clearly show that the pressure decrease starts to tail out during 2007, indicating that it is stabilising at a slower rate. The stabilisation of the pressure decrease is expected as the recharge into the system usually increases during the first years of production, and the observed pressure changes are in good agreement with numerical simulations of the reservoir fluid and heat flow (Björnsson et al., 2008). The surface subsidence observed by GPS also appears to tail off, albeit at a slower rate than the pressure observations, indicating that the crustal response is somewhat delayed from the pressure changes. The pressure decrease in RN16 is smaller than that observed in the production boreholes located within the main well field, however it shows a very similar pattern. The total pressure decrease in the production boreholes is around 3 MPa.

7.2 Induced seismicity

Extraction of fluids from geothermal and hydrocarbon reservoirs are known to trigger seismicity in several cases, such as in the Geysers geothermal field (Eberhart-Phillips and Oppenheimer, 1984), the Coso geothermal field in USA (Fialko and Simons, 2000) and the Lacq gas field in southwestern France (Grasso and Wittlinger, 1990). Near the Lacq gas field, earthquakes with magnitudes up to 4.2 have been recorded, in an area that is clearly separated from the tectonic seismicity in the Pyrenees (Grasso and Wittlinger, 1990). The seismicity began when the pressure had decreased by 30 MPa, ten years after the start of gas extraction. The subsidence around the Lacq gas field varies linearly with the average reservoir pressure drop, indicating that the contraction of the reservoir can be explained by a linear poro-elastic model (Segall et al., 1994). The poro-elastic stressing due to reservoir contraction has been examined in detail by Segall (1989) and Segall and Fitzgerald (1998). They found through analytical modelling of a circular disk-shaped reservoir, that the least compressive horizontal stress within the reservoir decreases with decreasing pore pressures, thus enhancing tensional fracturing. Outside the reservoir production does not directly decrease the pore pressure so that the tendency for normal faulting is considerably larger. In extensional environments, normal faulting will be promoted near the edge of the reservoir, or anywhere there is a steep gradient in pore-pressure reduction (Segall and Fitzgerald, 1998).

A change in the pattern of seismicity is observed following the start of production in the Reykjanes power plant (Figure 8). Earthquakes on the Reykjanes Peninsula usually occur along a narrow ENE trending zone extending from the tip of the peninsula to the Hengill area (Tryggvason, 1973). An intense swarm of several thousand micro-earthquakes were recorded on the tip of the peninsula in 1972 by a local seismic network (Klein et al., 1977). Accurate epicentre locations of a subset of the swarm events showed that most of the earthquakes occurred within a less than 2 km wide and approximately 12 km long zone, as outlined in Figure 8. Since the early 1990s, earthquakes in Iceland have been recorded by the SIL seismic network operated by the Icelandic Meteorological Office (Bödvarsson et al., 1999; Jakobsdóttir, 2008). Earthquake locations and magnitudes as well as focal mechanism solutions are determined as part of the routine SIL analysis.

During the first months after the start of production in the Reykjanes field, the SIL network recorded three short-lived earthquake swarms SE of the tip of the peninsula, along the periphery of the subsidence bowl. The swarms occurred on 31 May–1 June, 9–10 July and 27–28 September 2006 (orange dots in Figure 8), and each of them had 40–80 recorded events with a maximum local magnitude of $M_L 3$. A swarm occurred in the same area on 6–11 January 2008, and another swarm NW of the tip on 8 July 2008 (blue dots). The focal mechanisms, as determined by the SIL analysis, showed that the largest events were typically consistent with normal faulting on NE-trending planes (see Figure 8), although there is some uncertainty on the mechanisms as the earthquakes are located outside the seismic network.

Very few earthquakes have previously been recorded in these areas by the SIL network, and the seismicity is clearly separated from the area of the intense 1972 swarm. We investigate if the unusual earthquake activity could be triggered by the crustal stresses caused by the contraction within the geothermal field. From our three-ellipsoid model for the subsidence around the Reykjanes geothermal field, we compute the change in Coulomb failure stress (ΔCFS) for normal slip on NE-SW trending fault planes dipping 60° toward NW, along a vertical profile AA' shown in Figure 8. The ΔCFS along this profile is mainly due to the steeply plunging ellipsoid (3b), because this source is located nearest the profile. The maximum stress change is around 0.3 MPa, which may be enough to trigger earthquakes (e.g. King et al., 1994). The earthquakes recorded during the swarms in 2006 and 2008 were generally located a little deeper than the area of maximum ΔCFS. However, the uncertainty of the hypocentre depths in this area reported by the SIL catalogue are typically 3–6 km, and recent work on the velocity model on the Reykjanes Peninsula indicates that the earthquake depths here may be a little too deep (K. Vogfjörd, personal communication, 2008).

Short-lived swarms also occurred SE of the Svartsengi field during 2–3 July 2007 (red dots) and 22–24 January 2008 (blue dots in Figure 8). The swarms only had 40–60 recorded events, but they both included a number of $M_L > 3$ events, and the January 2008 swarm included two $M_L 4$ events. Very little seismicity has been observed in the area since the start of production in the Svartsengi field in 1976, indicating that the pressure drawdown in the Svartsengi reservoir of around 3 MPa (Vatnaskil, 2009), may have raised the fracture limit and thus reduced the micro-earthquake activity temporarily (Brandsdóttir et al., 2002; Keiding et al.,

2009). The small swarms along the periphery of the Svartsengi subsidence bowl may occur in response to the increased reinjection of waste fluids during recent years.

7.3   Aseismic faulting

Interestingly, the radar data reveal subtle discontinuities that probably reflect fault movement, as can be seen in the near-vertical displacements along profile BB' in Figure 8. Near the NW end of the profile, we see a 3 km long NE-trending discontinuity, consistent with subsidence in a graben-like structure. This discontinuity becomes visible between two acquisitions from 14 September 2006 to 19 October 2006, a few months after the start of production in the Reykjanes field. No fractures have been mapped in this area, but the amplitude images from the radar data clearly show linear structures aligning with the edges of the discontinuity. The total offset in the near-vertical radar image is approximately 1 cm, but no earthquakes were associated with this event. A recent earthquake study on the Reykjanes Peninsula in fact suggested considerable aseismic faulting in the west (Keiding et al., 2009). A similar, albeit less clear, discontinuity can be seen near the SE end of the profile. The discontinuities are located at some distance from the Reykjanes subsidence bowl, however they are within the areas of increased tensile stress, and the appearance of the largest discontinuity in fall 2006 suggests that these faulting events are also induced by the subsidence due to geothermal fluid extraction.

8   Conclusions

We have examined the crustal deformation observed on the Reykjanes Peninsula during 1992–2009, using InSAR and GPS data. The plate boundary is transtensional with both left-lateral motion and opening, and a number of geothermal fields are located along the central plate boundary zone. The geodetic data show deformation due to the plate motion, anthropogenic subsidence around the Reykjanes, Svartsengi and Hellisheidi geothermal power plants and, possibly, pressure increase in the Krísuvík geothermal system. We investigate the subsidence around the Reykjanes field in more detail, and estimate a maximum subsidence of around 10 cm during the first two years of production. The subsidence bowl around the

Reykjanes field is clearly elongated in the NE–SW direction, thus aligning with the main trend of fractures in the area. The observed surface subsidence can be modelled using point or ellipsoidal pressure sources in an elastic halfspace. A model with two or three ellipsoidal sources for the subsidence around Reykjanes indicates that water flows to the well field primarily from below, but there is also considerable lateral flow due to the anisotropic permeability. Following the installation of the Reykjanes power plant, short-lived swarms of micro-earthquakes appear along the SE and NW periphery of the subsidence bowl, in areas where there has not previously been recorded earthquakes. The earthquake swarms, as well as aseismic fault movement revealed by the radar data, appear to be triggered by the stresses due to geothermal fluid extraction at Reykjanes.

9   Acknowledgements

References

Allis, R., C. Bromley and S. Currie, 2009. Update on subsidence at the Wairakei-Tauhara geothermal system, New Zealand. *Geothermics*, **38** (1), 169–180.

Altamimi, Z., X. Collilieux, J. Legrand, B. Garayt and C. Boucher, 2007. ITRF2005: A new release of the International Terrestrial Reference Frame based

on time series of station positions and Earth Orientation Parameters. *J. Geophys. Res.*, **112**, B09401. doi:10.1029/2007JB004949.

Amelung, F., D. L. Galloway, J. W. Bell, H. A. Zebker and R. J. Laczniak, 1999. Sensing the ups and downs of Las Vegas: InSAR reveals structural control of land subsidence and aquifer-system deformation. *Geology*, **27** (6), 483–486. doi:10.1130/0091-7613.

Árnadóttir, T., W. Jiang, K. L. Feigl, H. Geirsson and E. Sturkell, 2006. Kinematic models of plate boundary deformation in southwest Iceland derived from GPS observations. *J. Geophys. Res.*, **111**, B07402. doi:10.1029/2005JB003907.

Árnadóttir, T., B. Lund, W. Jiang, H. Geirsson, H. Björnsson, P. Einarsson and T. Sigurdsson, 2009. Glacial rebound and plate spreading: Results from the first countrywide GPS observations in Iceland. *Geophys. J. Int.*, **177**, 691–716. doi:10.1111/j.1365-246X.2008.04059.x.

Björnsson, H., G. Thorgilsson and S. Halldórsdóttir, 2008. Numerical modelling of the geothermal system in Reykjanes, predictions for 50 MW$_e$ production increase from year 2011 (in Icelandic). Report ÍSOR-08053, Iceland Geosurvey, Reykjavík, Iceland.

Bödvarsson, R., S. T. Rögnvaldsson, R. Slunga and E. Kjartansson, 1999. The SIL data acquisition system - at present and beyond year 2000. *Phys. Earth Planet. Inter.*, **113**, 89–101.

Brandsdóttir, B., H. Franzson, P. Einarsson, K. Árnason and H. Kristmannsdóttir, 2002. Seismic monitoring during an injection experiment in the Svartsengi geothermal field, Iceland. *Jökull*, **51**, 43–52.

Cervelli, P., M. H. Murray, P. Segall, Y. Aoki and T. Kato, 2001. Estimating source parameters from deformation data, with an application to the March 1997 earthquake swarm off the Izu Peninsula, Japan. *J. Geophys. Res.*, **106** (B6), 11,217–11,238.

Clifton, A. E. and S. A. Kattenhorn, 2006. Structural architecture of a highly oblique divergent plate boundary segment. *Tectonophysics*, **419**, 27–40.

Clifton, A. E., F. Sigmundsson, K. L. Feigl, G. Gudmundsson and T. Árnadóttir, 2002. Surface effects of faulting and deformation resulting from magma accumulation at the Hengill triple junction, SW Iceland, 1994–1998. *J. Volcanol. Geotherm. Res.*, **115**, 233–255.

Dach, R., U. Hugentobler, P. Fridez and M. Meindl, 2007. *Bernese GPS software version 5.0*. Switzerland.

DeMets, C., R. G. Gordon, D. F. Argus and S. Stein, 1994. Effect of recent revisions to the geomagnetic reversal time scale on estimates of current plate motions. *Geophys. Res. Lett.*, **21** (20), 2191–2194.

Donnelly, L. J., 2009. A review of international cases of fault reactivation during mining subsidence and fluid abstraction. *Quart. J. Eng. Geol. Hydrol.*, **42**, 73–94. doi:10.1144/1470-9236/07-017.

Dow, J. M., R. E. Neilan and G. Gendt, 2005. The International GPS Service (IGS): Celebrating the 10th anniversary and looking to the next decade. *Adv. Space Res.*, **36** (3), 320–326. doi:10.1016/j.asr.2005.05.125.

Eberhart-Phillips, D. and D. H. Oppenheimer, 1984. Induced seismicity in the Geysers geothermal area, California. *J. Geophys. Res.*, **89** (B2), 1191–1207.

Efron, B. and R. Tibshirani, 1986. Bootstrap methods for standard errors, confidence intervals, and other measures of statistical accuracy. *Statistical Science*, **1** (1), 54–75.

Eysteinsson, H., 2000. Elevation and gravity changes at geothermal fields on the Reykjanes Peninsula, SW Iceland. *Proceedings World Geothermal Congress 2000*, pages 559–564.

Feigl, K. L., J. Gasperi, F. Sigmundsson and A. Rigo, 2000. Crustal deformation near Hengill volcano, Iceland 1993–1998: Coupling between magmatic activity and faulting inferred from elastic modeling of satellite radar interferograms. *J. Geophys. Res.*, **105** (B11), 25,655–25,670.

Fialko, Y. and M. Simons, 2000. Deformation and seismicity in the Coso geothermal area, Inyo County, California: Observations and modeling using satellite radar interferometry. *J. Geophys. Res.*, **105** (B9), 21,781–21,793.

Glowacka, E., J. Gonzáles and H. Fabriol, 1999. Recent vertical deformation in Mexicali Valley and its relationship with tectonics, seismicity, and the exploitation of the Cerro Prieto geothermal field, Mexico. *Pure Appl. Geophys*, **156**, 591–614.

Grasso, J. R. and G. Wittlinger, 1990. Ten years of seismic monitoring over a gas field. *Bull. Seis. Soc. Am.*, **80** (2), 450–473.

Herring, T. A., R. W. King and S. C. McClusky, 2006. GLOBK Reference Manual, Global Kalman filter VLBI and GPS analysis program, Release 10.3. Technical report, Massachusetts Institute of Technology, USA.

Hoffmann, J., H. A. Zebker, D. L. Galloway and F. Amelung, 2001. Seasonal subsidence and rebound in Las Vegas Valley, Nevada, observed by synthetic aperture radar interferometry. *Water Resour. Res.*, **37** (6), 1551–1566.

Hooper, A., 2008. A multi-temporal InSAR method incorporating both persistent scatterer and small baseline approaches. *Geophys. Res. Lett.*, **35**, L16302. doi: 10.1029/2008GL034654.

Hooper, A., R. Pedersen and F. Sigmundsson, 2009. Constraints on magma intrusion at Eyjafjallajökull and Katla volcanoes in Iceland, from time series SAR interferometry. In C. J. B. et al. (ed.), *The VOLUME Project, VOLcanoes: Understanding subsurface mass moveMEnt*, pages 13–24.

Hooper, A., P. Segall and H. Zebker, 2007. Persistent scatterer interferometric synthetic aperture radar for crustal deformation analysis, with application to Volcán Alcedo, Galápagos. *J. Geophys. Res.*, **112**, B07407,. doi:10.1029/2006JB004763.

Hreinsdóttir, S., T. Árnadóttir, J. Decriem, H. Geirsson, A. Tryggvason, R. A. Bennett and P. LaFemina, 2009. A complex earthquake sequence captured by the continuous GPS network in SW Iceland. *Geophys. Res. Lett.*, **36**, L12309. doi:10.1029/2009GL038391.

Hreinsdóttir, S., P. Einarsson and F. Sigmundsson, 2001. Crustal deformation at the oblique spreading Reykjanes Peninsula, SW Iceland: GPS measurements from 1993 to 1998. *J. Geophys. Res.*, **106** (B7), 13,803–13,816.

Jakobsdóttir, S. S., 2008. Seismicity in Iceland: 1994–2007. *Jökull*, **58**, 75–100.

Jónsson, P., S. Halldórsdóttir and H. Björnsson, 2009. Svartsengi - Reykjanes, temperature and pressure measurements 2008 (in Icelandic). Report ÍSOR-2009/036, Iceland Geosurvey, Reykjavík, Iceland.

Jónsson, S., P. Segall, R. Pedersen and G. Björnsson, 2003. Post-earthquake ground movements correlated to pore-pressure transients. *Nature*, **424**, 179–183. doi:10.1038/nature01776.

Kampes, B., R. Hanssen and Z. Perski, 2003. Radar Interferometry with Public Domain Tools. In *Proceedings of FRINGE 2003*. ESA ESRIN, Frascati, Italy.

Keiding, M., T. Árnadóttir, E. Sturkell, H. Geirsson and B. Lund, 2008. Strain accumulation along an oblique plate boundary: the Reykjanes Peninsula, southwest Iceland. *Geophys. J. Int.*, **172**, 861–872. doi:10.1111/j.1365-246X.2007.03655.x.

Keiding, M., B. Lund and T. Árnadóttir, 2009. Earthquakes, stress and strain along an obliquely divergent plate boundary: the Reykjanes Peninsula, southwest Iceland. *J. Geophys. Res.*, **114**, B09306. doi:10.1029/2008JB006253.

King, G., R. S. Stein and J. Lin, 1994. Static stress changes and the triggering of earthquakes. *Bull. Seis. Soc. Am.*, **84** (3), 935–953.

Klein, F. W., P. Einarsson and M. Wyss, 1977. The Reykjanes Peninsula, Iceland, earthquake swarm of September 1972 and its tectonic significance. *J. Geophys. Res.*, **82** (5), 865–888.

Lu, Z., T. Masterlark, J. Power, D. Dzurisin and C. Wicks, 2002. Subsidence at Kiska Volcano, Western Aleutians, detected by satellite radar interferometry. *Geophys. Res. Lett.*, **29** (18), 1855. doi:10.1029/2002GL014948.

Magnússon, I. T. and G. Thorbergsson, 2004. GPS measurements on the outer Reykjanes Peninsula 2004 (in Icelandic). Report IV Hluti, Iceland GeoSurvey, Reykjavík.

Mogi, K., 1958. Relations between the eruptions of various volcanoes and the deformations of the ground surfaces around them. *Bull. Earthquake Res. Inst. Univ. Tokyo*, **36**, 99–134.

Mossop, A. and P. Segall, 1997. Subsidence at The Geysers geothermal field, N. California from a comparison of GPS and leveling surveys. *Geophys. Res. Lett.*, **24** (14), 1839–1842.

Pagli, C., F. Sigmundsson, T. Árnadóttir, P. Einarsson and E. Sturkell, 2004. Deflation of the Askja volcanic system: Constraints on the deformation source from combined inversion of satellite radar interferograms and GPS measurements. *J. Volcanol. Geotherm. Res.*, **152**, 97–108. doi:10.1016/j.jvolgeores.2005.09.014.

Peltier, A., T. Hurst, B. Scott and V. Cayol, 2009. Structures involved in the vertical deformation at Lake Taupo (New Zealand) between 1979 and 2007: New insights from numerical modelling. *J. Volc. Geotherm. Res.*, **181**, 173–184. doi:10.1016/j.jvolgeores.2009.01.017.

Sæmundsson, K., 1978. Fissure swarms and central volcanoes of the neovolcanic zones of Iceland. *Geol. J. Special Issue*, **10**, 415–432.

Segall, P., 1989. Earthquakes triggered by fluid extraction. *Geology*, **17**, 942–946.

Segall, P. and S. D. Fitzgerald, 1998. A note on induced stress changes in hydrocarbon and geothermal reservoirs. *Tectonophysics*, **289**, 117–128.

Segall, P., J. R. Grasso and A. Mossop, 1994. Poroelastic stressing and induced seismicity near the Lacq gas field, southwestern France. *J. Geophys. Res.*, **99** (B8), 15,423–15,438.

Sigmundsson, F., P. Einarsson, S. Rognvaldsson, G. Foulger, K. Hodgkinson and G. Thorbergsson, 1997. The 1994–1995 seismicity and deformation at the Hengill triple junction, Iceland: Triggering of earthquakes by minor magma injection in a zone of horizontal shear stress. *J. Geophys. Res.*, **102** (B7), 15,151–15,161.

Sudhaus, H. and S. Jónsson, 2008. Improved source modelling through combined use of InSAR and GPS under consideration of correlated data errors: Application to the June 2000 Kleifarvatn earthquake, Iceland. *Geophys. J. Int.*, **176**, 389–404. doi:10.1111/j.1365-246X.2008.03989.x.

Tiampo, K. F., J. B. Rundle, J. Fernandez and J. O. Langbeinc, 2000. Spherical and ellipsoidal volcanic sources at Long Valley caldera, California, using a genetic algorithm inversion technique. *J. Volcanol. Geotherm. Res.*, **102**, 189–206.

Tryggvason, E., 1973. Seismicity, earthquake swarms, and plate boundaries in the Iceland region. *Bull. Seis. Soc. Am.*, **63** (4), 1327–1348.

Vadon, H. and F. Sigmundsson, 1997. Crustal deformation from 1992 to 1995 at the mid-Atlantic ridge, southwest Iceland, mapped by satellite radar interferometry. *Science*, **275**, 194–197.

Vasco, D. W., C. Wicks, K. Karasaki and O. Marques, 2002. Geodetic imaging: Reservoir monitoring using satellite interferometry. *Geophys. J. Int.*, **149** (3), 555–571. doi:10.1046/j.1365-246X.2002.01569.x.

Vatnaskil, 2009. Svartsengi - Reykjanes, production overview for 2008 (In Icelandic). Report 09.04, Hitaveita Sudurnesja, Reykjavík, Iceland.

Werner, C., U. Wegmüller, T. Strozzi and A. Wiesmann, 2000. GAMMA SAR and interferometric processing software. In *Proc. ERS-ENVISAT Symp. Gothenburg, Sweden.* European Space Agency.

Wessel, P. and W. H. F. Smith, 1998. New, improved version of the Generic Mapping Tools released. *Eos Trans. AGU*, **79**, 579.

Wicks, C., W. Thatcher and D. Dzurisin, 1998. Migration of fluids beneath Yellowstone Caldera inferred from satellite radar interferometry. *Science*, **282** (5388), 458–462.

Yang, X.-M., P. M. Davis and J. H. Dieterich, 1988. Deformation from inflation of a dipping finite prolate spheroid in an elastic half-space as a model for volcanic stressing. *J. Geophys. Res.*, **93** (B5), 4249–4257.

Zebker, H. A. and J. Villasenor, 1992. Decorrelation in interferometric radar echoes. *IEEE Transactions on Geoscience and Remote Sensing*, **30** (5), 950–959.
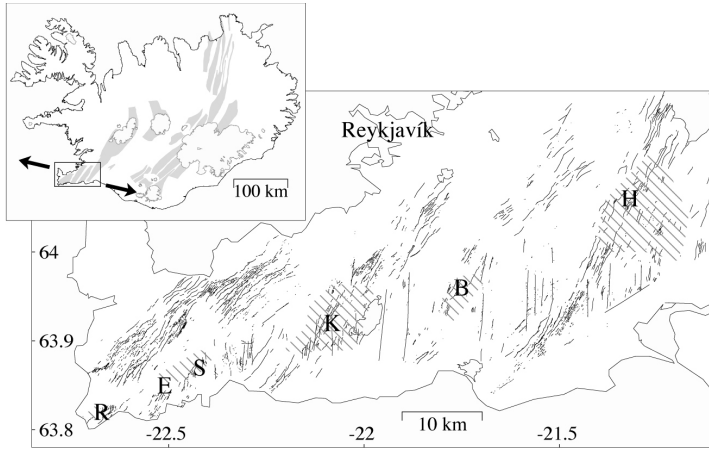
Figure 1: Tectonic map of the Reykjanes Peninsula, with fracture locations from Clifton and Kattenhorn (2006). The fractures are mainly NE–SW trending normal faults and tension fractures located within four volcanic fissure swarms. The hatched areas show the locations of high-temperature geothermal fields, labelled as R: Reykjanes, E: Eldvörp, S: Svartsengi, K: Krísuvík, B: Brennisteinsfjöll and H: Hengill. The Iceland inset shows the neovolcanic systems (grey shades) and the location of the study area. The arrows show the direction of the 2 cm/yr spreading across the peninsula between North America and Eurasia (DeMets et al., 1994).

RNES   HH04
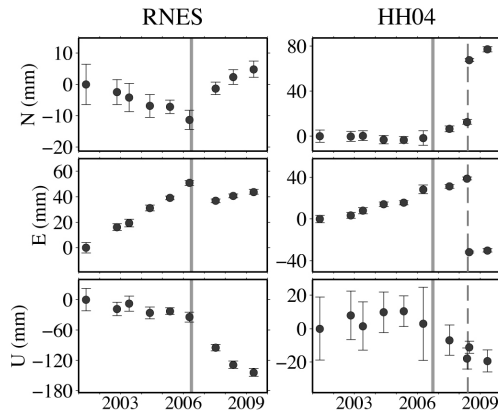
Figure 2: North, east and vertical time series at the campaign stations RNES and HH04 (see station locations in Figure 3), in the ITRF2005 reference frame. Error bars indicate 1σ uncertainties. The solid vertical lines show the approximate start of production at the Reykjanes and Hellisheidi geothermal power plants. The stippled line shows the time of the earthquake sequence on 29 May 2008.

Table 1: Estimated ellipsoidal source parameters for the subsidence around the Reykjanes field

	Lon	Lat	Depth	Strike	Plunge	Semimajor	Semiminor	Volume decrease
	(°W)	(°N)	(km)	(°)	(°)	(km)	(km)	($\times10^{-3}$ km^3)
1a	22.67	63.827	2.3±0.2	52±1	0±2	4±1	0.9±0.1	2.4±0.3
2a	22.64	63.843	2.0±0.1	51±1	6±2	6±1	0.3±0.1	1.1±0.1
2b	22.68	63.817	4.0±0.1	241±2	60±2	4±1	1.1±0.1	2.8±0.4
3a	22.64	63.838	1.6±0.1	28±3	1±1	6±1	0.2±0.1	0.8±0.1
3b	22.68	63.829	4.3±0.1	289±4	68±3	4±1	0.5±0.1	2.4±0.1
3c	22.71	63.819	1.1±0.1	232±2	2±2	3±1	1.2±0.1	0.4±0.1

The confidence limits are 68% percentiles from the bootstrap model parameters. A Poisson's ratio of 0.25 and a shear modulus of 10 GPa are used in all calculations (Fialko and Simons, 2000).
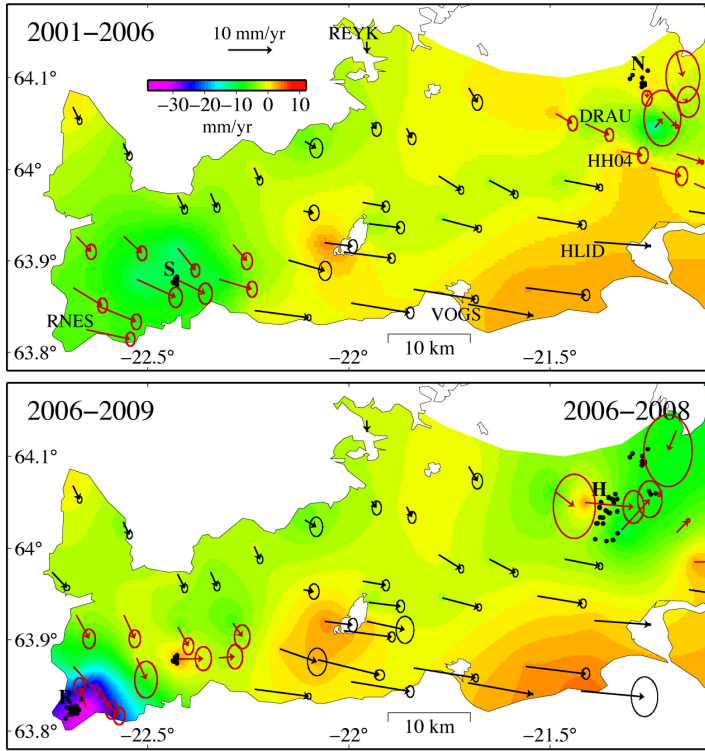
Figure 3: GPS velocities based on annual measurements during 2001–2009. The arrows show horizontal velocities with 1σ confidence ellipses, while the contour colours in the background show interpolated vertical velocities. Black dots show location of production boreholes at the Svartsengi (S), Nesjavellir (N), Hellisheidi (H) and Reykjanes (R) geothermal power plants. The velocities at stations near the Reykjanes and Hellisheidi power plants have been computed for 2001–2006 (upper panel) and 2006–2009 (lower panel, western peninsula) or 2006–2008 (lower panel, eastern peninsula). Note that only the velocity vectors coloured in red are from time series that have been split up into two periods, the other velocities are based on all available data. Some variations in the velocity vectors between the two time periods are due to changes in the network configuration, that is, abandonment of old stations or installation of new ones.
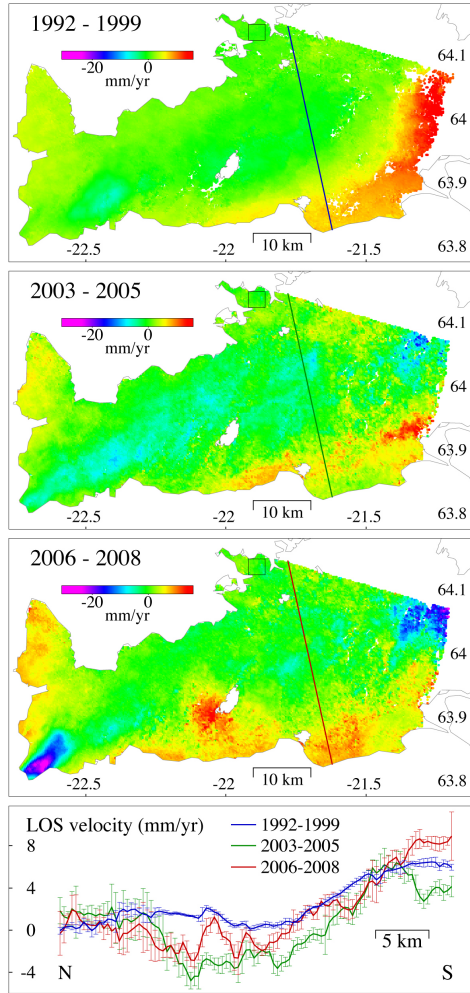
Figure 4: Residual mean LOS velocity fields after removal of bilinear ramps, relative to the mean value during each period in the area near Reykjavík (shown with the box). The time spans of the images are 11 May 1992–16 Sep 1999 (18 ERS images), 25 Sep 2003–29 Sep 2005 (9 Envisat images) and 6 Jul 2006–1 May 2008 (9 Envisat images). The profiles in the bottom panel show moving averages of the mean LOS rates and 1σ standard deviations along the line shown on the maps.
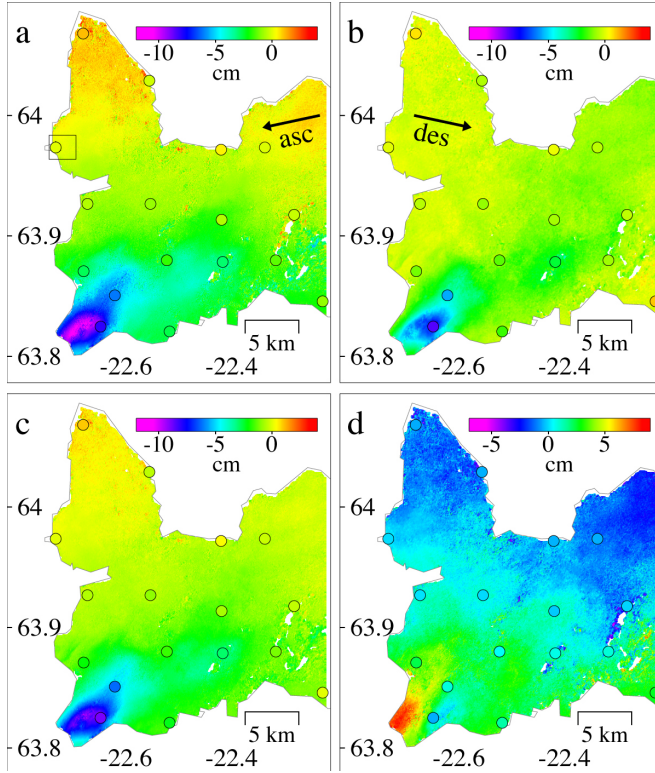
Figure 5: Linear combinations of ascending and descending radar data and comparison with GPS data. a) Ascending LOS displacement during 18 June 2005–3 May 2008 from two Envisat track 173 acquisitions. b) Descending LOS displacement during 16 June 2005–1 May 2008, estimated from 13 Envisat track 138 acquisitions. c) Near-vertical radar displacements from addition of ascending and descending LOS displacements. d) Approximately east-west radar displacement obtained by subtracting the ascending from the descending LOS displacements. The coloured circles show the magnitudes of the GPS displacements projected onto the direction of the radar displacements. The radar data in all four panels are shown relative to the mean value within the area shown with the box in panel a, and the GPS data are shown relative to the continuous GPS station located within the box. The arrows in panel a and b show the line-of-sight direction from ground toward the ascending and descending satellite.
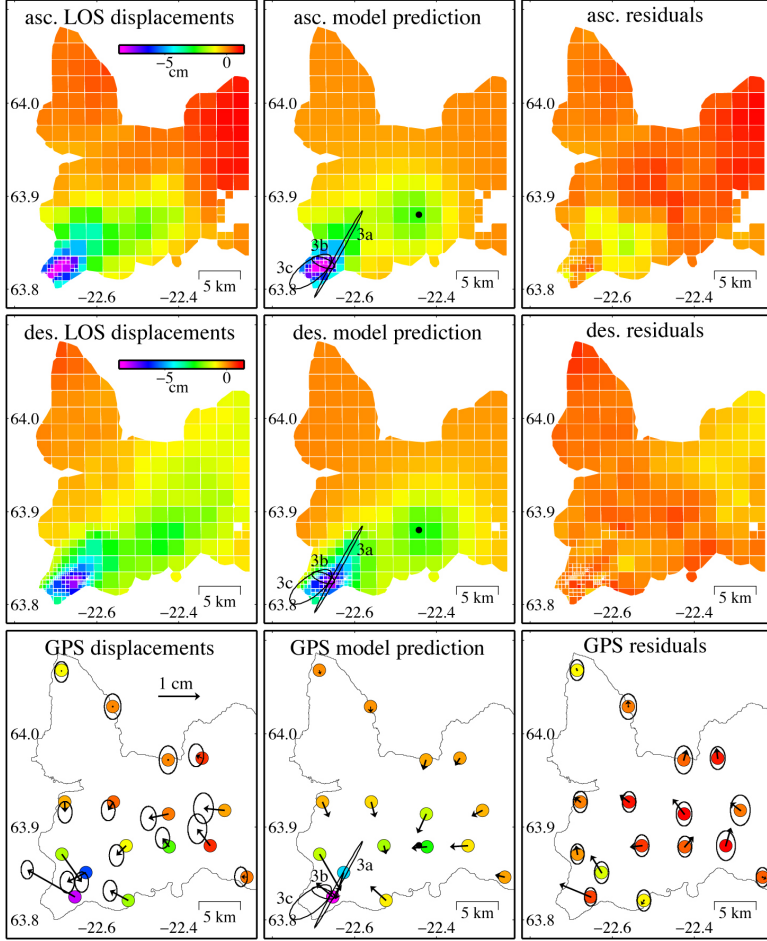
Figure 6: Ascending and descending radar LOS displacements and east, north and vertical GPS displacements included in optimisation for the Reykjanes and Svartsengi source parameters. The predicted surface displacements from the model with three finite ellipsoidal sources for Reykjanes and a point source for Svartsengi is shown, as well as the residuals between the observations and predictions. The coloured circles in the GPS figures show the vertical displacements. The colour scale for the ascending LOS, descending LOS and vertical GPS displacements is identical for the three figures.
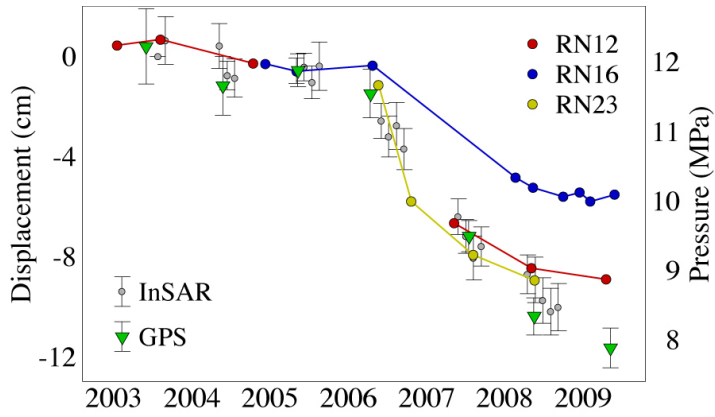
32

Figure 7: Time series spanning 2003–2008 with vertical GPS and descending radar LOS displacements, as well as pressure observed at 1500 m depth in three boreholes in the Reykjanes field. The GPS and radar displacements are in the same reference frame as in Figure 5.
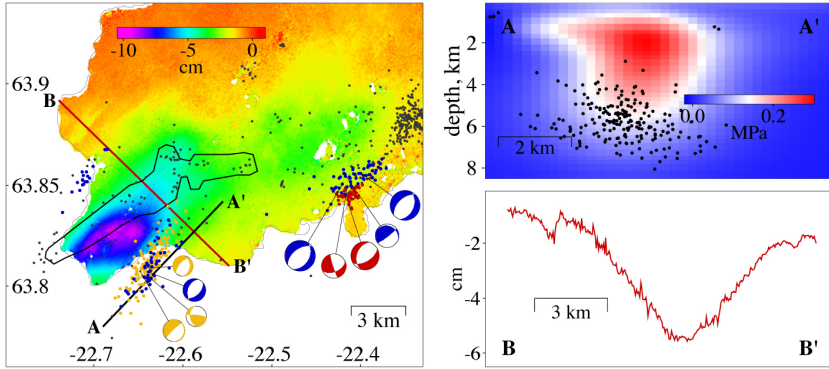
Figure 8: Close-up on the near-vertical radar displacement field during June 2005 – May 2008 (same as in Figure 5c). Earthquake locations and focal mechanisms from the SIL seismic catalogue are shown as background events (small black dots), and distinct swarm events in 2006 (orange), 2007 (red) and 2008 (blue). Also shown are focal mechanisms for some of the largest swarm events with local magnitudes ranging 2.9–4.1. The black outline shows the approximate location of the 1972 swarm activity (redrawn from Klein et al., 1977, their Figure 5). Profile AA' shows the predicted change in Coulomb failure stress, for normal slip on NE-SW trending fault planes, computed from the three-ellipsoid elastic halfspace model for the subsidence around the Reykjanes geothermal field. Profile BB' shows the observed near-vertical radar displacement across the Reykjanes subsidence bowl.